Feature extraction and quantification to explore human vasculature

Li Chen

A dissertation

submitted in partial fulfillment of the

requirements for the degree of

Doctor of Philosophy

University of Washington

2021

Reading Committee:

Jenq-Neng Hwang, Chair

Chun Yuan, Chair

Ming-Ting Sun

Program Authorized to Offer Degree:

Electrical and Computer Engineering

University of Washington

Abstract

Feature extraction and quantification to explore human vasculature

Li Chen

Chairs of the Supervisory Committee:
Professor Jenq-Neng Hwang
Department of Electrical and Computer Engineering
and
Professor Chun Yuan
Department of Radiology and Bioengineering

Human vasculature plays an important role in maintaining human body function. And vascular diseases are the top leading cause of death around the world. While advanced vascular imaging techniques are available to visualize human vasculature and disease regions, clinically relevant information in medical images (artery structural information, atherosclerotic plaque burden, etc.) remains to be extracted, quantified, validated and explored. Challenges exist preventing the feature extraction and quantification on human vasculature, partly due to the difficulties from the small artery region in the images, complex geometry of arteries, variable signals around vessel boundaries, and limited datasets available for vascular images.

In this dissertation, a toolbox of novel algorithms (*the Cafe family*) was proposed to facilitate 3D vascular image analysis so that comprehensive features of human vasculature can be extracted and quantified automatedly. The endpoint of the analysis is a *quantitative vasculature map*, which includes **three categories of useful imaging features**: artery structural features such as artery length, plaque morphometry features such as vessel wall thickness, and vascular disease features such as potential artery segments with atherosclerotic lesions. **Three key technical innovations were proposed**: 1) Three artery centerline tracing and labeling methods (tracklet refinement, *iCafe*, *AICafe*) based on different vascular beds and applications for extracting **artery structural features**; 2) *Y-net* and polar segmentation algorithms for extracting **plaque morphometry features**, including both inner vessel wall (lumen) and outer wall; 3) a domain adaptive classification model for extracting **atherosclerotic lesion features**.

Generating centerlines of arteries (list of 3D points with radii) is the starting point for the *quantitative vasculature map* construction, as centerlines not only provide artery structural features, but also identify region of interest for further vascular analysis. Three different approaches were proposed for artery tracing based on different vascular beds and purposes of applications. 1) For arteries with relatively straight structures, such as carotid or popliteal arteries, a slice-based artery detection method combined with the tracklet refinement algorithm was proposed to generate centerlines along the luminal centers of arteries. 2) For more challenging arteries with tortuous paths, such as intracranial arteries, a semi-automated image processing technique with graphical user interface (*iCafe*) was proposed to generate artery centerlines and label anatomical names for arteries with human corrections. 3) When fully automated process is needed, artificial intelligence (AI) techniques were applied to the *iCafe* workflow, so that the *AICafe* (AI+iCafe) method trained with processed *iCafe* results can automate artery tracing and

labeling. With artery centerlines and anatomical labels generated using either of the three approaches, a series of artery structural features can be extracted, such as artery length, volume and tortuosity for global or user defined artery groups. These features, as quantitative representations of artery structure and cerebral blood flow, have demonstrated to be useful in various vascular research.

After artery centerline generation, artery patches (region of images with artery in the center) can be extracted along the artery centerline for lumen/vessel wall segmentation to further assess luminal structures and atherosclerotic plaques. Traditional manual or semi-automated segmentation methods are time-consuming and only applicable to large straight arteries, limiting its usage in clinical setting or medical research. We propose fully automated lumen/vessel wall segmentation methods (*Y-net* and Polar models) for delineating lumen and outer wall boundaries based on different Magnetic Resonance (MR) sequences. For bright blood MRI (such as MR angiography) where only lumen areas are visualizable (bright in signal), *Y-net* (a patch-based lumen segmentation algorithm using convolutional neural network) is used to segment lumen regions from 3D images. For black blood MRI (such as MR vessel wall imaging (VWI)) where both lumen (black in signal) and vessel wall (bright in signal) are visualizable, lumen/vessel wall segmentation is more challenging due to the variable vessel wall signals and flow artifacts. We propose a polar-based method to segment vessel walls in the polar coordinate system so that the lumen/vessel wall boundaries are smoother and more continuous than traditional Cartesian-based methods. In addition, segmentation confidence was available from our model to suggest optional manual checking on challenging slices. The automated lumen/vessel wall segmentation was useful in various vascular research. For example, our *FRAPPE* tool (a member of *Cafe* family, designed for popliteal vessel wall analysis) reduced the analysis time for popliteal arteries in a knee MR

scan from 3 hours (manual) to 7 minutes (automated), which made large population analysis on lumen/vessel wall feasible.

In addition to vascular structure features and plaque morphometry features, <u>identification and classification of possible segments of arteries having vascular disease</u> (for example, atherosclerotic lesions) can provide additional vascular disease assessment features for the *quantitative vasculature map*. *LATTE* (another member of *Cafe* family) was designed for automated lesion identification and classification. In combination with a 2-minute MR VWI imaging sequence (MERGE) and an image quality assessment module, *LATTE* classifies artery slices along the centerlines into normal arteries, early lesions and advanced lesions, so that patients with vascular diseases can be identified and their artery segments with vascular diseases can be highlighted. One major challenge for robust lesion classification is the domain shift between different MR datasets (signal variations due to different scanners, imaging parameters, coils, etc.), due to which machine learning models developed from a single dataset may not perform robustly when deployed to new datasets. In order to reduce the domain shift, an unsupervised domain adaptation algorithm was applied on lesion classification. Without additional annotations, the CNN adapts its parameters based on the domain irrelevant signals from both the source and target datasets so that the final classification performance can be improved. *LATTE* was fast in analysis and robust towards various datasets. In addition to extract lesion related features, LATTE can also be a good candidate to be used clinically as a screening tool for vascular diseases.

With *the Cafe family* toolbox loaded with novel algorithms of medical image analysis and machine learning, artery centerlines were identified, lumen/vessel wall regions were segmented, and regions for vascular disease were located and categorized automatedly. The multi-dimensional features extracted and quantified from vascular images formed a *quantitative vasculature map*

which provides comprehensive information for vascular health and helps us better explore the disease pattern of human vasculature.

TABLE OF CONTENTS

iii

LIST OF FIGURES

LIST OF TABLES

ACKNOWLEDGEMENTS

Chapter 1. INTRODUCTION

1.1   HUMAN VASCULATURE

Human vasculature system circulates blood throughout the human body to maintain functioning of all organs. Any abnormal conditions of blood vessels (arteries and veins) can cause severe disability and death. Vascular disease is the leading cause of death globally, accounting for 17.3 million deaths per year, a number that is expected to grow to more than 23.6 million by 2030 [1].

Ischemic stroke due to atherosclerosis is one of the common cardiovascular diseases where plaque builds up in the arteries to form a stenosis or occlusion [2]. Artery is usually a tubular structure with inner wall (lumen, where blood flows inside) and outer wall. The advanced atherosclerotic plaque is of high risk for vascular health, as it can either reduce blood flow to distal artery regions, or a plaque may burst with embolus travels with the blood flow to cause a blockage further distal in the vascular system. **Monitoring atherosclerosis status thus includes two main perspectives**: identify artery structures to assess blood flow and identify vessel wall regions to assess plaque development and lesion burden. In addition, atherosclerosis is known as a systemic disease occurring in all vascular beds of human vasculature, for example, causing clinical events to the heart (coronary heart disease), brain (ischemic stroke), or lower extremities (peripheral vascular disease) [3]. The vasculature analysis is thus necessary for **all vascular beds**.

Vascular images, frequently from Magnetic Resonance Imaging (MRI) allows visualization of arteries in human vasculature. With different imaging parameters configurable in MRI, signals from blood regions can be either enhanced or suppressed, leading to different MRI sequences for imaging vasculatures. For example, Time of flight (TOF) Magnetic Resonance Angiography (MRA) has been commonly used to depict luminal stenosis resulting from atherosclerosis progression by enhancing signals in vascular regions. Due to the bright signals in the lumen areas

of arteries, MRA is also called a **bright blood MRI** sequence. The limitation for MRA is it can only identify lumen areas without clear signals on vessel wall areas. So more recently, through Magnetic Resonance (MR) Vessel Wall Imaging (VWI), vessel wall structures and pathologies can be characterized without radiation or contrast agents, providing additional diagnostic values [4], [5]. Due to the suppressed signals in the lumen areas, the MR VWI is a **black blood MRI** sequence. Figure 1.1 shows several examples of bright blood and black blood vascular images from MRI.
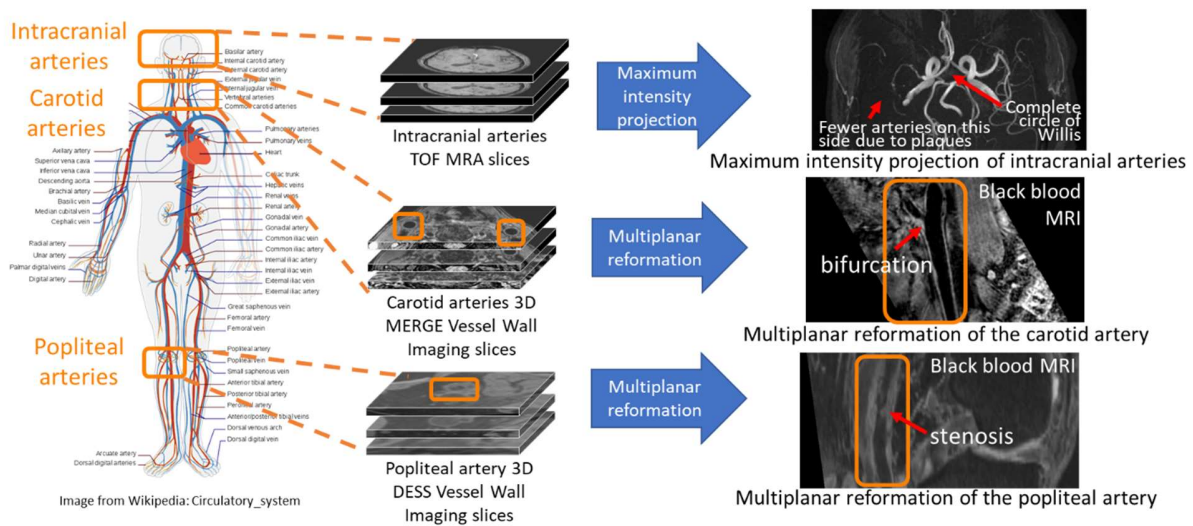
Figure 1.1 Example of vascular images.

Top: Maximum intensity projection (largest intensities along axial direction of a 3D image mapped into a 2D image) of intracranial arteries using MRA. Middle: Multiplanar reformation view of a carotid artery (with bifurcation) using the 3D Motion-Sensitized Driven Equilibrium prepared Rapid Gradient Echo (MERGE) sequence. Bottom: Multiplanar reformation view of a popliteal artery (with stenosis) using the 3D Dual Echo Steady State (DESS) MR imaging technique. Arteries are highlighted in the orange boxes. Normal vascular variations or disease related changes are frequent on vasculatures adding difficulties for quantitative analysis, such as complete/incomplete circle of Willis, plaque caused reduction of blood flow (top), carotid bifurcation (middle), and artery stenosis (bottom).

Extracting and quantifying the vasculature, especially identifying vascular features related with vascular disease from 3D vascular images is important in vascular analysis. For example, from MRA, human vasculature can be digitally constructed into a network of inter-connected tubes to identify the artery structures and assess the vessel density as a representative of blood flow. Vessel wall segmentation in MR VWI provides quantitative measurements of atherosclerotic burden, which can be exploited for monitoring disease progression in serial studies and clinical trials [6], [7].

1.2 TECHNICAL CHALLENGES

It is challenging to extract and quantify features from vascular images, mainly due to three reasons, 1) small and complicated geometry for arteries, 2) low image quality or signal contrast between vessel and surrounding tissues in vascular images, and 3) limited datasets available for vascular images. Some challenging examples from both bright blood MRA and black blood VWI are shown in Figure 1.2.

Small and complicated geometry for arteries. Due to the 3D nature of vasculature, vascular images are usually acquired in 3D space. The arteries are tiny structures (usually take less than 0.1% of the image space) compared with other human organs. Usually, small but anatomically important arteries, such as posterior communicating arteries, are hard to be identified and quantified accurately. To analyze arteries, a region of interest identification is usually required. However, correct target artery identification is not easy, as usually more arteries than the artery of interest co-exist in the view. For example, in the carotid region, the internal carotid artery (ICA) is of our interest instead of the external carotid artery (ECA), so the algorithm needs to identify the ICA although ICA and ECA are quite similar in appearance. In addition, not all the human vasculature has straight tubular structures easy to be identified. Intracranial arteries (Figure 1.1

top), for example, are a complex network of tortuous arteries with substantial inter-individual variations [8]. In addition, human vasculature is often with physiological or pathophysiological changes and inter-subject variations, arteries may bifurcate into smaller branches (Figure 1.1 middle, fourth image in Figure 1.2) or suffer from stenosis (Figure 1.1 bottom).

Low image quality or signal contrast between vessel and surrounding tissues in vascular images. Current imaging techniques are not perfect for visualizing vasculatures, introducing imaging artifacts or leading to poor image qualities. For example, MRA has relatively weak signal from small branches (first image in Figure 1.2), resulted from slow or in-plane blood flow. MR VWI is easily affected by artifacts (last image in Figure 1.2) including poor flow suppression and motion artifacts. MR hardware can also cause problems, such as coil inhomogeneity (third image in Figure 1.2) will lead to uneven signal intensity within the image slice. For vessel wall imaging, blood flow can be suppressed to display lumen areas with high contrast, but the outer wall is hard to visualize using the current imaging technique. Signals around outer wall boundaries may have similar image intensity with surrounding tissues (second image in Figure 1.2).
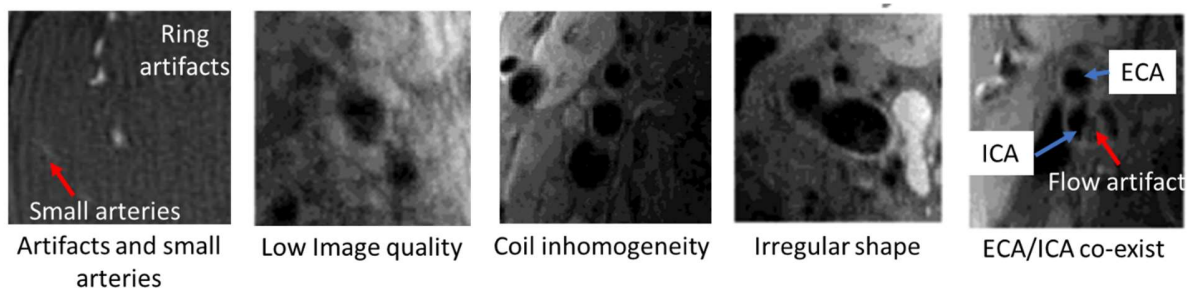
Figure 1.2 Examples of vessel wall slices challenging for segmentation.
Frist slice is from MRA, the rest are from MR VWI. ECA: external carotid artery, which is not of interest. ICA: internal carotid artery, which is of interest.

Limited datasets available for vascular images. The data and label availability for vascular images is another challenge. Unlike natural images where abundant data with labels of good

quality are publicly available, the lack of vascular images due to the expensive MRI scan is a major restriction to develop machine learning models in vascular image analysis. In addition, only trained vascular reviewers with sufficient medical background are capable of reviewing the vascular images and labeling the vascular markers (vessel wall contours, lesion types, etc.), which adds more difficulties for vascular image analysis. Developing techniques with limited training samples and labels is always desired in vascular image analysis.

1.3   AIMS

We proposed to use medical image analysis and machine learning techniques on vascular images to construct a *quantitative vasculature map*, which includes artery centerline generation (tracing and anatomical labeling), vessel wall segmentation, and atherosclerotic lesion identification, so that comprehensive vascular features can be extracted and quantified from the vasculature map for vascular analysis.

Related work will be discussed in Chapter 2. Then three major components for constructing the *quantitative vasculature map* will be introduced in Chapter 3-5. Chapter 3 will focus on artery centerline generation, including three approaches for artery tracing and anatomical labeling (tracklet refinement, *iCafe*, *AICafe*), followed by artery refinements and related clinical applications. Chapter 4 will cover the topic of lumen/vessel wall segmentation, including the *Y-net* and polar-based segmentation approaches. *FRAPPE*, as a clinical application for vessel wall segmentation will also be introduced in this chapter. In Chapter 5, the extraction of atherosclerotic lesion features using an identification and classification method (*LATTE*) will be discussed with a focus on the domain adaptation for improving cross-domain performance. Finally, we will draw conclusions in Chapter 6.

Chapter 2. RELATED WORK (BACKGROUND AND CHALLENGE)

Vascular analysis algorithms or tools reported in literation are usually focused on a specific task with limited capabilities. There is no existing method to extract and quantify vascular features on both large and small arteries, on both lumen and outer wall, applicable to multiple vascular beds, and can highlight segments of arteries having atherosclerotic lesions. Without such comprehensive features, the representation of the overall health status of human vasculature is not complete, and the diagnostic value for vascular disease is greatly limited.

The most related vascular image analysis methods with our *quantitative vasculature map* can be mainly summarized into several topics: artery tracing (section 2.1), artery anatomical labeling (section 2.2), and vessel wall segmentation (section 2.3). After different image analysis methods, we will discuss the vascular feature extraction approaches (section 2.4) and summarize this chapter (section 2.5).

2.1   ARTERY TRACING

Artery tracing converts artery voxels from 3D images into interconnected tree structures with 3D artery centerlines (list of 3D points with various radius at each point). Due to the complexity of artery structures in 3D space, especially intracranial arteries, there are few manual tracing methods [9]. Most semi-automated or automated methods can be summarized into segmentation-based or tracking-based approaches.

Segmentation-based approaches. Voxels belonging to the vascular region are first segmented, then a vessel skeletonization method identifies artery centerlines through iterative thinning. Finally, radii along the centerlines are estimated by fitting the segmented voxels. Methods belonging to this approach mainly differ in the segmentation algorithm, which was

comprehensively discussed in review papers [10]–[12]. Recently, convolutional neural network (CNN) based vascular segmentation has become the predominant method, such as using the inception module equipped U-Net (Uception) [13], the Dense-net equipped U-Net (DDNet) [14], the multi-path 2.5D based VesselNet [15], the DeepVesselNet [16] with cross-hair filter to apply 2D and 3D information, the JointVesselNet [17] with dual-stream segmentation using 3D volume and 2D maximum intensity projection, and the radial distance transformed segmentation [18]. However, usually for these methods, there is no guarantee for the smoothness and continuity of vessels after skeletonization. Moreover, two nearby vessels close to each other might be traced as one large vessel.

Tracking-based approaches. Initial seeds are identified as the starting points from the vascular image, then the artery centerline and radius are directly identified from seed points through iteratively stretching both ends of the trace during tracking. It is critical to predict the correct direction for stretching, which can either be decided by human designed rules, for example, the first principal direction of the Jacobian matrix of images [19], Hessian-based estimation [20], Kalman filtering [21] or from a neural network used in CNN Tracker and DCAT [22], [23]. Traces generated by tracking methods might be rough or zigzagged. To solve this issue, some smoothness constraints such as the active contour model can be combined in the tracking approach to ensure smoothness and fitness of centerlines [24]. In addition, tracking-based approaches are sensitive to initial seed placement. When the image quality suffers, improper seed selection is likely to cause tracing leakages into the background or lead to incomplete vasculature tracing.

To ensure robust artery tracing, post-tracing artery refinement by centerline positions re-centering is sometimes performed. Adjusting centerline positions using intensity information [40] or segmentation results [43] from re-sliced 2D cross-sectional planes is usually used, but such

methods do not consider the longitudinal information along the artery centerlines, which might be valuable in artery refinements.

In summary, 1) previous manual or semi-automated artery tracing methods cannot reliably identify all the vasculatures in vascular images, limiting the available features that can be extracted; 2) segmentation-based and tracking-based approaches have their own strength and weakness; 3) global vascular prior knowledge, for example, intracranial arteries are likely to have tree (non-loop) structures, has not been well utilized in model design for artery tracing.

2.2   ARTERY ANATOMICAL LABELING

Artery anatomical labeling is the step of assigning artery names to each segment of trace. This task is especially challenging for intracranial arteries where hundreds of arteries are inter-connected in a vascular tree. Thus methods for artery labeling are mainly focused on intracranial artery labeling, or more specifically the Circle of Willis (CoW) arteries located in the center of intracranial arteries. An example of labeled intracranial arteries and the simplified graph illustration of intracranial arteries is shown in Figure 2.1.
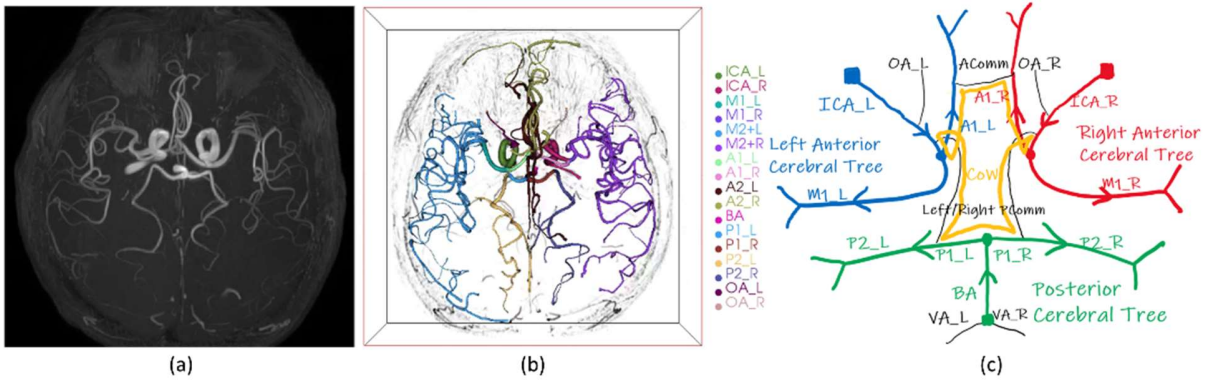
Figure 2.1 Intracranial artery images and structures.

(a) Time of flight (TOF) MRA of cerebral arteries. (b) Intracranial arteries labeled in different colors. (c) Illustration of CoW (yellow), left (blue) and right (red) anterior circulation, posterior circulation (red) and optional artery branches (black) with their anatomical names.

When there are intracranial arteries variations, not only the optional artery branches, but also A1, M1, P1 segments may be missing.

There have been continuous efforts in automating intracranial arteries labeling, using either private datasets with a limited number of scans or the publicly available UNC dataset with 50 cerebral Magnetic Resonance Angiography (MRA) images [25]. Takemura et al. [26] built a template of the CoW on five subjects, then arteries were labeled by template alignment and matching on fifteen scans. A more complete artery atlas was built from a population-based cohort of 167 subjects by Dunås et al. [27], [28] using a similar matching approach, and arteries were labeled in 10 clinical cases. Bilgel et al. [29] considered connection probability within the cerebral network using belief propagation for labeling 30 subjects but the method was limited to anterior circulations. Using the UNC dataset, in the serial work from Bogunović et al. [30]–[32], eight typical intracranial arteries graph templates were used to represent intracranial arteries with variations, and bifurcations of interest were defined and classified so that vessels were labeled indirectly. However, more variations exist beyond the eight typical types. Using the same dataset, by combining artery segmentation along with the labeling, Robben et al. [33] simultaneously optimized the artery centerlines and their labels from an over complete graph. However, their computation involved thousands of variables and constraints, and took as long as 510 seconds per case.

In summary, while previous works have shown success in labeling relatively small datasets with limited variations in mostly healthy populations, 1) prior knowledge about the global artery structures and relations has not been fully explored; 2) robustness of methods is unclear if the algorithms are not fully assessed on large diverse and challenging datasets; 3) labeling efficiency has not been considered for a large number of scans, which is needed for clinical applications.

2.3 VESSEL WALL SEGMENTATION

Vessel wall segmentation is the voxel-wise identification of areas belonging to lumen/vessel wall regions, so that quantitative features on vessel wall morphology can be quantified.

Vessel wall segmentation is challenging due to the small area of vessel wall and variable contrasts in outer wall boundaries. Many previous studies for quantitative analysis of vessel wall relied on manual vessel wall segmentation by drawing inner and outer boundaries of the arterial wall (lumen and outer wall) in each slice of MR image [34], which is tedious and subject to reader variability [35].

Semi-automated or automated methods have been proposed to segment vessel walls, such as using active contour models by Yuan et al. [36] and Adams et al. [37], active shape model by Underhill et al. [38], or using graph cut by Arias-Lorza and Petersen et. al. [39]–[41]. Another category of methods segment vessel wall area by classifying pixels into vessel wall regions and non-vessel wall regions using machine learning models [42], [43]. More recently, machine learning techniques, especially CNN methods become another approach for vessel wall segmentation, and achieved success on carotid arteries [44] and intracranial arteries [45]. CNN based methods rely heavily on well annotated labels, which might be challenging to find, and the segmentation quality might deteriorate for new datasets.

Due to the small artery size in vascular images, manually locating the artery of interest is required for most methods, but some methods try to automatically locate arteries by referring to registered MRA, in which lumen areas are better visualized [46]. In addition, Hough circle detection has been attempted to detect arterial centers under the assumption that arteries are circular in shape [47], which might not always be true. These methods reduce some manual steps and show reasonable agreements for images with high vessel wall contrast.

In summary, there are three major problems for existing vessel wall segmentation methods. 1) Extensive human input is still needed for most methods, including contour initialization [36], [37], seed point initialization [38]–[40], [42], [43], and registration of image sequences [46]. 2) Feedback from the automated segmentation models, for example, the confidence of the segmentation is usually not available, but might be useful for clinicians to manually check the problematic slices to ensure the segmentation quality. 3) The robustness of algorithms was not fully explored in previous studies likely due to the limited number of annotated samples in a specific vascular region.

2.4   VASCULAR FEATURE EXTRACTION

Artery structural features can be extracted from artery tracing results. Existing artery structural feature extraction methods apply to arteries up to different size levels and the number of available anatomical labels are diverse, leading to various number of vascular features available for analysis. [49], [50] are limited to four morphometric features (vessel number, radius, two tortuosity features) from each of the four anatomic regions (anterior/posterior left/right) of the intracranial arteries. Wright et al [51] used L-Measure, an open-source tool to quantify 19 morphometric features from six major arteries stemming from the circle of Willis (CoW). The limited number of vascular features cannot cover all morphometric features in each important region of the vascular tree.

Features for describing the atherosclerotic plaques can be quantified from the segmentation results, for example, vessel wall thickness, lumen/wall areas and normalized wall index (wall area/(lumen area + wall area)). Current work on vessel wall analysis usually focused on several cross-sectional slices from large arteries with simple structures (carotid arteries). Complete vessel wall assessment on the whole artery with both large and small sizes is rare (for example, vessel wall analysis along intracranial arteries). However, both artery structural and vessel wall features

are related with atherosclerotic plaque status. Lacking either part of features might limit the capability for detailed vascular analysis.

Besides quantitative vascular features, from the clinical perspective, additional information on which artery segments have vascular diseases with disease severity can provide assistance on vascular disease diagnosis. However, current vessel wall analysis is limited on extracting plaque features without the additional step of identification and classification of the segment of arteries with atherosclerotic lesions, partly due to the complexity in artery structures and labor-intensive annotations.

2.5   SUMMARY

Although individual vascular analysis algorithms have contributed on either artery tracing, artery labeling and vessel wall segmentation, none of the studies combined artery structural information, vessel wall information and vascular disease related information into a comprehensive *quantitative vascular map*. In addition, current vascular analysis is not usually applicable on both large and small arteries, may not have complete artery labeling categories, and some algorithms lack the necessary automation for large population studies. These limitations restrict the vascular image analysis capabilities.

Chapter 3. ARTERY CENTERLINE GENERATION

Finding the artery centerlines by artery tracing is the first step for vascular analysis. Artery centerlines (a list of points with 3D coordinate in the image space and the corresponding radius at each point) are ideal representations to quantify vascular structures and locate the analysis region. When artery anatomical names are associated with each centerline, arterial segment-specific features are available for region based detailed analysis.

Human vasculature has diverse anatomical structures requiring different approaches for centerline generation. 1) For arteries with relatively straight structures, such as carotid arteries, 3D vascular images have relatively similar 2D cross-sectional slices for vascular regions along one axis, which can be used to develop an efficient 2D artery detection + 3D tracklet refinement method for centerline generation (section 3.1). 2) For more tortuous intracranial arteries, for example, tracing arteries in 3D space is required for centerline generation, but it is more challenging due to the more complex geometry of intracranial arteries, thus a semi-automated method (*iCafe*) was developed to accurately trace arteries with manual supervisions on automated results (section 3.2). 3) When fully automated analysis is needed, *AICafe* (AI+iCafe) method was developed from processed *iCafe* results for fully automated artery tracing and labeling using artificial intelligence (AI) techniques. *AICafe* includes two important modules: deep open snake tracker (DOST) for artery tracing (section 3.3) and a graph neural network solution for artery labeling (section 3.4).

To further improve artery centerlines, especially for vascular images with low image qualities (for example, infant intracranial images with motion artifacts), an artery refinement algorithm was used to make corrections based on straightened curve planar reformation (CPR) view (section 3.5).

Section 3.7 listed examples of applying the centerline generation methods to various clinical applications.

Part of the contents from this chapter were described in details in our previous publications [48]–[56].

3.1   CENTERLINE GENERATION USING TRACKLET REFINEMENT

Ideally, when sliding through 2D slices of a 3D image in the direction perpendicular to the flow direction of an artery, vascular regions are represented in similar circular shapes in 2D slices. An example of multiple axial slices of a common/internal carotid artery is shown in Figure 3.1. The similarity of arteries in 2D slices indicates the feasibility of using an object tracking approach to identify the arteries. Similar to object tracking in videos, if the time axis in a video is considered as the depth axis in a 3D image, a tracking by detection approach can be applied in artery tracking in 3D space. For robust artery tracking, three steps, region of interest identification, lumen center detection followed by tracklet refinement, are required. First, a 2D artery detector was used to locate potential artery locations, then lumen centers were identified from lumen segmentation, and artery centerlines were generated through refinements using locations of arteries from neighboring slices.
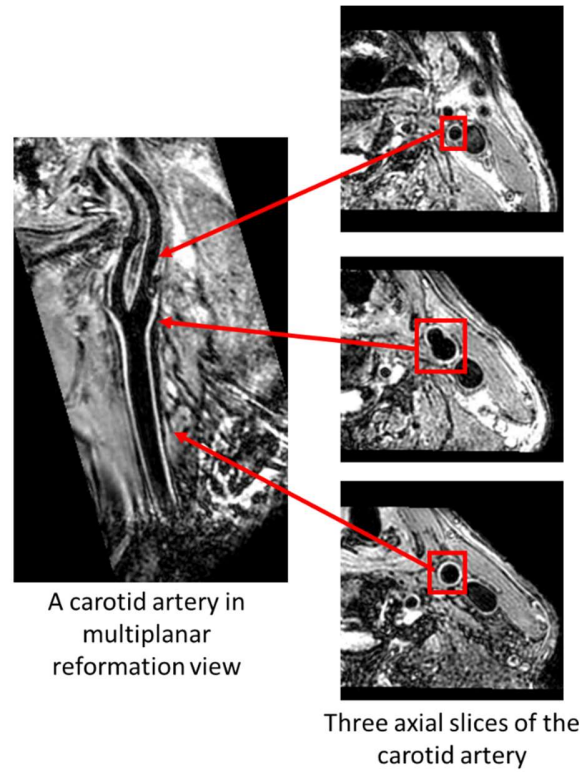
Figure 3.1 . An example of multiple axial slices of a common/internal carotid artery
(indicated by the red bounding boxes).

3.1.1   *Region of interest identification*

For artery detection, a Yolo V2 detector [57] based on CNN was used to predict bounding boxes (minimum encompassing rectangles covering whole artery regions) of arteries in each image slice with an artery detection score. The original weights of the Yolo detector were used to further train the model in artery detections given manual labels of artery bounding boxes.

3.1.2   *Lumen center detection*

Accurate patch extraction from the lumen center is important for the following artery analysis (such as vessel wall segmentation). However, the center of bounding boxes from the Yolo detector may not be the same as the geometric lumen center when the arterial shape is not a perfect circle

(Figure 3.2B shows an example). Instead, we predicted centers of the lumen near the bounding boxes using the following steps. First, a 2D U-net [58] was trained to predict the minimum distance to the nearest non-lumen area for each pixel. Then, the predicted minimum distance map was thresholded using the Otsu's method [59] and divided into connected components based on pixel connectivity. Components having no overlap with the bounding box were removed, and the centers of the remaining components were used to represent each possible lumen. The value of the minimum distance map at each lumen center was used as the confidence score for the centers.
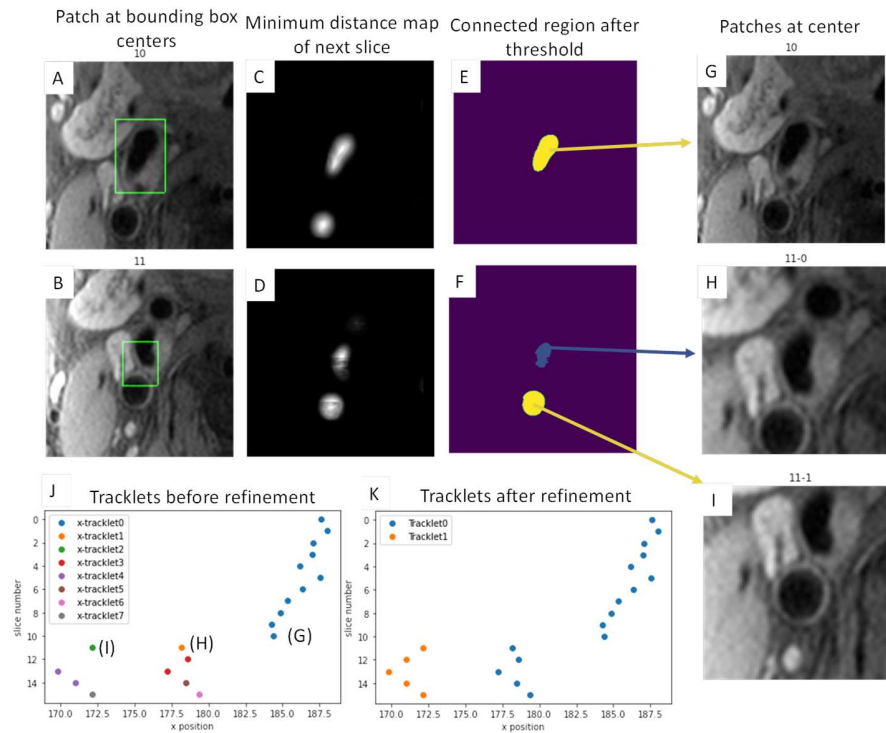
Figure 3.2 An example of centerline generation on carotid arteries.

A, B: Bounding boxes detected by Yolo V2 at slices 10 and 11 to identify rough artery locations.

C, D: Minimum distance map predictions.

E, F: Connected regions showing overlap with bounding boxes after threshold of C and D.

G: Patch from the connected region center (as lumen centers) of E.

H, I: Patches from two connected region centers from F.

J: Lumen centers of all slices form tracklets (x position vs z position).

K: Tracklets after refinement. The longest tracklet (blue) on each side of the carotid artery is used as the centerline for segmentation.

3.1.3   *Tracklet refinement*

When no, or multiple, lumen centers were identified for some slices, a tracking method (tracklet refinement algorithm) was used to infer the missing centers or remove centers corresponding to veins/arteries not of interest. First, a series of closely matching (based on intensities along the path between centers) neighboring centers were defined as a short tracklet. All short tracklets formed a collection of $K = \{T_1, T_2, \ldots, T_i\}$. Tracklet T_i with $z_{t,i} - z_{h,i} + 1$ neighboring centers was represented with head and tail centers $T_i = (\boldsymbol{h}_i, \boldsymbol{t}_i) = ([x_{h,i}, y_{h,i}, z_{h,i}], [x_{t,i}, y_{t,i}, z_{t,i}])$. Short tracklets were then merged for longer tracklets by a connection loss $L(T_i, T_j)$ defined as the feature distance between head and tail of each pair of tracklets,

$$L(T_i, T_j) = \begin{cases} \infty, \ z_{h,i} > z_{h,j} \\ \left\| F(C(\boldsymbol{t}_i)) - F\left(C(\boldsymbol{h}_j)\right) \right\|^2, z_{h,i} \leq z_{h,j} \end{cases} \tag{3.1}$$

C is a function to crop the in-plane image patch of 128*128 at the center of $\boldsymbol{h}$ or $\boldsymbol{t}$. F is a CNN feature extraction network with 5 convolution layers, 5 max pooling layers, and a fully connected layer of 64 nodes as the output. Triplet loss [60] $L_t(A, P, N)$ was used to train the feature extraction network, where the anchor and positive patches were extracted from ground truth lumen centers at the head and tail of the tracklets, and the negative patch was extracted from the same slice as the positive patch but at (one of) the center(s) of connected component(s) not encompassing lumen centers (an example is shown in Figure 3.3).

$$L_t(A, P, N) = \max\left(\left\|F(A) - F(P)\right\|^2 - \left\|F(A) - F(N)\right\|^2 + \propto, 0\right) \tag{3.2}$$

$\propto$ is the margin between positive and negative pairs. The default value of 0.4 was used for $\propto$ in this study.
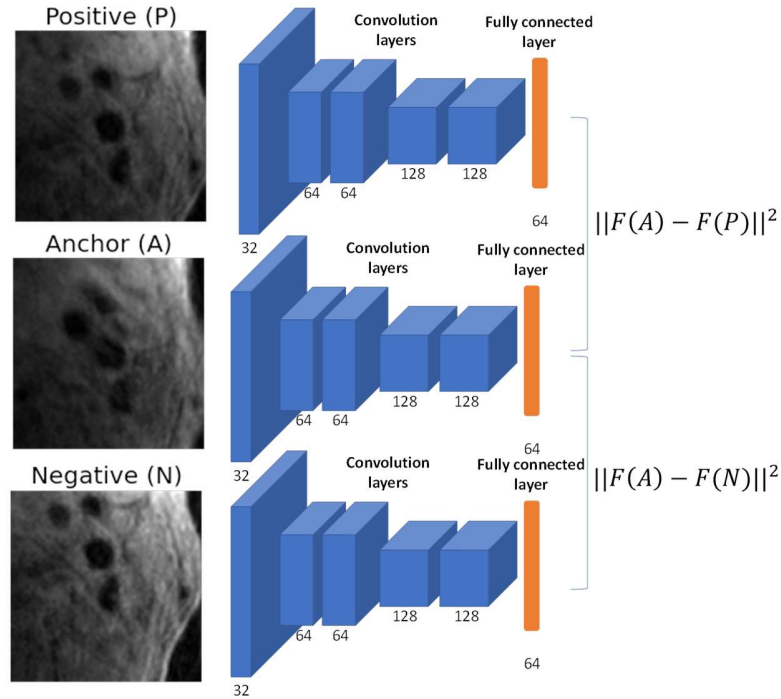
Figure 3.3 Feature extraction network and triplet loss for identifying pairs of tracklets to merge.

An anchor image patch (middle) was selected for training, along with a positive patch (top) from the same centerline and a negative patch (bottom) from a different centerline. Number of kernels are shown in each convolution layer.

Tracklets were pairwise calculated for connection losses, and the pair (i, j) with mutual minimum loss among all merge options were connected. $\min_i\{L(T_i, T_j)|T_j \in K\} = \min_j \{L(T_i, T_j)|T_i \in K\}$. During tracklet merging, missing lumen centers between slice $z_{h,i}$ and $z_{h,j}$ were linearly interpolated by T_i, T_j. Center confidence scores within the tracklet were summed up, and the tracklets with the top score on each side of the carotid artery were considered as the

target centerline. An example of using tracklet refinement to find the centerline when there are multiple centers for connection is shown in Figure 3.2 J K.

3.1.4   *Experimental results*

We applied the method on a carotid dataset, which included T1-weighted (T1W) carotid artery images of 954 patients with recent ischemic stroke or transient ischemia attack, which were collected from the CARE-II study from multiple sites across China [61], and 203 asymptomatic subjects from a clinical trial (NCT00851500; http://clinicaltrials.gov) for the Kowa Research Institute [62], [63]. Vessel wall contours were traced manually by trained reviewers with >3 years' experience in cardiovascular MR imaging using a custom-designed software package (CASCADE) [64]. Then the minimum encompassing boxes were derived to use as labels.

For the centerline evaluation, mean absolute distance (MAD) between predicted lumen centers with ground truth centers, number of false negatives (no lumen center in a slice) and false positives (more than one center in a slice) were calculated before and after the tracklet refinement.

The centerline evaluation results are shown in Table 3.1, after tracklet refinement, 31 (0.9%) FN centers and 211 (6.2%) FP centers from the carotid dataset were all corrected. The MAD improved from 2.60 to 1.58 pixels.

Table 3.1 Centerline generation performance before and after the tracklet refinement.

		MAD (pixel)	# FN	# FP
Carotid N=3406	Before refinement	2.60	31 (0.9%)	211 (6.2%)
	After refinement	1.58	0 (0.0%)	0 (0.0%)

3.1.5   *Summary*

The tracklet refinement approach is able to identify artery centerlines in an efficient framework. The approach is robust enough to handle missing and wrong artery detections by taking advantages of neighboring slice information, while the most significant limitation for this approach is its assumption that arteries are relatively straight.

More details of this approach can be found in our publication [53].

3.2   iCAFE FOR ARTERY TRACING AND LABELING

Compared with relatively straight carotid arteries, intracranial vasculature is much more challenging to generate centerlines, due to the smaller and more tortuous artery structures. To generate accurate artery centerlines, we developed a semi-automated intraCranial artery feature extraction (*iCafe*) technique [48]. Human is allowed to edit the automated tracing and labeling results from 3D MRA images in a graphical user interface (GUI). The workflow of iCafe is shown in Figure 3.4.
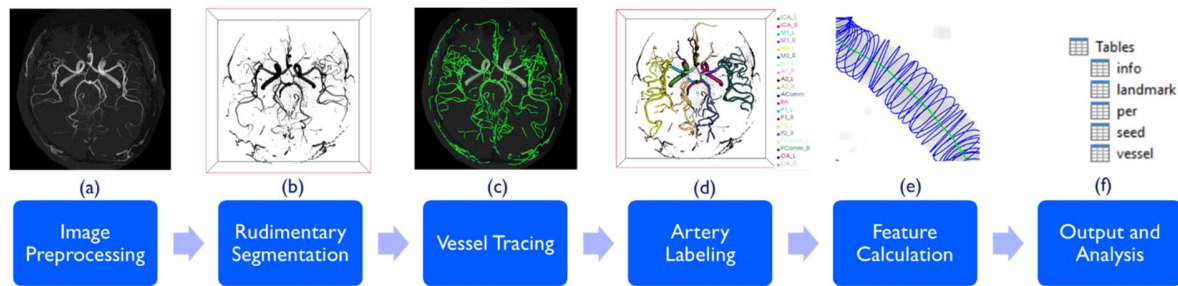
Figure 3.4 Workflow for *iCafe* (**i**ntra**C**ranial **a**rtery **f**eature **e**xtraction)

3.2.1   *Image preprocessing*

The original images were resliced in the axial direction of image acquisition using bi-cubic interpolation with isotropic resolution in 3D space. The absolute intensity values of MR images

do not have a fixed meaning, so a fast and accurate intensity normalization method by Nyul [65] is used to adjust intensities among cases in the database.

3.2.2 *Rudimentary segmentation*

For images with excessive noises hindering 3D visualization, a rudimentary segmentation of the artery region by the Phansalkar local threshold method [66] was optionally applied before artery tracing. The Phansalkar method was used due to its local thresholding ability with minimum loss of vascular regions in a reasonable processing time.

3.2.3 *Artery tracing*

Artery tracing represents arteries into radius varying tubes in the 3D space so that quantitative vascular features can be calculated. The open-curve active contour algorithm [24] originally designed for neural fiber tracing, was adapted for artery tracing in *iCafe*. Considering the different nature in arteries compared to neurons, for example, bifurcations are frequent in vasculature, but the areas near bifurcation are not enhanced in the vesselness image (Frangi vesselness filtered [67]), causing traces to be aborted near bifurcations, a combined tracing approach with both original image and vesselness image was used for artery tracing in *iCafe*. In the first stage, the tracing process started stretching from the seed point selected from centers of high intensity regions from the vesselness image. The current length of traced artery was calculated in each iteration. If the length increased slower than a preset threshold after an iteration, the trace was then stretched based on the raw image instead as a second stage until the length increase was below the threshold after an iteration again or until a maximum iteration number was reached. During each iteration, the radius on each point in the centerline was estimated using the method described in [19], where combined maximum gradients in eight directions were found at the radius boundary.

Manual editing was needed to correct the tracing errors in order to get the most accurate artery structures. A user-friendly GUI was provided (Figure 3.5) with five visualization methods (maximum intensity projection (MIP) view, 3D view, cross-section (CS) view, slice view, and multiplanar reformatted (MPR) view) for easier observation of artery details for human operators (Figure 3.6). The human correction time varies depending on complexity of data ranging from 20 minutes to one hour.
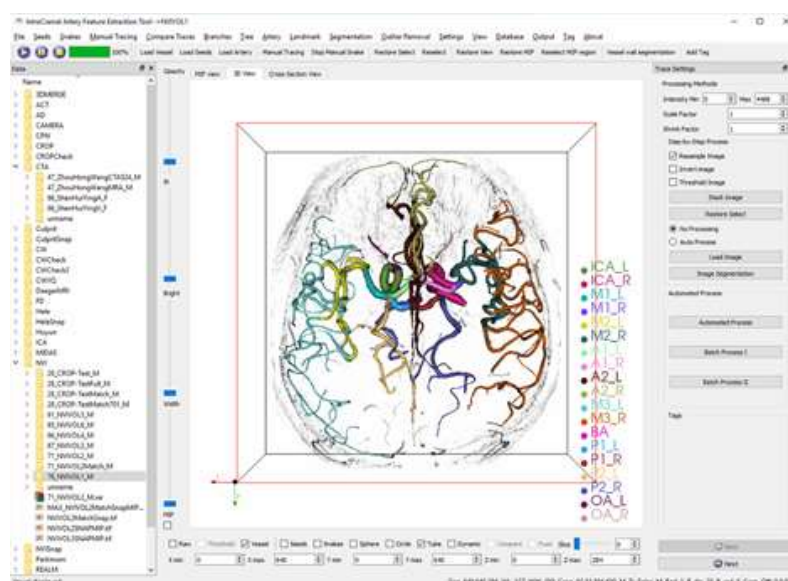
Figure 3.5 *iCafe* user interface with constructed intracranial artery centerlines displayed in 3D view.

CS view   MIP view   Slice view   MPR view
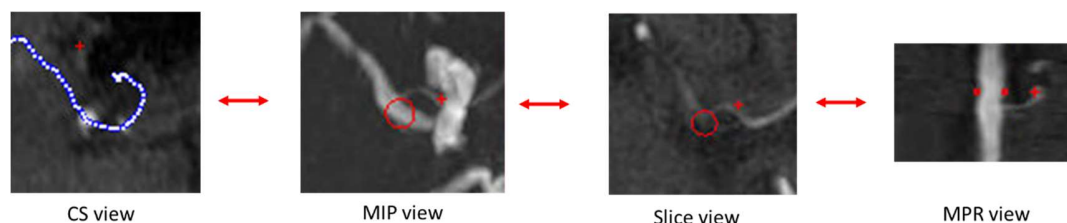
Figure 3.6 Different views for artery visualization in *iCafe*. Position and artery radius are linked in each view.

3.2.4   *Artery labeling*

An automated artery labeling method based on Maximum a Posteriori (MAP) estimation was used [55]. Before artery labeling, 31 types of bifurcations of Interest (BoI) were identified based on a probability model using the positional, directional and topological [68] features. Each artery could be labeled after all BoI types were assigned. Manual corrections were needed when there were mistakes in automated artery labeling.

3.2.5   *Feature extraction*

The twelve morphometric features (length, volume, tortuosity, etc.) and sixteen intensity features (max, min, average intensity) from each artery can be calculated from the generated artery centerline. With artery labels, arteries with similar geometric and anatomical properties can be further grouped based on anatomy and flow distribution, such as distal branch length, and total volume in anterior circulation. A total of 1456 vascular features per scan can be extracted using *iCafe*.

All the vascular features were well managed under a MySQL database retrievable through customized scripts.

3.2.6   *Summary*

The *iCafe* approach is able to generate artery centerlines and label arteries in a human-supervised semi-automated workflow. The benefits of using *iCafe* is its high accuracy and extensive vascular features available compared with existing artery tracing and feature extraction tools, but the accuracy comes with intensive human editing. Although *iCafe* analysis is time consuming, when enough cases with good quality labels are generated, this new artery tracing and

labeling dataset (1000+ cases) becomes valuable not only for various medical research but also for developing AI models to automate the artery analysis workflow (section 3.3 and 3.4).

More details of this approach can be found in our publication [48].

3.3   DEEP OPEN SNAKE TRACKER (DOST) FOR ARTERY TRACING

iCafe provides a solution for artery centerline generation with more complex structures at the cost of more human supervisions. Based on existing large datasets of *iCafe* processed results, we proposed a deep learning based active contour model called *Deep Open Snake Tracker* (*DOST*) for automated artery tracing.

DOST includes three key steps: curve proposal from centerline segmentation, deep snake tracing, and global tree construction (Figure 3.7).
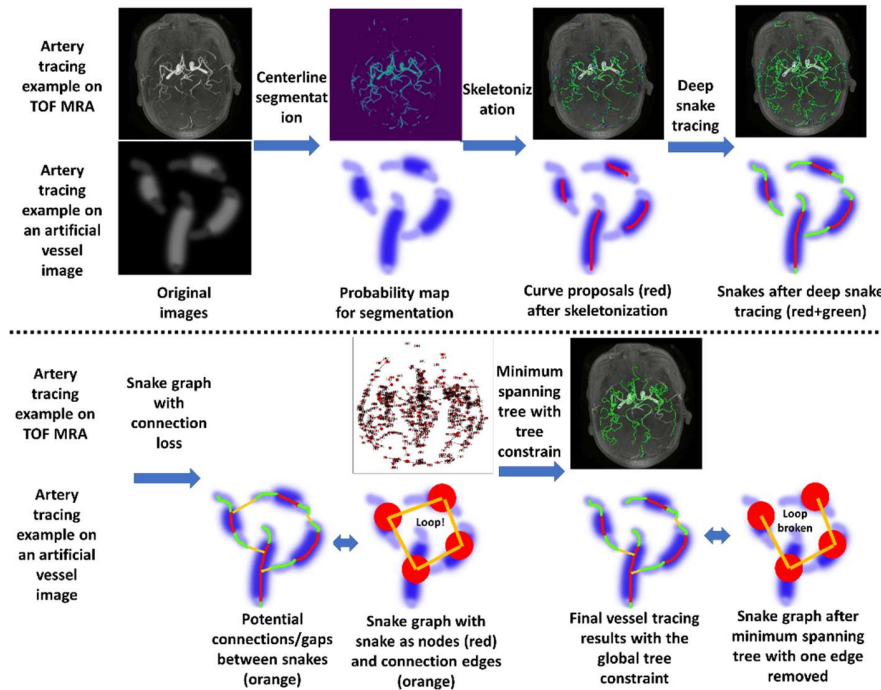
Figure 3.7 Workflow of *Deep Open Snake Tracker* (*DOST*).

Centerlines for arteries were identified by a centerline segmentation CNN and skeletonized into pieces of 1-voxel thin vessel curves, which were used as the initial traces for deep snake tracing. CNN predicted the stretching directions and radii for both ends of the snake while trace

smoothness and fitness to image intensities were maintained. Then a graph model was used to select and construct a topologically correct vascular tree.

3.3.1   *Curve proposal*

Instead of seed points [19], [22], *DOST* initializes from *vessel curves* predicted from the centerline segmentation, which better utilizes vascular structures from segmentation-based tracking methods to avoid initial stretching errors. A 3D patch-based encoder-decoder centerline segmentation network (2 blocks in encoder/decoder, each with two 3D convolutional layers + RELU followed by 3D max pooling/up sampling layers) was used for segmentation on the vascular images. To separate the nearby vessels, the centerline distance transform [18] was used to map the vascular regions with continuous values according to the distance to the centerline. Each voxel at $\boldsymbol{p} = [\boldsymbol{x}, \boldsymbol{y}, \boldsymbol{z}]$ within the radius ($r_{i,\mathrm{k}}$) of the artery i at the k th point was transformed into a labeled distance map d, where centerlines voxels had highest values.

$$d[x, y, z] = \max_i \max_k \left(\frac{\max\left(0, r_{i,\mathrm{k}} - \left\|\boldsymbol{p}_{i,\mathrm{k}} - \boldsymbol{p}\right\|\right)}{r_{i,\mathrm{k}}} \right) \tag{3.3}$$

Considering the majority of d is zeros. The L2 loss for training the segmentation network is masked by the non-zero regions in d. $\mathbf{1}(\cdot)$ is an indication function.

$$Loss_{seg} = \left\|\mathbf{1}(d[x, y, z] \neq 0)(d[x, y, z] - \hat{d}[x, y, z])\right\|_2 \tag{3.4}$$

Threshold after segmentation was chosen (from the validation set) to make binary predictions. Zhang's skeletonization algorithm [69] was applied to identify initial curves (grouped if voxels were 26-connected) for tracing.

3.3.2   *Deep snake tracing*

An initial curve $c(s)$ was represented as a parametric open curve model $(x(s), y(s), z(s)), s \in [0,1]$ The snake energy used in $DOST$ (E_{DOST}) was a combination of the internal energy E_{int} and the external energy of E_{ext}

$$E_{DOST} = \int_0^1 E_{int}(c(s)) + E_{ext}(c(s)) \, ds \tag{3.5}$$

$$E_{int}(c(s)) = \alpha(s)|c_s(s)|^2 + \beta(s)|c_{ss}(s)|^2 \tag{3.6}$$

"Elasticity" $\alpha(s)$ and "stiffness" $\beta(s)$ of the snake were set to be zero at $s = 0 \, or \, 1$ to allow snake stretching. c_s and c_{ss} indicate first and second order derivatives.

$$E_{ext}(c(s)) = -I(x(s), y(s), z(s)) + E_{str}(c(s)) \tag{3.7}$$

I is the image intensity. E_{str} is the energy for stretching directions at both ends of the snake. $E_{str}(c(s)) = 0$ for points other than both ends.

Different from the open curve snake (OCS), the stretching directions at the end of the snake were predicted from a deep neural network following the settings from the CNN tracker [22]. The network structure has 6 blocks followed by a convolution layer with $D + 1$ dimensions $(D = 500)$, each block was a 3D convolutional layer + batch normalization + RELU. A 3D image patch $P(c(s))$ with the size of 19^3 (large enough to cover the vessel diameter) was extracted centered at $c(s), s = 0, 1$ for prediction of the 1-dimensional radius $r(P(c(s)))$ and D-dimensional stretching direction $v_{m=1,2,..,D}(P(c(s)))$ by the network. The predicted stretching magnitudes $\{k_m\}$ has D dimensions indicating evenly distributed 3D unit directions v_m. The training targets for each patch were generated from semi-automatedly traced arteries using *iCafe*[48].

$$\nabla E_{str}(c(s)) = -\begin{cases} \max_m(sign(-c_s(s) \cdot v_m) \cdot k_m), s = 0 \\ \max_m(sign(c_s(s) \cdot v_m) \cdot k_m), s = 1 \\ 0, 0 < s < 1 \end{cases} \tag{3.8}$$

The directions of $-c_s(s)|s = 0$ and $c_s(s)|s = 1$ pointed outward from the curve, indicating the correct stretching directions for v_m to stretch the snake.

3.3.3   *Global tree construction*

Snakes were traced independently. In each iteration for a snake tracing, the snake stretches at both ends with the step size of $\gamma = 0.5r(P(c(s)))$ with minimized snake energy, then resampled evenly for the next iteration.

Snake stretching will terminate either when a snake end point reached another traced snake or the predicted direction v_m can no longer predict a confident direction indicated by the normalized entropy [22].

$$H = \frac{\sum_m -k_m \cdot log_2(k_m)}{log_2(D)} \tag{3.9}$$

Deep snake tracing can reliably trace individual arteries. However, traces were not connected with each other through merging or branching to form a topologically meaningful vascular tree. To solve this issue, the global constraint on tree structure (no loop) was used to fix connection errors in tracing. On rare occasions when loops naturally exist, such as in individuals with collateral arteries or with a complete circle of Willis, a manual step of loop reconnection is needed.

The vascular tree was constructed using an undirected *snake graph*, in which vertices indicated snakes, and edges between vertices indicated the connection loss $Loss_{con}(i,j)$ for the snake pair i,j (through merging or branching).

The connection loss $Loss_{con}(i,j)$ was based on intensities of point list $t_{i,j}$ from two snakes $c_i \cup c_j$ and their gap g_i (minimum distance from one point of the snake to any point on the other snake). Foreground intensities for the snake pair were estimated with normal distributions N_{i_f,δ_f}.

i_f, δ_f were mean and standard deviation of intensity along $t_{i,j}$. Background intensities for the snake pair were sampled from points at twice the radius around $t_{i,j}$ with normal distributions N_{i_b, δ_b}. i_b, δ_b were mean and standard deviation of background intensities. Mean intensity along g_i was i_g.

$$Loss_{con}(i,j) = \frac{N_{i_f, \delta_f}(i_g)}{N_{i_f, \delta_f}(i_g) + N_{i_b, \delta_b}(i_g)} \tag{3.10}$$

When $Loss_{con}(i,j)$ was below the threshold of 0.05 or the gap was above the maximum distance for connection consideration (10mm), edges were removed from the graph. Parameters were empirically chosen for the best vascular tree construction.

Kruskal's algorithm [70] was used for minimum spanning tree (MST) construction from the snake graph with connection losses. Edges in MST were used to fill the gaps for snakes to construct a whole vascular tree.

3.3.4 *Evaluations*

We used the BRAVE dataset [71], [72] with 167 TOF MRA from elderly hypertensive subjects to evaluate *DOST* comparing with state-of-the-art methods. To evaluate the robustness of *DOST* on more vascular beds and imaging modalities, we used 1) the Rotterdam Coronary Artery Challenge (CAT08): eight CTA scans for coronary artery tracing [73], and 2) Harborview dataset: clinical scans with MR vessel wall imaging using T1 SPACE (black blood) from 15 patients with history of stroke. Detailed dataset properties are described in Table 3.2. Ethics approval was waived due to the retrospective study design.

Table 3.2 Detailed properties for datasets used in *DOST* evaluation.

	Number of training/vali dation/teat cases	Modality	Vascular beds	Blood intensity in images	Interpolated in-plane resolution (mm)
BRAVE	117/25/25	TOF MRA	Intracranial	Bright	0.43
CAT08	6/1/1	CTA	Coronary	Black	0.36
Harborview	5/5/5	MR VWI (T1 SPACE)	Intracranial	Bright	0.56

Ground truth for CAT08 was provided. For other datasets, arteries were automatically generated by the OCS and manually corrected in *iCafe* [48], [74].

We evaluated the tracing accuracy following the metrics used in the CAT08 Challenge [73], including Average inside (AI) and Overlap (OV). However, AI and OV mainly evaluate centerline overlap for a single artery and cannot reflect the multi-vessel connection accuracy. For example, a vessel matched by two traces (Figure 3.8) has 100% OV but gets no penalties on additional broken predictions.
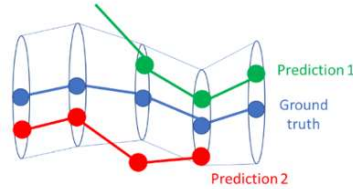
Figure 3.8 An example when overlap measures are high but traced by multiple traces.

Thus following multiple object tracking tasks [75], we adopted three 3D multi-vessel connection accuracy metrics: ID switch (IDS), multiple object tracking accuracy (MOTA) and IDF1 metrics to evaluate connection errors in vessel tracing.

The tracing target for each scan in our task is a constructed snake list $T = \{t_i, i = 1,2,...,N\}$ with N traces. Ground truth labels are annotated with hat symbols, for example, $\hat{T}$. After $\{t_i\}$ were

matched ($min_{i,k}$ ($||\boldsymbol{p}_{i,k} - \hat{\boldsymbol{p}}_{i,k}|| < \hat{r}_{i,k}$)) with $\{\hat{t}_i\}$, for each $\hat{t}_i$, ID switch IDS_i was defined as the

additional count of sources from the predicted $\{t_i\}$. TP was the number of $\{\hat{t}_i\}$ having matching

t_i, FN was the number of $\{\hat{t}_i\}$ having no matching t_i, and FP was the number of $\{t_i\}$ having no

matching $\hat{t}_i$. T was the number of points in $\{\hat{t}_i\}$. $MOTA$ penalizes FP, FN as well as IDS, leading

to the best possible value of 1. $IDF1$ is the F1 score for artery matching ranging from 0 to 1, with

lower score either by larger FP or FN.

$$IDS = \sum_i IDS_i \qquad (3.11)$$

$$MOTA = 1 - \frac{FN+FP+IDS}{T} \qquad (3.12)$$

$$IDF1 = \frac{2 \cdot TP}{2 \cdot TP + FP + FN} \qquad (3.13)$$

3.3.5 *Experimental results*

Comprehensive quantitative comparisons with *DOST* were made with traditional and deep learning

methods. For segmentation-based approaches, Frangi vesselness filter [67], U-Net [58] and Deep

Distance Transform (DDT) [18] were selected. For tracking-based approaches, OCS [24], CNN-

tracker [22] and Discriminative Coronary Artery Tracking (DCAT)[23] were selected. Results

were shown in Table 3.3.

Table 3.3 Quantitative comparison results for intracranial artery tracing

Tracing approach	Model name	OV↑	AI↓	MOTA↑	IDF1↑	IDS↓
Traditional segmentation	Frangi	0.617	0.956	0.238	0.621	343.9
Deep learning segmentation	U-Net	0.662	0.724	0.300	0.696	398.3
Deep learning segmentation	DDT	0.683	0.703	0.281	0.712	423.0
Traditional tracking	OCS*	0.672	**0.356**	**0.372**	0.694	**74.8**
Deep learning tracking	CNN tracker	0.562	0.860	-0.312	0.595	108.5

Deep learning tracking	*DCAT*	0.564	0.943	-0.241	0.601	137.8
Hybrid	*DOST* (Our)	**0.732**	0.592	0.318	**0.731**	104.1

* Ground truth was modified manually based on OCS results

DOST showed higher performance than most methods. Note that the ground truth was generated based on OCS, which was a natural bias. An example of artery tracing on an MRA data is shown in Figure 3.9.
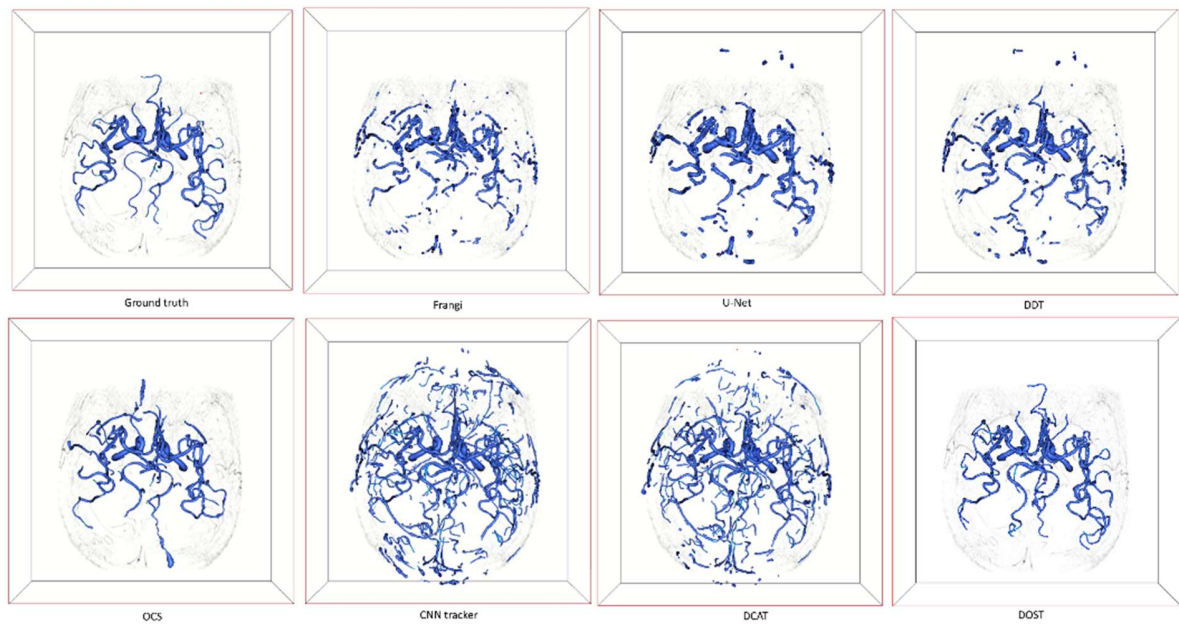
Figure 3.9 An example of artery tracing for comparison.

DOST did not have the problem in segmentation-based method for broken arteries, and it considered global tree structures in tracing, thus avoiding loops or many noise branches.

3.3.6   *Summary*

A deep learning based open curve snake model (*DOST*) was developed and evaluated. *DOST* combines deep learning-based direction prediction/radius estimation and the classic parametric curve modeling. It allows data driven machine learning knowledge to complement human prior knowledge on the structure of vessels (smoothness and stretchiness) and the topology of the

vasculature, so that *DOST* out-performed existing models with either human or machine knowledge. In addition, *DOST*, as an adaptive hybrid (segmentation and tracking-based) tracing method, is able to identify complete vascular trees from multiple vascular beds and modalities.

The main limitation of *DOST* is its requirement of supervised training to get the initial curve proposals and predict stretching directions. The training labels requires detailed semi-automated artery tracings[48]. However, we have demonstrated *DOST* works even with 6 cases in CAT08 and 5 cases in Harborview dataset.

More details of this approach can be found in our publication [56].

3.4 GRAPH NEURAL NETWORK + HIERARCHICAL REFINEMENT FOR ARTERY LABELING

Labeling arteries after tracing is a necessary step to identify region of interest, as well as to calculate region based vascular features. This task is especially challenging when there is a complex structure of vasculature such as intracranial arteries. Substantial variations of intracranial arteries exist among individuals that are either healthy or associated with vascular disease [76]–[78], which makes automated artery labeling challenging.

The Graph Neural Network (GNN) is an emerging network structure recently attracted significant interest [79], [80], including applications on vasculature [81], [82]. By passing information between nodes and edges within the graph, useful properties for the graph can be predicted. Considering the graph topology in anatomical structures of intracranial arteries, we propose a GNN model with hierarchical refinement (HR), aiming to overcome the challenges in arterial labeling by training with large and diversely labeled datasets (more than 500 scans in the training set from multiple sources) and applying refinements after network predictions to combine prior knowledge on intracranial arteries.

3.4.1   *Graph neural network*

The intracranial artery network is represented as the centerlines of arteries, each with consecutively connected 3D points with radius. Centerlines in one MRA scan are constructed as an attributed relational graph $G = (V, E)$. $V = \{v_i\}$ represents all unique points in the centerlines with node features of v_i, and $E = \{e_k, r_k, s_k\}$ represents all point connections where edge k connects between the node index r_k, s_k with edge features of e_k. $e(i)_{1,\dots,D(i)}$ are all the edges connected with node i ($r_k = i$ or $s_k = i$). $D(i)$ is the degree (number of neighbor nodes) of node i.

Features for node v_i include p_i for x, y, z coordinates, r_i for radius and b_i for the directional embedding of the node. Due to the uncertain number of edges connected to the node, direction features cannot be directly used as an input in GNN. Here we use the multi-label binary encoding to represent direction features. First, 26 major directions in the 3D space are defined as $n_u = (x_u, y_u, z_u)_{u=1,\dots,26}$, with 45 degrees apart in each axis, excluding duplicates.

$$\begin{cases} x = \sin(45° * a) * \cos(45° * b) \\ y = \cos(45° * a) * \cos(45° * b), \ a \in \{0, \dots, 7\}, b \in \{-2, \dots, 2\} \\ \quad\quad z = \sin(45° * b) \end{cases} \quad (3.14)$$

Then each edge direction (x_v, y_v, z_v) originating from the node is matched with the major directions with $dir_v = argmax_u(x_u x_v + y_u y_v + z_u z_v)$. b_i is the 26-dimensional feature with encoded direction for all dir_v. (an example in Figure 3.10)
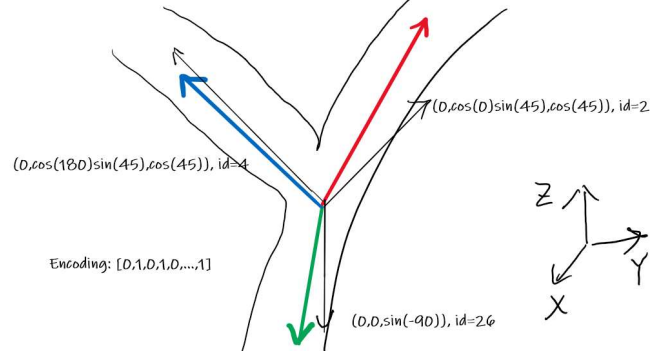
Figure 3.10 Illustration of direction encoding as the node feature.

Red, blue and green arrows indicate the edge directions for the node (bifurcation in this case). The closest major directions (with direction and id) are shown in black arrows near the edges. The indexes of these black arrows are used to construct the one hot encoding for this node.

Features for edges e_k include edge direction $\boldsymbol{n}_k = (\boldsymbol{p}_{s_k} - \boldsymbol{p}_{r_k})$, which is then normalized (and inverted) so that $||\boldsymbol{n}_k|| = 1$ and $z_k > 0$; distance between nodes at two ends $d_k = ||\boldsymbol{p}_{s_k} - \boldsymbol{p}_{r_k}||$; and mean radius at two nodes $\bar{r}_k = (r_{s_k} + r_{r_k})/2$.

With similar purpose of labeling using BoI instead of directly on arteries [30]–[32], we remove all nodes with a degree of 2 to reduce the graph size, as nodes requiring labeling are usually at bifurcations or ending points. If the remaining nodes are correctly predicted as one of the 21 possible bifurcation/ending types, then the intracranial arteries (edges) can be labeled based on their connections.

We implemented the GNN based on the message passing GNN framework proposed in [80], [83] to predict the types for each node and edge. The GNN takes a graph with node and edge features as input and returns a graph as output with additional features for node and edge types. The input features of edges and nodes in the graph are encoded to an embedding in the encoder layer. Then the core layer passes messages for 10 rounds by concatenating the encoder's output with the previous output of the core layer. The embedding is restored to edge and node features in

the decoder layer with additional label features. Computation in each graph block is shown in

equation (3.15). The edge attributes are updated through the per-edge "update" function $\emptyset^e$, and

features for edges connected to the same node are "aggregated" through function $\rho^{e \to v}$ to update

node features through the per-node "update" function $\emptyset^v$. The network structure is shown in Figure

3.11.

$$\begin{cases} updated\ edge\ attributes\ \boldsymbol{e}'_k = \emptyset^e\left(\boldsymbol{e}_k, \boldsymbol{v}_{r_k}, \boldsymbol{v}_{s_k}\right) \\ updated\ edge\ attributes\ per\ node\ \bar{\boldsymbol{e}}_i' = \rho^{e \to v}\left(\{(\boldsymbol{e}'_k, r_k, s_k)\}_{r_k=i}\right) \\ updated\ node\ attributes\ \boldsymbol{v}'_i = \emptyset^v(\bar{\boldsymbol{e}}_i', \boldsymbol{v}_i) \end{cases} \quad (3.15)$$
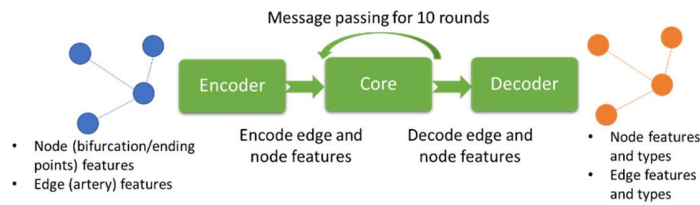
Figure 3.11 GNN structure used in the artery labeling method.

The artery names and abbreviations used in this labeling method is shown in Table 3.4.

Table 3.4 Abbreviation and definition of intracranial arteries used in the artery labeling
method.

Abbreviation	Artery Segment	Definition
ICA_L, ICA_R	Internal Carotid Artery on left/right side	Proximal to the bifurcation of ICA into M1 and A1
M1_L, M1_R	Middle Cerebral Artery on left/right side	From the bifurcation of ICA to the first major bi(tri)furcation of MCA
M2_L, M2_R		The rest of the distal branches of MCA
A1_L, A1_R	Anterior Cerebral Artery on left/right side	From the bifurcation of ICA to AComm
A2_L, A2_R		The rest of the distal branches of ACA (A2/3)
AComm	Anterior Communicating Artery	The connecting segment between left and right A1

VA_L, VA_R	Vertebral Artery on left/right side	Proximal to the converging point of left and right VA into BA
BA	Basilar Artery	From the converging point of VAs to the bifurcation of BA into left and right PCA
P1_L, P1_R	Posterior Cerebral Arteries on left/right side	From the bifurcation of BA to PComm
P2_L, P2_R		The rest of the distal branches of PCA (P2/3)
PComm_ L, PComm_ R	Posterior Communicating Arteries on left/right side	The connecting segment between ipsilateral ICA and PCA
OA_L, OA_R	Ophthalmic Artery on left/right side	The branch originating from the siphon of ICA coursing towards the eye

Probability $P_{nt}(i)$ for node i being bifurcation/ending type $nt \in \{0: Non\_Type, 1: ICA\_Root\_L, ..., 20: ICA\_PComm\}$ is calculated using a softmax function of GNN output $O_{nt}(i)$. The predicted node type $T_n(i)$ is then identified by selecting the node type with the maximum probability.

$$P_{nt}(i) = \frac{e^{O_{nt}(i)}}{\sum_{nti=0}^{20} e^{O_{nti}(i)}} \tag{3.16}$$

$$T_n(i) = argmax_{nt}(P_{nt}(i)) \tag{3.17}$$

Similar for edges, $et \in \{0: Non\_Type, 1: ICA\_L, ..., 22: OA\_R\}$, the edge probability and predicted edge type are

$$P_{et}(k) = \frac{e^{O_{et}(k)}}{\sum_{eti=0}^{22} e^{O_{eti}(k)}} \tag{3.18}$$

$$T_e(k) = argmax_{et}(P_{et}(k)) \tag{3.19}$$

Ground truth types for nodes and edges are $G(i), G(k)$.

The GNN was trained using combined weighted cross entropy losses in both nodes and edges, with weights inverse proportional to frequencies of the node and edge types. Batch size of 32 graphs was used in training the GNN. Adam optimizer [84] was used for controlling the learning

rate. Positions of nodes from different datasets were normalized based on the imaging resolution, and a random translation of positions (within 10%) was used as the data augmentation method.

3.4.2 *Hierarchical refinement*

Predictions from the GNN might not be perfect, as end-to-end training cannot easily learn global intracranial artery structures and relations. Logically, human reviewers are likely to subdivide intracranial arteries into three sub-trees (i.e., left/right anterior, posterior cerebral trees), find key nodes (such as the bifurcation for ICA/MCA/ACA) in sub-trees, and then add additional sub-branches more prone to variations (such as PComm, AComm). Enlighted by the sequential behavior during manual labeling, a hierarchical refinement (HR) framework based on GNN outputs is proposed to further improve the labeling. Starting from the most confident nodes, the three-level refinement is shown in Figure 3.12.
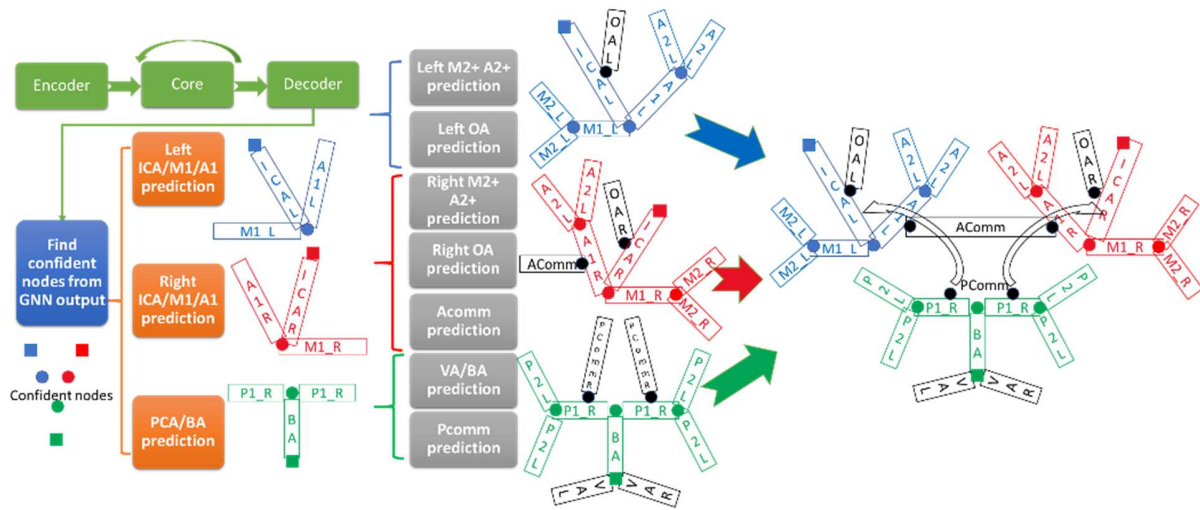
Figure 3.12 Workflow of HR framework.

In the first level (blue box), confident nodes (circle and square dots) are identified from the GNN outputs. In the second level (orange boxes), confident nodes as well as their inter-connected edges in the left (blue lines)/right (red lines) anterior, posterior (green) sub-trees are identified. In the third level (grey boxes), optional nodes and edges (black lines) are added to each of the three sub-trees to form a complete artery tree.

Level one labeling. We consider nodes as confident if the predicted node type fits the predicted edge types in edges they are connected with.

$$F\left(\{T_e\left(e(i)_{1,\ldots,D(i)}\right)\}\right) = T_n(i) \tag{3.20}$$

F is a lookup table with human prior knowledge for all valid pairs of edge types and node types. For example, $F(P1\_L, P1\_R, BA) = PCA/BA$, $F(ICA\_L) = ICA\_ROOT\_L$.

Level two labeling. From confident nodes, three sub-trees are built, and major-branch nodes are predicted in each sub-tree individually. Major node i is defined as ICA/MCA/ACA (for anterior trees) and PCA/BA (for posterior trees), and branch nodes j are defined as ICA_Root, M1/2, A1/2 (for anterior trees) and BA/VA, P1/2 (for posterior trees). If major nodes are not confident nodes in each sub-tree, they are predicted with type $argmax_i\ (P_{nt_i}(i)|D(i) \neq 1)$ with additional constraints if branch nodes j are confident ($i \notin j$ and i must be in the path between any pair of j). Then from the major node, all unconfident branch nodes are predicted using the target function of

$$\begin{cases} argmax_j\ \left[P_{nt_j}(j) + P_{et_{e(i)}}\left(e(i)_{1,\ldots,D(i)}\right)_{r_{e(i)}=j,s_{e(i)}=i}\right], if\ P_{nt_i}(i) > Thres \\ argmax_j\ \left(P_{nt_j}(j)\right), if\ P_{nt_i}(i) < Thres \end{cases} \tag{3.21}$$

On rare occasions, when the major nodes have a probability lower than a certain threshold $Thres$ (when there are anatomical variations where major nodes do not exist), branch nodes are predicted without edge probability.

If certain distance between the optimal i and j is beyond the mean plus 1.5 standard deviation of $G(k)|r_k = j, s_k = i$ from the training set, labeling on j will be skipped and a node with a degree of 2 will be labeled so that its distance to node i is closest to the mean distance of $G(k)$. This happens when there are missing Acomm or Pcomm.

Level three labeling. Optional branches are added to three sub-trees. M2+, A2+, and P2+ edges are assigned for all distal neighbors of M1/2, A1/2, P1/2 nodes. Based on node probabilities, OAs are identified on the path between ICA_Root and ICA/MCA/ACA nodes, Acomm is assigned if there is a connection between A1/2_L and A1/2_R, Pcomm is assigned if there is connection between P1/2 and ICA/MCA/ACA, VA_Root is predicted from neighbors of BA/VA.

3.4.3   *Datasets*

Five datasets from our previous research [50], [72], [85] were used to train and evaluate our method, then the generalizability was assessed on the public UNC dataset with/without further training. Details for the datasets are in Table 3.5.

Table 3.5 Properties of datasets used in the artery labeling method.

Datasets	Number of scans (training/validation/testing)	In-plane resolution after interpolation(mm)	Coverage	Scanner manufacturer	Health state	Source of scan
Our 1	117/25/25	0.352	Partial brain centered at M1	Philips	Healthy	Research project
Our 2	117/25/25	0.430		General Electric	Hypertension	Research project
Our 3	111/32/17	0.391		General Electric	Stroke	Research project
Our 4	111/24/28	0.400		Philips	Parkinson Disease	Clinical scan
Our 5	46/10/10	0.469		General Electric	Dementia	Clinical scan
Public UNC	0/0/41	0.513	From M1 to top of skull	SIEMENS	Healthy	Research project

Our five datasets were collected with different resolutions using different scanner manufacturers from different population, adding difficulties to artery labeling due to various levels

of traceable arteries, anatomical variations and disease related pathological changes. Subjects enrolled in the datasets include both healthy (no recent or chronic vascular disease) and with various vascular related diseases, such as recent stroke events and hypertension. All the datasets were randomly divided into a training set (508 scans), a validation set (116 scans) and a testing set (105 scans). If the subject had multiple scans, these scans were assigned into the same set. All scans from the UNC dataset ([https://public.kitware.com/Wiki/TubeTK/Data, healthy volunteers](https://public.kitware.com/Wiki/TubeTK/Data)) with publicly available artery traces (N=41) were used for further evaluations like previous studies [32], [33]. Generally, our dataset has more intracranial artery variations and more challenging anatomies than the UNC dataset.

3.4.4   *Evaluation*

Evaluation metrics. As our purpose is to label the intracranial arteries, the accuracy of predicted node labels is the primary metric for evaluation (Node_Acc). In addition, we also used number of wrongly predicted nodes per scan (Node_Wrong), edge accuracy (Edge_Acc) and the percent of scans with CoW nodes (ICA/MCA/ACA, PCA/BA, A1/2, P1/2/PComm, PComm/ICA), all nodes and all edges correctly predicted (CoW_Node_Solve, Node_Solve, Edge_Solve). For detailed analysis of detection performance on each bifurcation type, the detection accuracy, precision and recall for 7 major bifurcation types (ICA-OA, ICA-M1, ICA-PComm, ACA1-AComA, M1-M2, VBA-PCA1, PCA1-PComA) were calculated. The processing time was also recorded. Due to the lack of criteria for labeling nodes with degrees of 2, nodes such as A1/2 without AComm were excluded from the evaluation.

Comparison methods. With the same artery traces of our dataset, three artery labeling methods introduced in section 2.2 [26], [28], [48] were used to compare the performance. Due to the unavailability of two methods using the UNC dataset, we only cite evaluation results from their

publications. Direction features and HR were sequentially added to our baseline model to evaluate the contribution of different features and the effectiveness of the HR framework.

Ablation study. We compared the performance of GNN without HR (predicts node and edge types directly from the GNN outputs $T_n(i)$ and $T_e(k)$). We further tested the removal of direction features.

3.4.5   *Experimental results*

In the testing set of our dataset, 1035 confident nodes (9.86/scan) were identified, and 5 of them (0.5%, none are major or branch nodes) were predicted wrongly, showing labeling of confident nodes is reliable, so that labeling in the following up levels in HR was meaningful. Examples of correctly labeling challenging cases are shown in Figure 3.13. Our method was robust, even with artificial noise branches added in the M1 branch shown in Figure 3.13 (d).
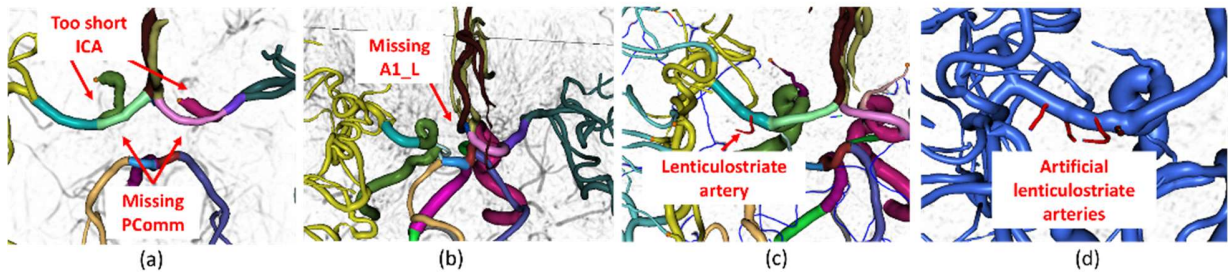
Figure 3.13 Examples of challenging anatomical variations where our method predicted all arteries correctly.

(a) A subject with Parkinson's disease. Occlusions cause both right and left internal carotid arteries to be partially invisible. In addition, Pcomms are missing.

(b) A hypertensive subject with rare A1_L artery missing, which is not among the 8 anatomical types and thus not solvable in [32].

(c) Some lenticulostriate arteries are visible in our dataset with higher resolution, an additional challenge for labeling, our method predicted it correctly as a non-type.

(d) With more artificial lenticulostriate arteries added in the M1_L segment, our method is still robust to these additional noise branches.

The comparison with other artery labeling algorithms and the ablation study is shown in Table 3.6. Our method demonstrates a better node accuracy of 97.5% with 3.0 wrong nodes/scan. Our method is the only one with cases where all nodes and edges were predicted correctly with the minimum processing time (less than 0.1 seconds). With direction features and the HR added to the baseline model, the performance is further improved. ICA-OA is the most accurately detected bifurcation type with detection accuracy of 96.2% while the challenging M1/2 has an accuracy of 68.1%. Mean detection accuracy is 83.1%, precision is 91.3%, recall is 83.8%.

Table 3.6 Comparison with existing methods and the ablation study on our testing set (N=105).

Method	Node_ Acc↑	Node_ Wrong ↓	Node_ Solve↑	CoW_ Node_ Solve↑	Edge_ Acc↑	Edge_ Solve↑	Process time (s) ↓
MAP [48]	0.9153	10.0	0	0.0476	0.3304	0	1.075
Template [26]	0.7316	31.6	0	0.0476	0.7934	0	5.057
Atlas [28]	0.8856	13.5	0	0.0095	0.7010	0	9.253
GNN(Pos)	0.9553	5.3	0.0286	0.3524	0.9099	0	**0.017**
GNN(Pos+Dir)	0.9637	4.3	0.0381	0.4286	0.9223	0	0.020
GNN(Pos+Dir)+HR	**0.9746**	**3.0**	**0.3238**	**0.6381**	**0.9246**	**0.3238**	0.092

Our labeling method showed good generalizability on the UNC dataset. Even without additional training on the UNC dataset, the node accuracy was 99.03% (2.0 wrong nodes/scan on all levels of labeling) with 56% of cases solved. Mean detection accuracy for all node types was 92%. As a reference with methods using leave-one-out cross validation trained and evaluated using the same dataset, 58% of cases were solved [32]. The mean detection accuracies were 94% and 95% in [32], [33], respectively. If trained in combination with the UNC dataset using three-fold cross validation, our method outperforms [32], [33].

TABLE 3.7 Performance of detection accuracy (A), precision (P) and recall (R) for each bifurcation type, compared with previous methods using the UNC dataset.

Note that our method is trained with our dataset with (GNN+HR+UNC) and without (GNN+HR) further training in the UNC dataset, but other methods were trained and evaluated by leave-one-out cross validation on the UNC dataset alone (more likely to overfit on the UNC dataset).

Method	GNN+HR (Ours)			GNN+HR+UNC (Ours)			Robben [33]			Bogunović [32]		
	A	P	R	A	P	R	P	R	R	A	P	R
ICA-OA	97	100	97	100	100	100	99	99	100	99	100	99
ICA-M1	90	96	93	95	97	97	100	100	100	99	99	100
ICA-PComm	88	97	89	95	97	97	98	100	98	93	94	96
ACA1-AComA	95	100	95	96	100	96	96	100	95	92	93	97
M1-M2	90	95	95	95	97	97	78	78	100	89	89	100
VBA-PCA1	94	97	97	90	94	94	90	98	91	94	100	93
PCA1-PComm	90	97	92	92	98	94	95	100	92	96	100	94
Mean	92	**97**	94	**95**	**97**	**97**	94	96	**97**	**95**	96	**97**

3.4.6 *Summary*

We have developed a GNN approach to label intracranial arteries with HR on our comprehensive intracranial artery labeling dataset (729 scans). In addition to its superior performance compared with methods described in the literature, our work shows robustness and generalizability on various challenging anatomical variations.

Four contributions and novelties in our work are worth highlighting. 1) The dataset includes more diverse and challenging intracranial artery variations compared with the existing UNC dataset, which is better suited to evaluate labeling performance. 2) The GNN and HR framework is an ideal method to learn from the graph representation of intracranial arteries and incorporate prior knowledge about intracranial artery structure. 3) With accurate predictions of 20 node and

22 edge types covering all major artery branches visible in MRA, this method can automatically provide comprehensive features for detailed analysis of cerebral flow and structures in less than 0.1 seconds. 4) It should also be noted that our GNN and HR framework is not only applicable to intracranial arteries, but also to any graph structures where sequential labeling helps.

More details of this approach can be found in our publication [52].

3.5   ARTERY REFINEMENT ON TRACES FROM LOW QUALITY IMAGES

Arteries are long tubular structures. By knowing this property, the traces can be further refined, which can be especially useful when image quality is poor, for example, motion affected infant MRA. Construction of the straightened curve planar reformation (CPR) view is an ideal image conversion method to represent and refine arteries, as the vertical axis of straightened CPR represents longitudinal direction of an artery and the horizontal axis represents one of the profiles in neighboring cross-sectional planes. An example of straightened CPR view of an intracranial artery is shown in Figure 3.14.
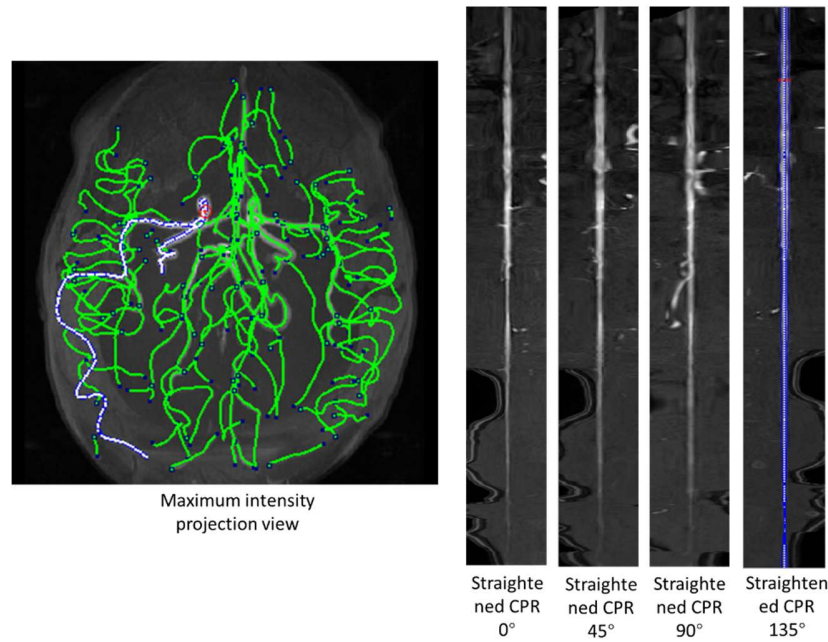
Figure 3.14 MIP and straightened CPR view of an example artery.

Left: MIP view with selected trace in blue. Right: straightened CPR view at angles of 0, 45, 90, and 135°. The radius along the centerline is shown in blue in the straightened CPR 135° angle image.

An artery refinement algorithm was developed and validated for robust quantification of intracranial vasculature from MRA in this section (extensible to other MRI sequences) using the straightened CPR. The refinement includes adjustments on centerline positions, lumen radii and centerline deviations, so that smooth artery traces are following vascular regions with radius fitting lumen boundaries.

3.5.1   *Artery refinement algorithm*

For an individual artery trace, the refinement algorithm uses both the signal intensity gradient from the cross-sectional plane and neighboring information along the centerline, to improve artery boundary delineation and radius smoothness. First, a straightened CPR view is generated. Then,

the artery tracing is optimized in three stages: 1) trace position optimization, 2) trace radius optimization, and 3) trace deviation correction.

Straightened CPR view generation. The directions along the centerline can be represented as normal vectors $\boldsymbol{n}_i = (x_i, y_i, z_i)$. Based on the orthogonal relations of normal directions and coordinate axes, the cross-sectional plane $C_i(u, v) = (u \cdot (x_u, y_u, z_u), v \cdot (x_v, y_v, z_v))$ for normal direction $\boldsymbol{n}_i$ can be generated from

$$
\begin{cases}
x_u = \dfrac{y_i^2 + z_i^2}{\sqrt{(y_i^2 + z_i^2)^2 + x_i^2 y_i^2 + x_i^2 z_i^2}} \\
y_u = -\dfrac{x_i y_i}{\sqrt{(y_i^2 + z_i^2)^2 + x_i^2 y_i^2 + x_i^2 z_i^2}} \\
z_u = -\dfrac{x_i z_i}{\sqrt{(y_i^2 + z_i^2)^2 + x_i^2 y_i^2 + x_i^2 z_i^2}} \\
x_v = 0 \\
y_v = \dfrac{z_i}{\sqrt{y_i^2 + z_i^2}} \\
z_v = -\dfrac{y_i}{\sqrt{y_i^2 + z_i^2}}
\end{cases}
\tag{3.22}
$$

when y_i and z_i are not zero at the same time. An illustrative graph is shown in Figure 3.15.
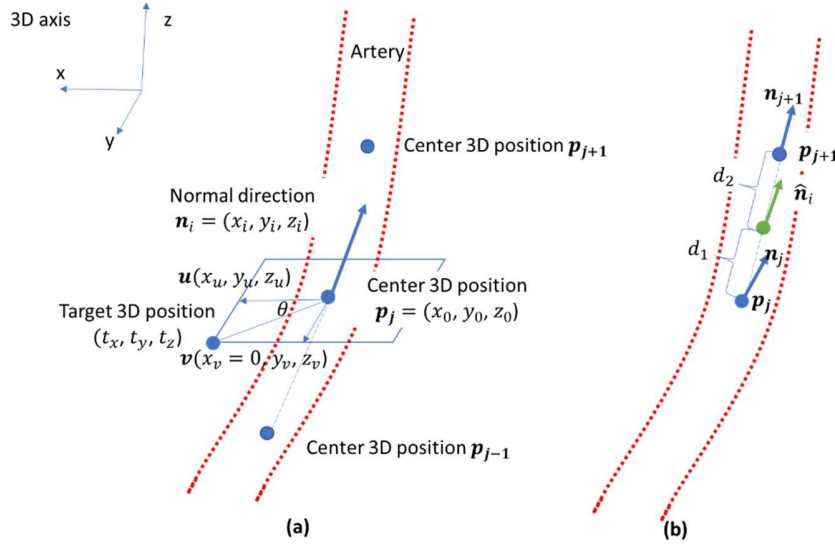
Figure 3.15 Illustration graph for straightened CPR view generation.

(a) a cross-sectional plane (blue rectangle) at center position $\mathbf{p}_j$ is defined by normal vector $\mathbf{n}_i$, any target position can be defined in the cross-sectional plane by two orthogonal vectors $\mathbf{u}$ and $\mathbf{v}$.

(b) interpolated normal direction at the position between two center positions is the linear interpolation between two neighboring normal vectors $\mathbf{p}_j$ and $\mathbf{p}_{j+1}$ according to their distances to center positions.

As the cross-sectional plane to a normal vector is not unique, $x_v = 0$ is chosen as one of the planes for convenience. Linear interpolation is used for fast generation of the cross-sectional plane of the image.

The straightened CPR image $M(u, v)$ is generated as follows: v is the accumulated distance from the starting point of the trace, somewhere on the centerline between $\boldsymbol{p_j}$ and $\boldsymbol{p_{j+1}}$, with distances of d_1 and d_2, the interpolated normal direction $\widehat{\boldsymbol{n}}_i = \frac{d_1}{d_1+d_2}\boldsymbol{n}_j + \frac{d_2}{d_1+d_2}\boldsymbol{n}_{j+1}$. $M(u, v = v_j)$ is the $C_i(u = \cos(\theta), v = \sin(\theta))$ derived from equation (1), where θ is the rotated view angle for the straightened CPR image.

As an example, straightened CPR views for one segment that includes the internal carotid artery and the middle cerebral artery viewed at 0, 45, 90, and 135 degrees are shown in Figure 3.14.

Trace position refinement. The 3D position of points in the trace is refined using the optimization function considering losses for trace smoothness and their intensity.

$$L_1(\boldsymbol{p}) = \sum_i L_1(\boldsymbol{p}_i)$$

$$= \sum_i \{ w_{dist} \left(||\boldsymbol{d}_i||^{(1)} + \gamma ||\boldsymbol{d}_i||^{(2)} + \gamma \left(d_{x,i}^{(2)} + d_{y,i}^{(2)} + d_{z,i}^{(2)} \right) \right) - w_{int}[I_n(\boldsymbol{p}_i) + I_s(\boldsymbol{p}_i)] \} \quad (3.23)$$

where the directional vector between two center points $\boldsymbol{d}_i = (\boldsymbol{p}_i - \boldsymbol{p}_{i-1}) = (d_{x,i}, d_{y,i}, d_{z,i})$, and $||\boldsymbol{d}_i||$ denotes the length of the vector; $I_n(\boldsymbol{p})$ and $I_s(\boldsymbol{p})$ are intensity values of normalized (M_n) and segmented (M_s) straightened CPR images at position of $\boldsymbol{p}_i = (x_i, y_i, z_i)$. (1) and (2) represent 1st and 2nd order of derivative. Minimizing the derivative of the length of the distance vector ensures the even distribution of center points along the centerline, and minimizing the derivative of the x, y, z coordinates help to ensure the smooth coordinate transitions between neighboring center points. γ is the parameter to control the first and second order weights for derivatives, and is empirically chosen as 5, the same as the active contour models [86]. Maximizing the intensities of center points on normalized and segmented straightened CPR images restricts the center points on the foreground of vascular images (lumen region of arteries). $w_{dist} = 0.02$ and $w_{int} = 1$ are weights for controlling the smoothness and intensity loss to the similar level.

Trace radius refinement. After the trace position refinement, centerline positions are fixed, and the radius of each point is refined using the following equation.

$$L_2(\boldsymbol{r}) = \sum_i L_2(u_{l,i}, u_{r,i}, v_i) = \sum_i L_2(l(v_i), r(v_i), v_i) = \sum_i w_{\text{smooth}} \left[l^{(1)}(v_i) + r^{(1)}(v_i) + \gamma l^{(2)}(v_i) + \gamma r^{(2)}(v_i) \right] - w_{\text{grad}}[M_u(l(v_i), v_i) + M_u(r(v_i), v_i)] \quad (3.24)$$

where $l(v)$ and $r(v)$ are the left and right boundary for artery radius in straightened CPR image M_n. Minimizing the derivatives controls the smoothness of both sides of boundaries. M_u is the derivative of M_n in its horizontal direction. Maximizing the horizontal gradient intensity ensures the radius boundaries to fit the edge of luminal area in the arteries. $w_{\text{smooth}} = 1$ and $w_{\text{grad}} = 50$ are weights for controlling the smoothness and gradient loss to the similar level.

Trace deviation correction. Ideally, the mean location of the left and right radius boundaries $\frac{l(u,v)+r(u,v)}{2}$ in the straightened CPR image should always be in the vertical center of the straightened CPR image ($v = v_m$). Any deviation away from the vertical center in u direction $o = \frac{l(v)+r(v)}{2} - v_m$ needs to be re-centered.

Iterative optimization from different angles. Arteries are iteratively optimized using straightened CPR images M_{deg} generated from multiple rotation angles $\{0,90,45,135\}$. The optimization process was repeated 3 times for this study. The Nelder-Mead algorithm [87] was used for optimization.

3.5.2   *Validation and Reliability*

The algorithm was then applied to the repeated artery tracings of MRA scans for 5 infants and 5 adults. As ground truth could not be determined, the measurement agreement for radii in selected arterial regions from the two repeated scans were compared before and after applying the refinement algorithm. Higher measurement agreement between repeated scans was considered to more accurately approximate the actual radius. Considering different tracing conditions, where the number of points in each segment and connection of segments in bifurcations are different, radii from selected locations on ICA, M1, M2 and M3 segments were manually chosen. One radius was selected as the sample in each segment when the segment could be matched on the second scan.

Sampled radii differences between the repeated scans, as well as intra-class correlation coefficient (ICC) and within-subject coefficient of variation (CV), were evaluated before and after the vascular refinement algorithm was applied.

3.5.3   *Experimental results*

The refinement algorithm was found to be effective at improving artery traces on 3D-TOF MRA images. In most cases, sudden changes of radius along the centerline, inaccurate radius boundary estimation due to weak MR signal, and tortuosity due to noise are minimized or resolved. One example from infants and one example from adults are shown in Figure 3.16. In this example, improvement in the delineation of arteries is visibly improved in a number of regions, including the sudden change of radius on the left side of the anterior cerebral artery and middle cerebral artery, and the right side of posterior cerebral artery, as pointed out by the red arrows.
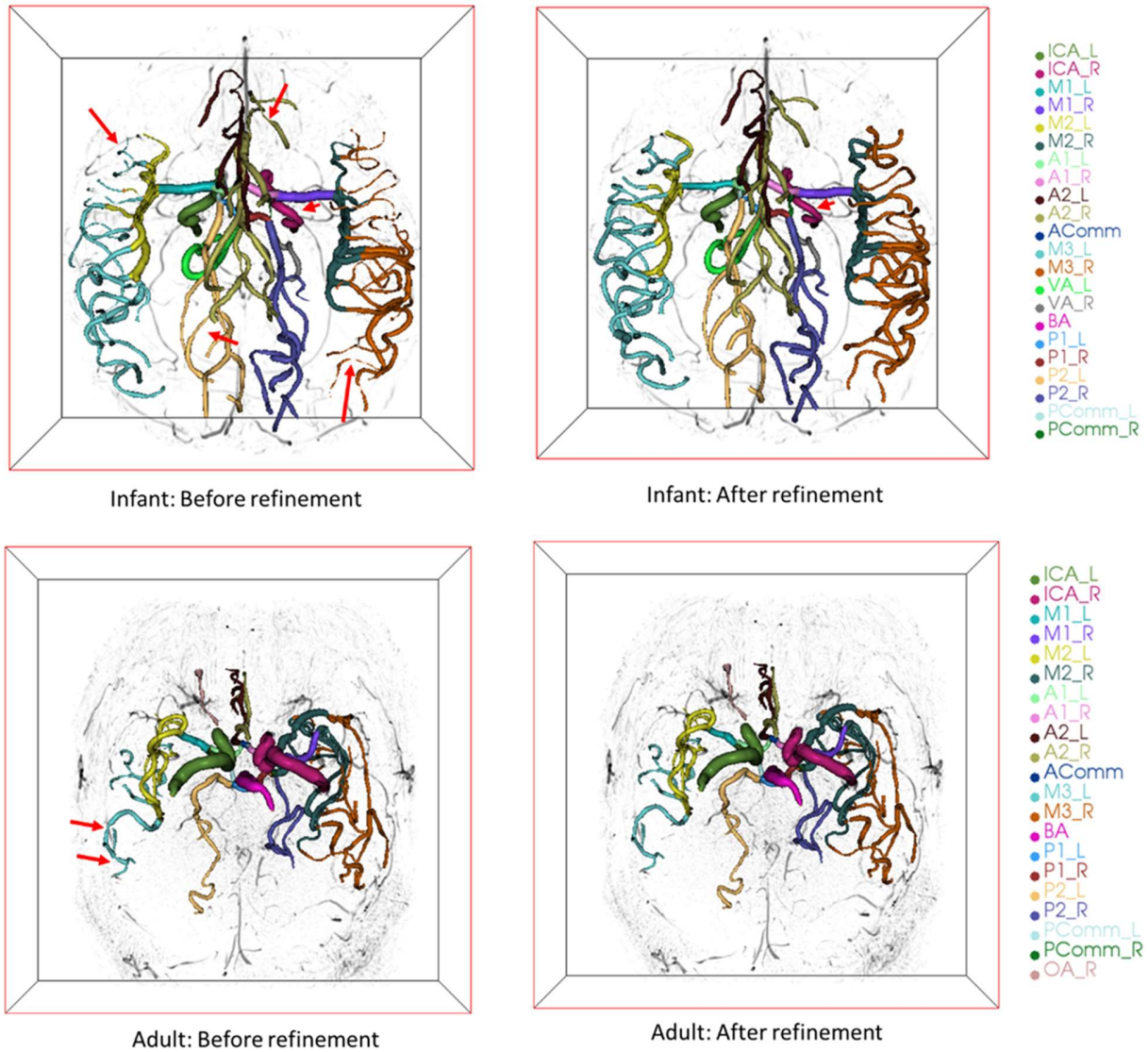
Figure 3.16 Characteristic artery traces before and after vascular measurement refinement for an infant (top row) and adult (bottom row).

Red arrows highlight several artery locations showing improvements.

Comparison of quantitative metrics of vascular features between the two scans for each subject revealed that vascular measurement refinements for TOF MRA scans improved the measurement correlations for all ten subjects. Artery radius differences measured between two repeated scans were significantly reduced using the refinement algorithm for both infants (p = 0.008) and adults (p = 0.048). ICC improved from 0.55 to 0.7 for infants, and from 0.59 to 0.92

for adults. CV decreased from 28.52% to 19.71% for infants, and from 26.65% to 11.01% for adults. Note that the adults had less motion and vascular pulsation than infants, so the artery boundary is sharper and more consistent between scans.

3.5.4 *Summary*

Limitations of imaging acquisition, as well as complications posed by specific patient populations (infants, for example), have substantially impacted the clinical reliability of the quantitative vasculature measurements. We present an artery refinement algorithm that uses straightened CPR to reduce measurement errors by incorporating both signal gradients and neighboring voxel information along the centerline.

Measurement improvements provided by this approach have the potential to allow clinically useful vascular features to be more reliably and rapidly characterized and quantified in an objective manner. This vascular measurement refinement approach will facilitate new avenues of research for vascular imaging studies to explore brain vascular changes during early development and in the presence of vascular pathology. However, this method requires iterative process, thus requiring long processing time (about 20 minutes per case). So we currently only applies this refinement algorithm on challenging cases with low image quality and severe motion artifacts (such as infant scans).

More details of this approach can be found in our publications [51], [54].

3.6   CLINICAL APPLICATIONS

3.6.1 *Validation of iCafe for quantifying artery structural features*

A series of validations are needed before *iCafe* can be used for clinical research. 1) whether the *iCafe* technique is accurate in feature quantification (point position, radius, length). 2) whether

MRA imaging is reliable for robust measurement of vasculature. 3) whether the semi-automated workflow of *iCafe* is repeatable for vascular image analysis.

iCafe is accurate in feature quantification. *iCafe* is accurate from three validations. Compared with manual labels from an experienced neuroradiologist on eight example scans, *iCafe* can generate accurate branch bifurcations, detect location of stenosis (>10% narrowing), and accurately measure artery length. The mean deviation distance of bifurcation points (N=89) is 0.328±0.444 millimeters, which is close to the image resolution of 0.297 millimeters per voxel. For the 13 stenosis locations identified by human, 11 are detected (sensitivity 11/13=85%), and two of the detected locations are not stenosis (precision of 11/13=85%). Arterial length measurements from iCafe are compared with measurements acquired from an established software, Philip Intellispace Portal Software (Philips Healthcare, Best, the Netherlands), showing an average difference between the two measures of 3.15% and intra-class correlation coefficient (ICC) of 0.97.

MRA imaging is reliable for robust measurement of vasculature and _iCafe_ is repeatable for vascular image analysis. A reproducibility study [49] is followed by the measurement validation of *iCafe* to answer the latter two questions. Twenty-four patients with known intracranial artery stenosis underwent two separate TOF MRA scans within 2 weeks of each other are processed using *iCafe* by the same operator for assessing the inter-scan reproducibility of eight representative vascular features. The first scans of eight subjects are reprocessed by the same operator for assessing the intra-operator reproducibility, and by a different operator for assessing the inter-operator reproducibility. The extracted vascular features show excellent inter-scan and intra-operator reproducibility (ICC = 0.91-1.00, and CV = 1.21-8.78% for all markers), and good to excellent inter-operator reproducibility (ICC = 0.76-0.99, and CV = 3.27-15.79% for all

markers). The good inter- and intra-operator reproducibility indicate the robustness of *iCafe* in extracting vascular features, and based on that, the excellent inter-scan reproducibility indicates the TOF MRA is reliable in imaging the artery structure and suitable for quantitative vascular feature extraction, which has not been extensively explored in the literature.

More details of this study can be found in our publications [48], [74].

3.6.2   *Vascular feature evaluation on aging population*

After validation and reproducibility assessments, *iCafe* has been extensively applied in dozens of clinical and research studies. One example is illustrated here where *iCafe* is used for cross-sectional study on vasculature for exploring healthy aging [50].

From a community study including 163 healthy subjects (age 56-85, mean 71, 74 males) from Beijing, China (the CROP study), we observe that reduced intracranial vasculature (represented as fewer number of branches and average artery order) and increased artery tortuosity are associated with healthy aging (p value <0.001 after adjustment for gender and traditional risk factors, shown in Table 3.8).

Table 3.8 Associations between age and vascular features derived from all arteries after adjustments.

Variable	Adjusted only for sex* (N=163)				Adjusted for sex and Traditional Risk Factors₃ (N=155)				Adjusted for sex and Mean Carotid Wall Thickness‡ (N=140)		
	Partial r*	(95% CI)	P-value		Partial r₃	(95% CI)	P-value		Partial r‡	(95% CI)	P-value
Total length	-0.18	(-0.31, -0.04)	0.021		-0.16	(-0.29, -0.02)	0.059		-0.17	(-0.31, -0.03)	0.047
Average diameter	0.02	(-0.13, 0.17)	0.80		0.08	(-0.08, 0.25)	0.36		0.07	(-0.10, 0.23)	0.41
Volume	-0.14	(-0.27, -0.00)	0.074		-0.08	(-0.22, 0.08)	0.35		-0.11	(-0.25, 0.04)	0.20
Number of branches	**-0.38**	**(-0.49, -0.26)**	**<0.001†**		**-0.34**	**(-0.47, -0.21)**	**<0.001†**		**-0.38**	**(-0.50, -0.25)**	**<0.001†**

Average order	**-0.39**	**(-0.50, -0.27)**	**<0.001†**		-0.35	(-0.48, -0.21)	<0.001†	-0.35	(-0.48, -0.22)	<0.001†
Average tortuosity	**0.27**	**(0.14, 0.40)**	**<0.001†**		0.16	(0.02, 0.30)	0.056	**0.28**	**(0.13, 0.41)**	**0.001†**
Average bifurcation angle	-0.08	(-0.24, 0.07)	0.28		-0.15	(-0.30, 0.00)	0.078	-0.06	(-0.23, 0.10)	0.46
Average normalized intensity	0.01	(-0.13, 0.16)	0.86		0.04	(-0.14, 0.19)	0.62	0.07	(-0.10, 0.23)	0.44

*The Partial Pearson correlation coefficient between the vascular feature and age, adjusted for sex;

‡The partial Pearson correlation coefficient between the vascular feature and age was adjusted for sex, BMI, hypertension, hyperlipidemia, diabetes, smoking history, blood pressure, LDL-C, HDL-C, and triglycerides in participants with complete clinical data;

‡The partial Pearson correlation coefficient between the vascular feature and age was adjusted for sex and mean carotid vessel wall thickness in participants with carotid wall thickness measurements;

†Statistically significant after accounting for the number of comparisons per model (Holm's method).

In addition to the global vasculature differences, with the help of 24 types of anatomical labeling of arteries, we identify the vascular changes are different on different areas of the intracranial vasculature. Only the distal branches show reduction and only the tortuosity in middle cerebral artery region (MCA) increase instead of all other cerebral regions through aging (scatter plots shown in Figure 3.17).
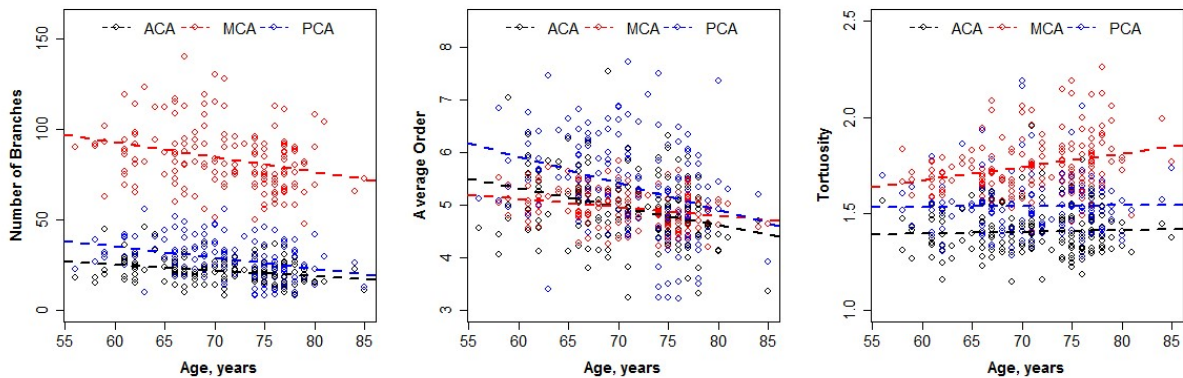
Figure 3.17 Scatterplots of selected vascular features of the ACA (black), MCA (red), and PCA territories (blue) versus age.

The least squares fits are indicated with the dashed lines. As summarized in Table 3, number of branches and average order of each territory were similarly significantly associated with age. However, tortuosity of the MCA was significantly more correlated with age than tortuosity of the other territories.

More details of this study can be found in our publication [50].

3.6.3   *Other applications*

With accurate and unique vascular features, *iCafe* has been extensively applied in dozens of clinical and research studies. The vascular features indicating intracranial structure and blood flow have been used in multiple ways. Here we have an incomplete list of our previous and on-going studies. Details of each study can be found in corresponding references if more information is needed.

- Identification of vasculature differences between dementia subjects with healthy controls [78].

- Quantitative monitoring cerebral blood flow before and after carotid revascularization surgery [85], [88].

- Validation of TOF MRA sequence reproducibility [49].

- Quantitative angiographic contrast mechanism analysis for MRA sequences [89].

- Collateral flow quantification in peripheral arteries [90].

- Exploration of medicine effect on intracranial arteries for Parkinson's disease [91].

- Exploration of the relation between vascular features and hypertensive factors in elderly males [71], [72], [92].

- Quantitative comparison of intracranial arteries of infants and elderly [54].

- Vessel length on SNAP MRA and TOF MRA is a potential imaging biomarker for brain blood flow [93].

Up to July 2021, iCafe has been requested by more than 22 academic institutes or hospitals in 6 countries for research through non-profit academic licenses. An incomplete list of their projects includes:

- Investigation of morphologic features of intracranial arteries in patients with ischemic stroke and after stroke recovery.

- Difference measurements in brain arterial structure between patients with Williams Syndrome.

- Investigation of MRA features of arterial pedicles that may predict hemorrhage risk in brain arteriovenous malformations.

- Characterization of progressive stenosis or occlusion of intracranial arteries from subjects with Moyamoya disease.

- Assessment on vascular modifications in a cohort of cerebral malaria patients from India.

- Investigate for MRA features of arterial pedicles that may predict hemorrhage risk in brain arteriovenous malformations.

- Determine the underlying mechanisms and subgroups at risk of vertebrobasilar dolioectasia.

- Use iCafe as labeling tools for intracranial artery localization and segmentation.

Chapter 4. LUMEN AND VESSEL WALL SEGMENTATION

Centerline with radius can only extract structural features of arteries. Segmentation for lumen and outer wall areas is needed after centerline generation to better delineate vascular areas, especially the accurate measurement of vessel wall area is an important indicator for atherosclerotic plaques. Vessel wall analysis in addition to the centerline generation helps us to better evaluate health status of vasculatures.

In this chapter, accurate and automated segmentation for lumen and vessel wall region was introduced for detailed geometric feature extraction of the vasculature. For bright blood MRI, only lumen area can be visualized, so a 3D patch-based CNN method (*Y-net*) was used to segment lumen areas (section 4.1) from 3D images. For black blood MRI, both lumen and vessel wall can be visualized, so a polar segmentation model was applied on cross-sectional slices along the generated centerlines (section 4.2). We have applied our vessel wall segmentation technique into the analysis of 3.5 million popliteal vessel wall images from a large knee MRI dataset and showed promising results (section 4.3).

Part of the contents from this chapter were described in details in our previous publications [53], [94]–[100].

4.1   Y-NET LUMEN SEGMENTATION FROM MRA

Lumen segmentation from MRA allows detailed artery structures to be extracted, a more detailed characterization of artery structures than the centerlines representation. Considering the complex artery intensity patterns in MRA so that no existing human-designed artery filters can segment lumen area of intracranial arteries robustly and accurately, a CNN method was used for lumen segmentation.

However, limited number of cases with segmentation labels and the large 3D image space (cannot be directly processed by usual GPUs) are the most challenges. Highly accurate manual segmentation labels as gold standard for artery segmentation are rare to find. Here we proposed to use a less perfect standard to train a model for artery luminal area segmentation by converting existing *iCafe* generated centerlines as alternative segmentation labels. To solve limited samples, a patch-based encoder-decoder CNN segmentation method with patch origin encoded (*Y-net*) was developed to fully use the similarity between different regions of artery.

4.1.1   *Y-net segmentation framework*

Patches of cubic of 16 were extracted from the 3D image, then the patch as well as the origin of the patch (normalized X,Y,Z coordinate position) were sent to the *Y-net* structure shown in Figure 4.1. Like the convolutional auto-encoder, useful image patterns were extracted from the original patch through multiple layers of convolution and max pooling for a low-dimensional encoding, then the encoded information was restored to the original size through multiple layers of convolution and up-sampling. The additional position path from *Y-net* provided patch source information as the additional information for better segmentation, as the probability of a patch containing artery in each region of the brain is different.
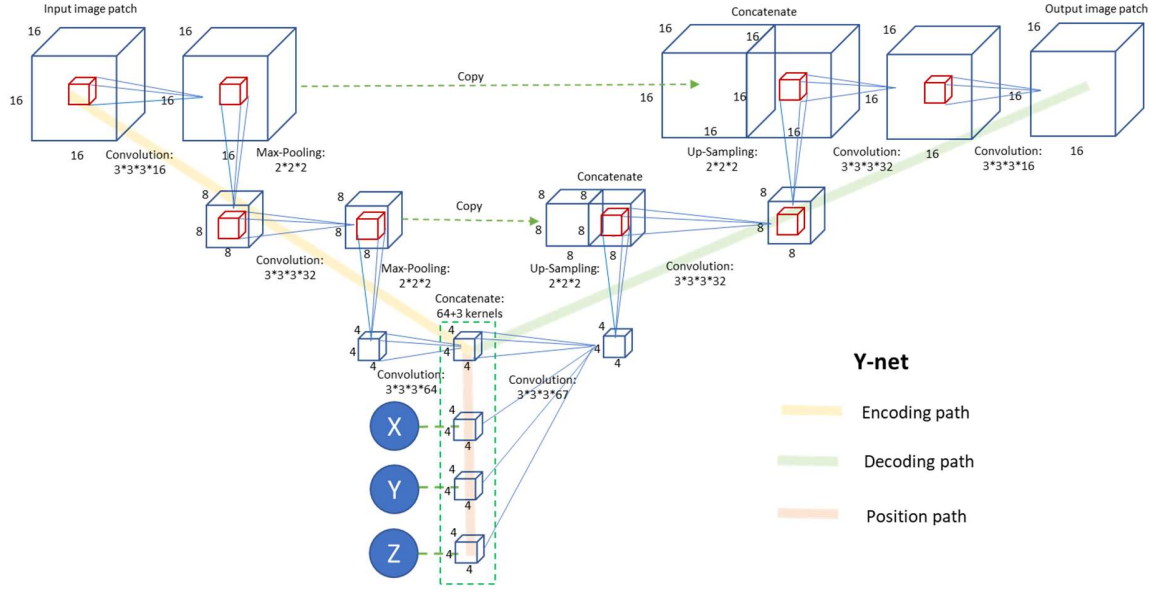
Figure 4.1 Neural network structure for *Y-net*

To build the dataset for training, 49 cases of *iCafe* traced brain TOF MRA images were used. Label image was initialized with all zeros with the same size as the original image. Centerline (with radius) is interpolated to a gap of 1 pixel per point, then a sphere is painted with intensity of 1 in the label image at each point center. Then patches from original image and labeled image are extracted using a sliding window to train the network. To balance the patches with and without artery region (around 99% voxels are background), strides for sliding window are different in a two-stage extraction strategy. Firstly a smaller stride S_1 extracts P_p positive patches if there is at least one voxel labeled as vascular region in labeled patches from P_a patches; then a larger stride S_2 is estimated according to the selection rate in the previous step to extract similar number of all non-artery patches.

$$S_2 = \sqrt[3]{\frac{P_a - P_p}{P_p}} \tag{4.1}$$

When the network was trained, predictions from overlapped patches (with stride of 8) were averaged to ensure smoothness in patch boundaries, then a threshold was selected from the validation set to get the best binary segmentation.

4.1.2   *Evaluation metrics*

The post-processed binary image was compared with the labeled image voxel by voxel. Binary classification performance was evaluated by accuracy, sensitivity, specificity, precision, and the dice similarity co-efficient (DSC), defined as

$$DSC = \frac{2(A \cap B)}{(A+B)} \tag{4.2}$$

where A is the ground truth result and B is the segmentation result. DSC ranges from 0 (no overlap) to 1 (identical results). DSC > 0.7 indicates excellent agreement [101].

4.1.3   *Experimental results*

The binary classification results from CAE (with variations) as well as traditional segmentation methods are shown in Table 4.1.

Table 4.1 Binary classification evaluation between Y-net (with threshold) and classical segmentation methods

Models	Accuracy	Sensitivity	Specificity	Precision	DSC
Y-net (0.38)	0.99837	0.83815	0.99913	0.81883	0.82838
Y-net (0.15)	0.99726	0.92235	0.99761	0.64560	0.75955
Y-net (0.38) no localization	0.99823	0.82208	0.99906	0.80465	0.81327
Y-net (0.38) epoch 100	0.99801	0.80282	0.99893	0.77965	0.79107
Renyi	0.99500	0.52331	0.99724	0.47272	0.49673
Phansalkar	0.85897	0.92017	0.85868	0.02992	0.05795
Frangi	0.99731	0.56023	0.99937	0.80856	0.66187

A threshold of 0.38 was selected. The generated MIP views of the labeled image, predicted image by CAE, and segmentation results using traditional methods of the test set are shown in Figure 4.2.
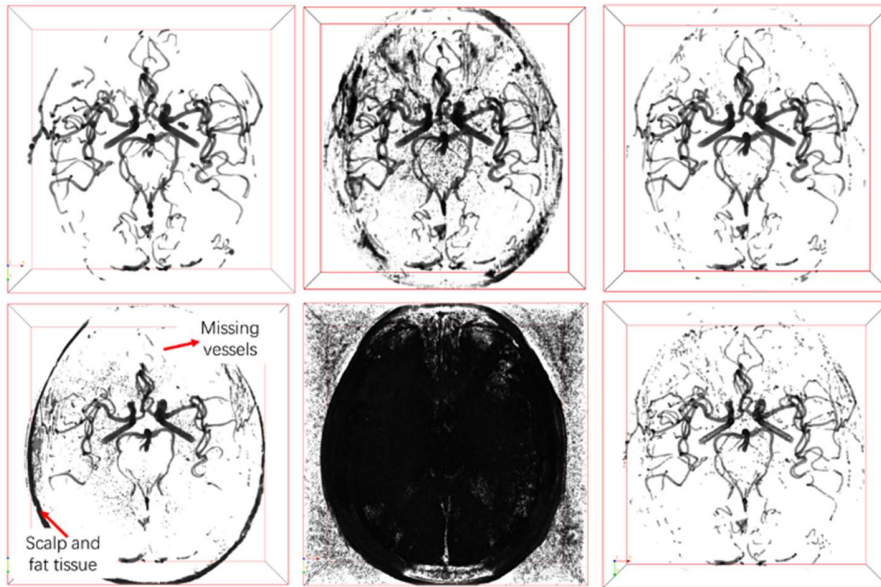
Figure 4.2 An example of lumen segmentation.
Top Left: Labeled image. Top middle: Predicted image (with possibility from 0 to 1) by CAE. Top Right: Predicted image after thresholding. Bottom Left to Right: Segmentation results by Renyi Entropy threshold, Phansalkar local threshold, and Frangi filtering.

4.1.4 *Summary*

We trained a *Y-net* for intracranial artery segmentation on brain TOF MRA. Our model outperformed three traditional segmentation methods in both binary classification and visual evaluation. Accurate segmentation of the whole cerebral vasculature will facilitate quantification of global and territorial vascular features.

More details of this approach can be found in our publications [94], [102].

4.2   POLAR VESSEL WALL SEGMENTATION FROM VWI

Compared with lumen segmentation from MRA, where the signal contrasts in lumen boundaries are much higher, vessel wall segmentation from VWI is more challenging. Both lumen boundary and outer wall boundary can be identified in the black blood VWI, but the segmentation target of the vessel wall area is much smaller than the lumen area. If we directly use the network structure in lumen segmentation on vessel wall [95], although most slices with normal vessel wall can be segmented reasonably well, some challenging slices with weak signal or irregular vessel wall boundaries are problematic. The segmented vessel wall region does not always have closed contours, which are not possible to extract vessel wall morphometry features as the critical measurements for atherosclerotic plaques. In addition, neighboring arteries (for example, ECA near ICA) will also be segmented due to the similar vessel wall signal patterns. One example is shown in Figure 4.3.
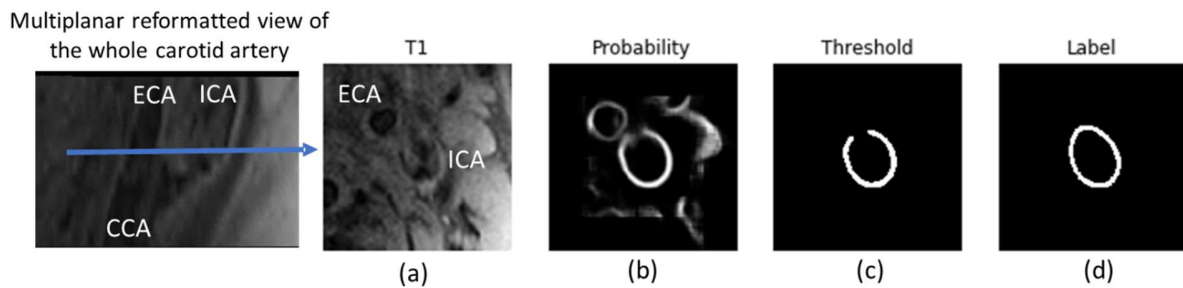
Figure 4.3 Exemplar problems encountered previously in the Cartesian based CNN method [94].

(a) Original vessel wall image

(b) Probability map from prediction. ECA is visible in the region of interest for ICA (the target artery) vessel wall segmentation, leading to both arteries with high probability.

(c) Broken vessel wall segmentation due to weak signal on vessel wall region.

(d) The human label.

In addition, feedback from the automated segmentation model, for example, the confidence of the segmentation is usually not available, but might be useful for clinicians to manually correct contours on the problematic slices to ensure the segmentation quality.

In this section, vessel wall segmentation in the polar coordinate system is explored and compared with the state-of-the-art Cartesian segmentation methods. Different from almost all other methods based on the Cartesian coordinate system, the vessel wall segmentation in the polar coordinate system provides unique benefits including better vessel wall continuity and improved segmentation especially needed in challenging slices near arterial bifurcations, where the artery shape is no longer circular. In addition, by predicting boundary coordinates from rotated polar patches and comparing with the probability map, our method can additionally yield uncertainty scores to inform human for possible mistakes. An illustration of polar segmentation workflow is shown in Figure 4.4.
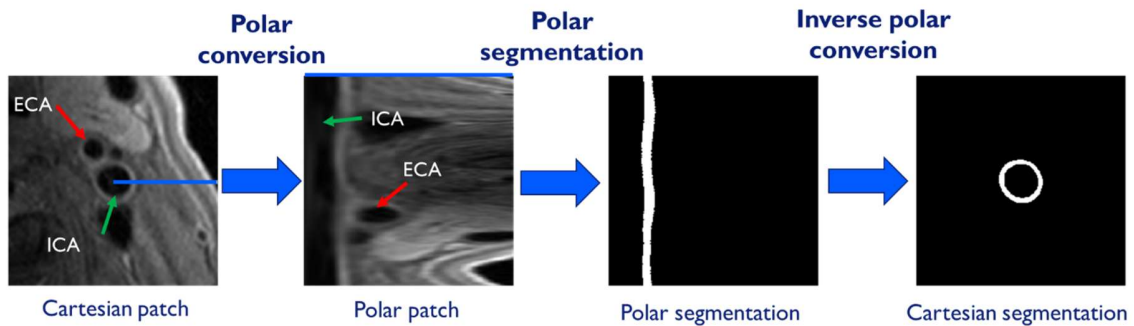
Figure 4.4 Workflow for Polar segmentation on vessel wall.

First, image patch along the ICA/CCA centerline is extracted (ECA centerline can be generated if needed), then the Cartesian image patch is converted into the polar coordinate system so that similar artery structures (ICA and ECA) will be much different in the polar patch. After segmentation for polar patches in the polar coordinate system, which is easier to ensure boundary continuity, the image is converted to Cartesian coordinate system through inverse polar conversion.

4.2.1   *Polar segmentation network*

The Cartesian image patch $\hat{P}[y, x]$, with the size of $4h * 4w$ (h: height and w: width, 4 times the original scale to enlarge the vessel wall images; height and width are large enough to ensure the whole vessel wall can be included in the image patch) is extracted from the original 3D image at the position along the generated ICA/CCA centerline using the centerline generation method introduced in the section 3.1. Then $\hat{P}[y, x]$ is converted to the polar image patch $P[t, r]$ (t: translation, r: rotation) using the polar transformation. ECA centerline can also be generated for vessel wall segmentation using similar methods if needed.

$$\begin{cases} r = \sqrt{(y - 2*h)^2 + (x - 2*w)^2} \\ t = \begin{cases} \begin{cases} \frac{h}{180}\arctan\left(\frac{y-2*h}{x-2*w}\right), y > 2*h \text{ and } x > 2*w \\ \frac{h}{180}\arctan\left(\frac{y-2*h}{x-2*w}\right) + 180, y < 2*h \\ \frac{h}{180}\arctan\left(\frac{y-2*h}{x-2*w}\right) + 360, y > 2*h \text{ and } x < 2*w \\ 90, x = 2*w \text{ and } y = 2*h + r \\ 270, x = 2*w \text{ and } y = 2*h - r \end{cases} \end{cases} \end{cases} \tag{4.3}$$

We designed four CNN architectures for segmentation in the polar coordinate system and compared their performances.
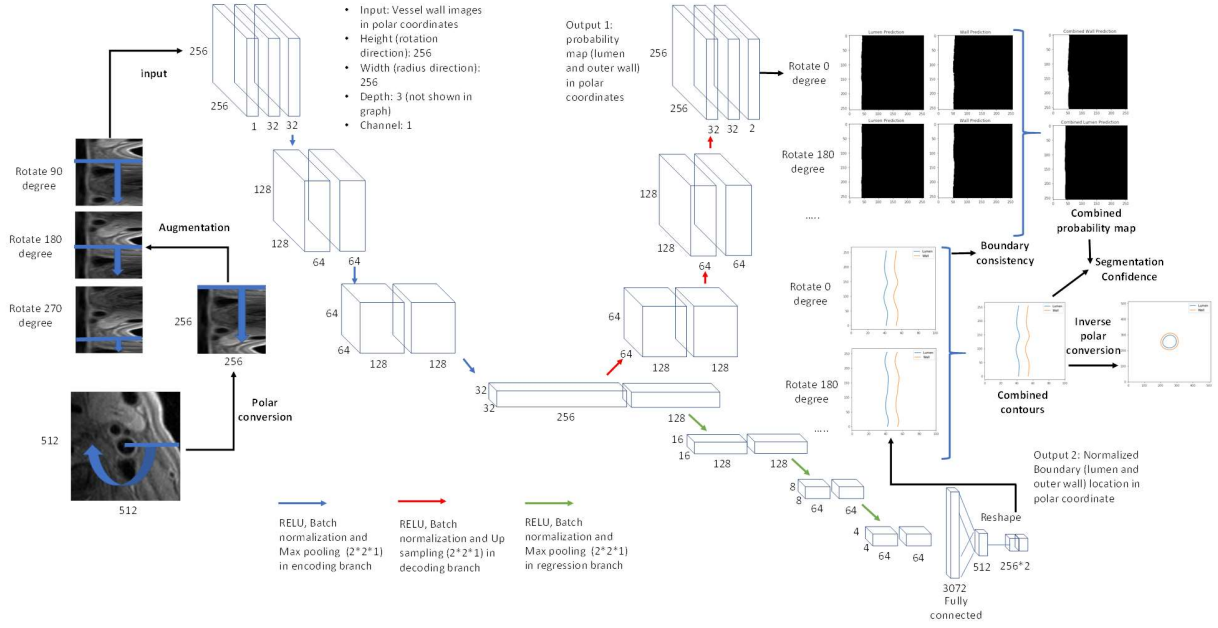
Figure 4.5 Workflow for proposed polar segmentation CNN architectures.

The first structure (Polar-Seg-Reg) with three CNN branches is shown in Figure 4.5. The encoding branch extracts the useful information from the polar patch for the decoding branch to predict segmentation probability map $S(P)$ and for the regression branch to predict the lumen and outer wall boundary coordinates in the polar coordinate system $R_l(P), R_w(P)$. The boundary coordinates then are converted to Cartesian system $\hat{R}_{l,w}(y,x) = f^{-1}(R_{l,w}(P))$. The inverse polar conversion is defined as $\hat{P}[y,x] = f^{-1}(P[t,r])$, where

$$\begin{cases} y = 2*h + r*\sin\left(t*\frac{360}{2*h}\right) \\ x = 2*w + r*\cos\left(t*\frac{360}{2*h}\right) \end{cases} \tag{4.4}$$

The regions between boundaries $\hat{R}_{l,w}(y,x)$ are filled with 1 to be the binary segmentation mask $\widehat{SM}_r(P)$. No skip connections [58] between the encoding and decoding branches are used to ensure the most representative information is encoded in the shared middle layer to better train the

boundary regression branch. Dice loss [103] and mean absolute error loss are used for the decoding and regression branch. Adam optimizer [84] is used to control the learning rate.

The second architecture (Polar-Seg) only has the encoding and decoding branches but no regression branch. The segmentation mask is generated from the segmentation probability map $S(P)$ in the polar coordinate system using the active contour algorithm [86] then converted to the Cartesian coordinate system. To apply the prior knowledge of the smooth ring shape of vessel wall, an extended map is used to avoid sudden change in boundaries between two edges of the polar image ($P[t = 0, r]$ and $P[t = 2 * h, r]$).

$$S'(P[t, r], b) = \begin{cases} S(P[2 * h - b + t, r]), t < b \\ S(P[t, r]), b \le t \le b + 2 * h \\ S(P[t - b - 2 * h], r), t > b + 2 * h \end{cases} \quad (4.5)$$

With the added paddings, bilateral neighboring information is available to predict smooth contours for regions near two edges. $b = 40$ is used in this study. Initial contours are found at minimum and maximum gradient image along the r direction.

$$\begin{cases} R_l{}^0(P[t, r]) = argmax_r(S'(P)[t, r] - S'(P)[t, r - 1]) \\ R_w{}^0(P[t, r]) = argmin_r(S'(P)[t, r] - S'(P)[t, r - 1]) \end{cases} \quad (4.6)$$

Head and tail of contours $R_{l,w}(P[t = 0 \ and \ 2 * h + 2 * b])$ are fixed during the iteration of the active contour algorithm. After iterations, the regions between contours $R_{l,w}(P[b \le t \le 2 * h + b])$ are filled with 1 to be the segmentation mask $SM_s(P)$.

The third architecture (Polar-Reg) only has the encoding and regression branches but no segmentation branch. The configuration and segmentation method are the same as the first architecture except the removal of the segmentation probability map.

In addition to the three polar segmentation CNN architectures introduced in Figure 4.5. As an extension of the Polar-Reg model, a deeper regression model with Resnet 101 [104] is compared

on the performance improvement with deeper CNN architecture. The model (Polar-Res-Reg) is adapted by connecting last two layers of Polar-Reg to the last fully connected layer from Resnet trained with initial weights on ImageNet dataset [105].

To incorporate neighboring slices information, patch slices extracted from $\hat{I}$ at neighboring slices were concatenated in the depth dimension in all CNN architectures. For simplicity, the depth channel is not drawn in Figure 4.5.

Data augmentation is needed for better training with limited samples. Traditional augmentation methods such as rotation and offsetting are not suitable for polar patches. A polar patch rotation method is proposed instead. Considering the boundless property of polar patch along the angle directions, augmented polar patch is defined as

$$P'_\alpha[t,r] = \begin{cases} P[2*h - \alpha + t, r], t < \alpha \\ P[t - \alpha, r], t \geq \alpha \end{cases} \tag{4.7}$$

where α is a random integer from 0 to $2*h$. Combined with vertical flipping, $4*h$ times samples can be acquired for training.

During the prediction stage, multiple rotated polar patches are combined to ensure the boundary smoothness. Rotated patches with $\alpha_i = i*G, i = 1,2,\ldots,\lfloor 2*h/G \rfloor$ are generated and their prediction results are averaged to be the final probability map and boundary coordinates. G is the predefined gap for predictions (10 is empirically selected in this study).

Final probability map of the patch M from the segmentation branch can be calculated as

$$M[t,r] = S(P[t,r]) = \frac{1}{2*\frac{h}{G}} \sum_i S(P'_{\alpha_i})[g(t - \alpha_i), r] \tag{4.8}$$

where $g(x) = \begin{cases} x + 2*h, x < 0 \\ x, x \geq 0 \end{cases}$.

Final lumen and outer wall boundary coordinates of the patch from the regression branch B_l and B_w can be calculated as

$$B_{l,w}[t] = R_{l,w}(P[t]) = \frac{1}{2*h/G}\sum_i R_{l,w}(P'_{\alpha_i}[g(t - \alpha_i)]). \tag{4.9}$$

Vessel wall contours in Cartesian coordinate system are

$$\hat{B}_{l,w}(x,y) = f^{-1}\left(B_{l,w}(t)\right). \tag{4.10}$$

4.2.2   *Segmentation uncertainty scores*

We observe that vessel wall segmentation with good agreement with manual labels demonstrates clear boundaries and a simple ring shape in MR images, and thus the segmentation neural network reliably generates consistent vessel wall boundaries from rotated patches with any α_i, in other words, $S(P'_{\alpha_i})[g(t - \alpha_i), r]$ and $R_{l,w}(P'_{\alpha_i}[g(t - \alpha_i)])$ should be constants with all possible α_i. In addition, the output results from the segmentation and the regression branches should be consistent, in other words, $|f^{-1}(M) - \widehat{SM}_r(P)| = 0$.

Based on that, we propose two methods to quantify the segmentation uncertainties by up to three scores from the CNN architecture.

For the first architecture where both the segmentation mask $M[t,r]$ from the segmentation branch and the boundary coordinates $B_{l,w}[t]$ from the regression branch are available, segmentation confidence $Conf(P)$ can be calculated from the consistency between two branches, defined as the normalized foreground minus background probability map.

$$FS = \sum_{t,r} M[t,r], if\, B_l[t] \leq r \leq B_w[t]\,, \tag{4.11}$$

$$BS = \sum_{t,r} M[t,r], if\, r < B_l[t]\, or\, r > B_w[t], \tag{4.12}$$

$$Conf(P) = \frac{FS-BS}{\sum_t (B_w[t]-B_l[t])}, \tag{4.13}$$

$Conf(P)$ has the maximum value of 1, indicating perfect confidence, but has no lower limit.

For the first and third architectures where the boundary coordinates $R_{l,w}(P[t])$ from the multiple rotated patches are available, the lumen and wall consistency can be calculated as

$$Cst_{l,w}(P) = 1 - \frac{1}{2*h}\sum_t\left(\frac{1}{\sqrt{\frac{1}{12}}}\sqrt{\frac{1}{2*\frac{h}{G}}\sum_\alpha\left(\frac{R_{l,w}(P'_\alpha[t])-B_{l,w}[t]}{2*w}\right)^2}\right). \quad (4.14)$$

Boundary coordinates are normalized between 0 to 1, and the variation of prediction from different patches is evaluated by the ratio of standard deviation of boundaries predicted from different patches to the worst case when all the predictions are random ($\sqrt{1/12}$). Range of consistency is between 0 (random) to 1 (perfect consistent). The worst case scenario is unlikely to happen, which means the score is usually high.

Polar patches used for training were converted from perfect lumen centers, which was not the case for testing data, leading to inferior segmentations in prediction. Even refined after artery centerline generation, the artery centers can still be further improved from the deviations calculated from the predicted polar boundaries. The center deviations can be reduced iteratively from the angle of $\frac{360°}{2h}\emptyset$ with the largest differences of polar coordinates from opposite directions.

$$\begin{cases} \emptyset = argmax(|B_l[\emptyset] - B_l[\emptyset + h]|) \\ \Delta x = \cos(B_l[\emptyset] - B_l[\emptyset + h]) \\ \Delta y = \sin(B_l[\emptyset] - B_l[\emptyset + h]) \end{cases} \quad (4.15)$$

4.2.3   *Evaluations*

We used the same carotid dataset introduced in section 3.1 for evaluating the segmentation performance. Lumen and outer walls are traced manually by trained reviewers with 3+ years' experience in cardiovascular MR imaging using a custom-designed software package (CASCADE) [64]. Image slices with poor image quality are excluded from review and all the labeled slices are also peer reviewed to ensure the label quality.

To evaluate the effect of accurate polar centers on the performance of vessel wall segmentation, the Polar-Reg model was tested directly on bounding box centers (without tracklet

refinement). To evaluate the effectiveness of the iterative center adjustment from segmentation, Polar-Reg-Once allowed only one segmentation per vessel wall.

Cartesian based segmentation methods (existing methods are usually in this category) were also compared, including the popular neural network models 3D U-net [58] (previously adopted in vessel wall segmentation [95]), Mask-RCNN [106] (Resnet 101 backbone, pretrained on the ImageNet [105] dataset). These methods were trained and tested using the same datasets and settings as our polar models.

We also compared the performance with a state-of-the-art non-CNN vessel wall segmentation method, Optimal front segmentation (Opfront) [41], which is based on the graph cut algorithm.

Performance of the segmentation was evaluated by the DSC, and Degree of Similarity (DoS) [107], both of which ranged from 0 (mismatch) to 1 (perfect match). DSC > 0.7 indicates excellent agreement [108]. DSC for lumen (DSC^{Inner}: area within the lumen contour), complete vessel (DSC^{Outer}: area within the outer wall contour) and vessel wall (DSC^{VW}: area between the lumen and outer wall contours) were evaluated separately. DoS for lumen and outer walls were also evaluated separately as DoS^{Lumen}, DoS^{Wall}. In addition, vascular features from predicted and ground truth contours were calculated and compared. Representative and clinically important vascular features were selected, including max wall thickness, mean wall thickness, lumen area, and wall area. Absolute mean difference and intraclass correlation coefficient between predicted and ground truth vascular features were calculated.

Independent associations between consistency scores and DSC^{VW} were evaluated using Spearman's partial rank correlation coefficients. The correlation between a combination of scores and DSC^{VW} was summarized using R-squared from a linear model with rank-transformed scores as predictor variables and DSC^{VW} as the outcome variable. These analyses were conducted at the

slice level, so generalized estimating equations (GEEs) were used to test associations and compare models while accounting for non-independence between slices from the same subject.

4.2.4   *Experimental results*

The superior performance of polar models compared with other models in vessel wall segmentation and vessel wall feature quantification is shown in Table 4.2 and Table 4.3.

Table 4.2 Carotid vessel wall segmentation performance compared with other methods.

Model	DSC VW	DSC[I] NNER	DSC Outer	DoS[L] umen	DoS Wall	Number of failed slices	Processing time (s)	Number of parameters in network
Polar-Res-Reg	**0.860**	**0.961**	**0.962**	**0.921**	**0.864**	**0**	0.757±0.072	44,989,224
Polar-Res-Reg-Single	0.841	0.955	0.954	0.901	0.838	**0**	0.891±0.151	44,989,224
Polar-Reg	0.852	0.958	0.959	0.913	0.846	**0**	0.738±0.058	5,642,016
Polar-Seg-Reg	0.852	0.958	0.959	0.912	0.840	**0**	1.264±0.066	7,386,914
Polar-Seg	0.811	0.942	0.945	0.866	0.747	**0**	0.886±0.059	4,095,682
Mask R-CNN [109]	0.792	0.940	0.940	0.654	0.565	81	0.138±0.027	63,733,406
Cartesian U-net [110]	0.774	0.922	0.941	0.647	0.517	194	**0.103±0.032**	4,094,817
Opfront [41]	0.531	0.822	0.878	N/A	N/A	N/A	38.717±5.370	N/A

Table 4.3 Carotid vessel wall features quantified from segmentation compared with other methods.

Model	Max Wall Thickness		Mean Wall Thickness		Lumen Area		Wall Area	
	MAD	ICC (CI)	MAD	ICC (CI)	MAD	ICC (CI)	MAD	ICC (CI)
Polar-Res-Reg	**0.890**	**0.896 (0.887-0.904)**	**0.484**	**0.886 (0.878-0.893)**	**25.715**	**0.985 (0.984-0.986)**	**40.404**	**0.984 (0.983-0.985)**
Polar-Reg	0.956	0.874 (0.864-0.883)	0.511	0.870 (0.862-0.878)	27.715	0.981 (0.979-0.982)	43.317	0.981 (0.979-0.983)

Polar-Reg-Seg	0.916	0.893 (0.886-0.900)	0.507	0.879 (0.871-0.887)	27.221	0.983 (0.982-0.984)	43.625	0.983 (0.982-0.984)
Polar-Seg	1.353	0.760 (0.717-0.794)	0.692	0.762 (0.644-0.832)	31.338	0.965 (0.963-0.968)	59.100	0.971 (0.961-0.978)
Mask R-CNN [106]	1.264	0.653 (0.632-0.672)	0.701	0.509 (0.473-0.543)	32.171	0.942 (0.938-0.945)	62.567	0.907 (0.885-0.924)
Cartesian U-Net [58]	1.071	0.810 (0.798-0.822)	0.565	0.808 (0.728-0.859)	45.065	0.935 (0.923-0.945)	52.460	0.949 (0.945-0.952)

As an example, the segmentation results by methods on two image slices are shown in Figure 4.6. In general, polar models have good to excellent evaluation metrics (DSC > 0.7 indicates excellent agreement [108], ICC>0.75 is considered good, and >0.9 indicates excellent [111]). Polar regression models (Polar-Reg, Polar-Reg-Seg) have better performance than the segmentation model (Polar-Seg), in both lumen and outer wall, indicating segmentation from predicting boundaries are more effective than predicting probability maps. Deeper regression network (Polar-Res-Reg with 45.0M parameters) has slightly better performance than the shallower regression model (Polar-Reg model with 4.6M parameters). Network architecture with neighboring slices as inputs are better than single slice inputs. The traditional method (Opfront) cannot handle vessel wall with weak signals, and in most cases cannot ensure ring shapes, so DoS is not evaluated.
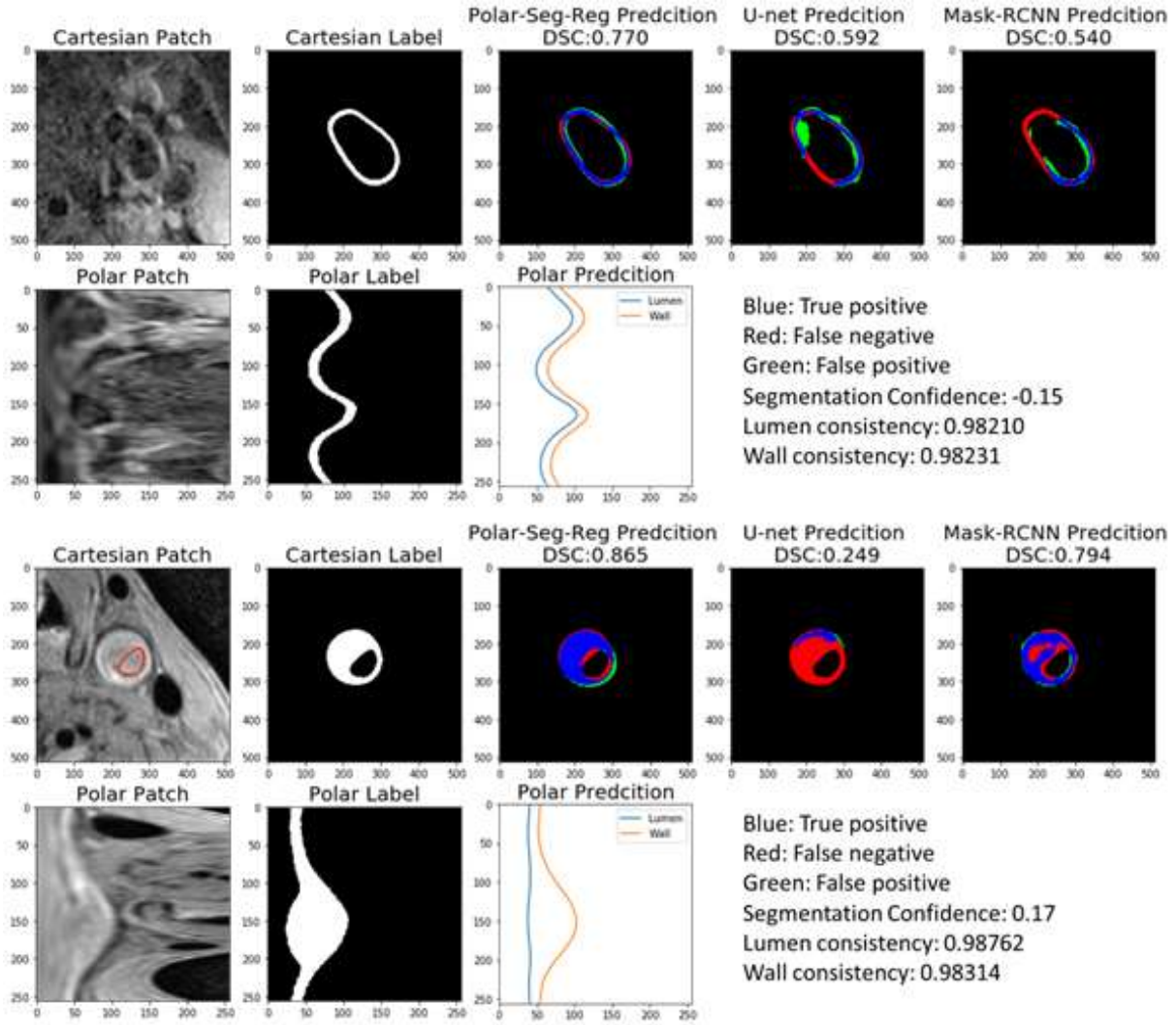
Figure 4.6 Examples of vessel wall segmentations at the slices distal (first two rows) and proximal (bottom two rows) to the carotid bifurcation.

Original Cartesian patches are converted to polar patches (first column) for prediction of vessel wall contours in polar coordinate system (middle bottom plot). Coordinates are converted back in Cartesian system and the region between two contours are filled as the segmentation (middle top plot). To better display the segmentation difference with manual labels (second column), regions are displayed as blue (TP, correct segmentation region), green (FP, wrong segmented region), and red (FN, not segmented region). Segmentation from two Cartesian methods (U-Net [58] and Mask R-CNN [106]) are compared in last two columns. Cartesian segmentations might have wrong artery of interest segmented (top) or broken vessel wall (bottom). For patches with low contrast (bottom), the uncertainty scores from the polar model

(Polar-Seg-Reg used as an example) are low, indicating possible lower segmentation performance, so manual checking might be required. A red line is drawn on the original patch to show lumen boundary.

The number of slices and the mean DSC-VW in each of the image quality levels are shown in Table 4.4. Better image quality led to higher DSC-VW, but even for slices with only adequate image quality, the polar regression models still generated contours with DSC-VW over 0.694.

Table 4.4 DSC^{VW} from slices with different image qualities of carotid arteries

	Image quality		
	Adequate	Good	Excellent
Number of slices	621	2483	302
Polar-Reg with ground truth center	0.802	0.861	0.880
Polar -Reg with localized center	0.694	0.778	0.809

Lastly, the uncertainty of segmentation is quantified using three scores. Both segmentation confidence and lumen consistency show significant contribution (p<1.26e-4 for all polar models) in predicting DSC^{VW}, indicating lower scores are likely to generate a poor segmentation mask compared with the ground truth. Wall consistency has strong relations with lumen consistency, so its partial correlation is lower in the regression model. Quantitative results between models are shown in Table 4.5. Two of the segmentation uncertainty scores (segmentation confidence and lumen consistency) are shown to provide independent and critical information in identifying problematic slices in segmentation.

Table 4.5 Quantitative comparison of carotid segmentation uncertainty predicted by polar models.

Polar models	Segmentation Confidence	Lumen Consistency	Wall Consistency	R square

	Correlation	P value	Correlation	P value	Correlation	P value	
Polar-Res-Reg	N/A		0.244	<1e-5	-0.043	0.060	0.139
Polar-Reg	N/A		0.132	<1e-5	0.047	0.045	0.115
Polar-Seg-Reg	0.161	<1e-5	0.086	1.26e-4	-0.007	0.769	0.141
Polar-Seg	0.552	<1e-5	N/A				0.305

Correlation: partial correlation coefficient from Spearman's method. P value: from Generalized Estimating Equations. R square: from a linear model with rank-transformed scores as predictor variables and DSC^{VW} as the outcome variable

4.2.5   *Extensible to other vascular beds*

The polar segmentation can also be applied to vascular beds other than the carotid arteries which were fully validated in section 4.2.4. Following a similar centerline generation, patch extraction along centerlines and polar segmentation workflow, vessel wall morphometry features from VWI of popliteal arteries and intracranial arteries can also be quantified. Details for the vessel wall analysis on popliteal arteries will be discussed in section 4.3. An example of intracranial artery vessel wall segmentation result is shown in Figure 4.7.
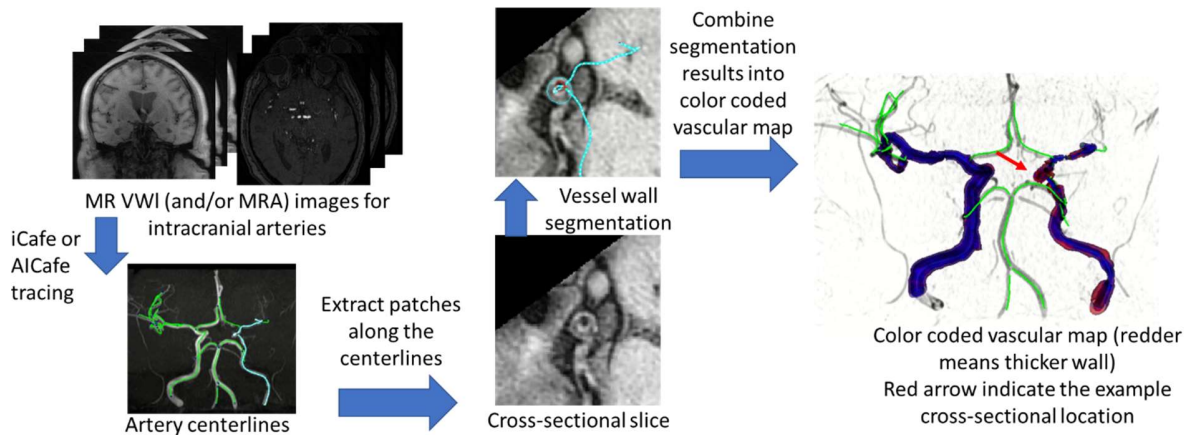
Figure 4.7 Color coded intracranial arteries to display vessel wall thickness along the centerlines. The redder, the thicker of intracranial vessel wall.

4.2.6   *Summary*

Fully automated vessel wall segmentation was achieved with high accuracy by effectively using a CNN based regression model to segment vessel wall in the polar coordinate system. Traditional vessel wall segmentation methods are susceptible to poor image quality, only providing reasonable results when both lumen and outer wall boundaries have high contrast. Our proposed deep learning-based method extracted useful boundary information from more than 32,000 slices of manually drawn vessel wall contours with various levels of image quality. We believe our dataset encompasses a wide spectrum of atherosclerosis as well as healthy arteries and is capable of training a robust deep learning model with good generalizability. The use of the polar regression CNN architecture is an ideal approach, incorporating the prior knowledge of vessel wall structures (e.g., ring shape, lumen in the center), and outperforms our previous deep learning segmentation method [95] based on the Cartesian coordinate system.

Both consistency scores were shown to provide independent and critical information in identifying problematic slices in segmentation, which can be useful in guiding humans to examine only the slices with higher likelihoods of possible errors and ensure high segmentation quality.

The application of deep learning methods in vessel wall segmentation might have a profound impact on MR vessel wall image analysis. As a research tool, with accurately segmented vessel wall areas from an automated method, quantitative vessel wall features can be extracted to enhance our understanding of atherosclerosis progression from large population studies, for which time-consuming manual or semi-automated methods are not achievable (details in section 4.3). Clinically, a fast screening tool can be developed to automatically identify high-risk patients for further detailed examination in a time-efficient manner (details in chapter 5). After choosing a proper threshold for better sensitivity over specificity, the quantitative vessel wall features along

with the confidence scores can largely reduce the burden for clinicians by prioritizing patients urgently requiring medical care and giving initial evaluations for the carotid scans.

More details of this approach can be found in our publications [53], [96].

4.3 CLINICAL APPLICATIONS

4.3.1 *Development of FRAPPE*

Our fully automated vessel wall segmentation method makes the analysis of large population studies available. The Osteoarthritis Initiative (OAI) [112] dataset, sponsored by the National Institutes of Health, (available for public access at http://www.oai.ucsf.edu/) is an ideal dataset which best suits our purpose. This massive dataset (bilateral knee MRI in 4796 subjects up to 8 time points over a period of 96 months, over three million images in total) provides high-quality 3D VW MRI images with the popliteal artery wall clearly visible on the 3D DESS sequence. Therefore, it is ideal for research on vessel wall features as MR biomarkers [113] and the relationship of these biomarkers with cardiovascular risks [92].

By adapting the artery centerline generation and vessel wall segmentation techniques to popliteal arteries, we developed a **f**ully automated and **r**obust **a**nalysis technique for **pop**liteal artery **e**valuation (*FRAPPE*) specifically optimized for popliteal vessel wall analysis.

Workflow of *FRAPPE* along with example images in each step is shown in Figure 4.8.
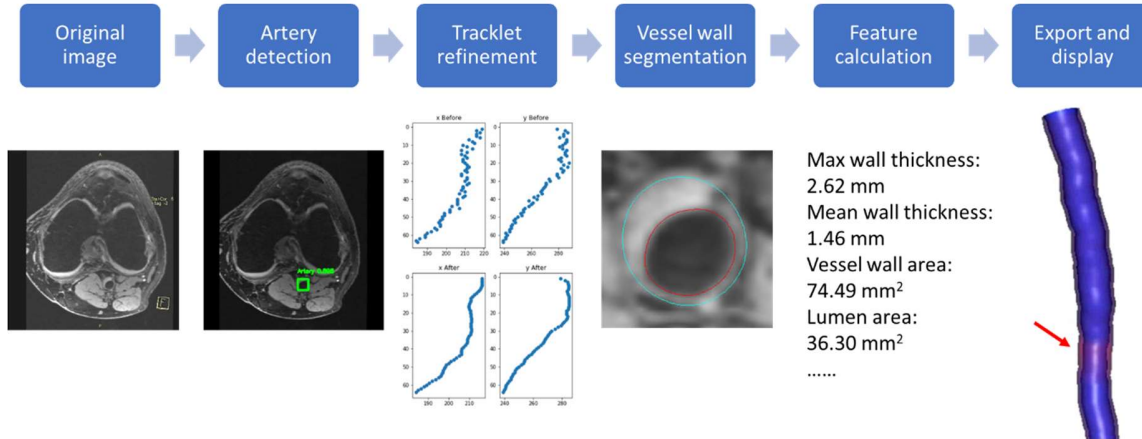
Figure 4.8 Workflow of FRAPPE and example images from each step.

Transfer learning and active learning techniques were applied to train the centerline generation and segmentation models, aided by limited human annotations. Initiated from previous models for carotid artery applications [96] where many human annotations are available, models could be trained using a relatively small dataset of popliteal artery images to reduce the need for tedious human labeling.

From the segmentation model developed from the carotid dataset, additional 23 subjects (1264 slices of vessel wall contours) were used to further tune the model on popliteal arteries. The validation and test sets include 2 subjects (117 slices) and 10 subjects (588 slices), respectively.

To improve the robustness of *FRAPPE* in quantifying the images which are particularly challenging, such as abnormal artery structures, poor image quality or with substantial artifacts, an active learning process with manual supervision was applied. With manual corrections on vessel wall contours from an expert human reviewer (with over 10 years of experience in vascular review), batches of challenging samples, such as images in artery bifurcations or with calcified plaques, with low confidence scores, are chosen for manual corrections, then the corrected images were used for further training, so that the performance of *FRAPPE* on difficult samples was

iteratively improved. One slice of image with calcified plaque before and after active learning is shown in Figure 4.9.

Original image with calcified plaque (red arrow)   Segmentation results before active learning   Segmentation results after active learning
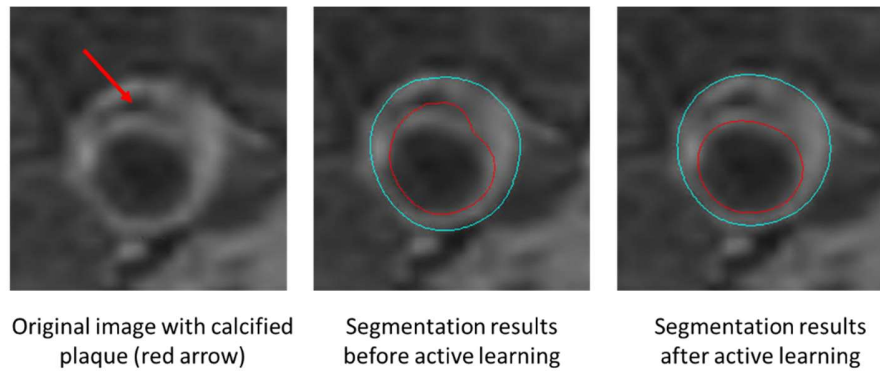
Figure 4.9 Calcified plaque (left image pointed by the red arrow) missed before active learning (middle), found after additional training using active learning technique (right)

From the test set, *FRAPPE* has the DSC of 0.79 (95% CI: 0.77-0.81). Relative to human reviewers, the CV and ICC estimates for *FRAPPE* were 8.7% and 0.73 for mean wall thickness, 10.0% and 0.90 for mean wall area, and 2.9% and 0.99 for mean lumen area. Some of the segmentation results on challenging images are shown in Figure 4.10, demonstrating good performance of *FRAPPE* on bifurcation images, vessel wall with low contrasts, vessel wall with plaque, and when the artery is close to the vein.
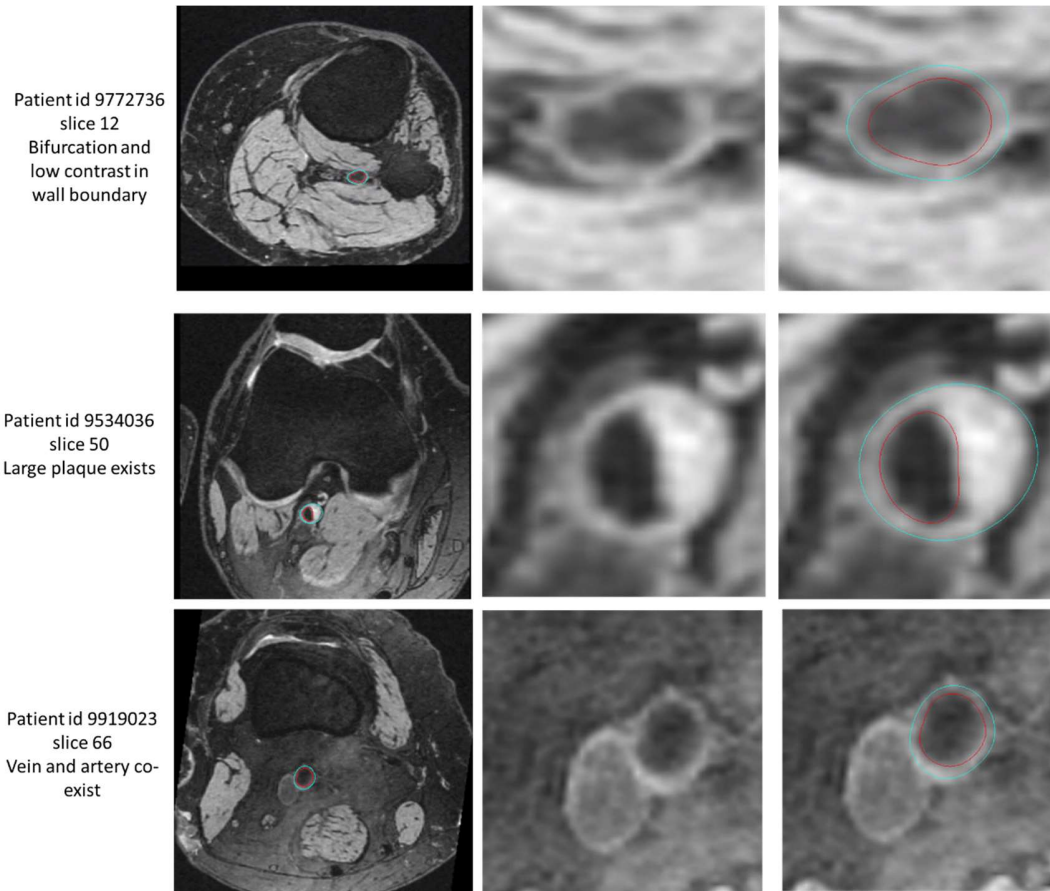
Figure 4.10 Example of *FRAPPE* generated contours.

FRAPPE results (right images. red contour: lumen boundary, blue contour: outer wall boundary) are reliable in challenging images (original images shown in the left, zoomed in images shown in the middle) with low image contrast around vessel wall boundary, bifurcation (top row), plaque (middle row) and when artery is close to the vein (bottom row)

Because of the accuracy and efficiency of *FRAPPE*, over three million images in OAI were processed within two months, and it could take more than 67 years (8 hours per workday) if using manual review.

More details of this approach can be found in our publications [97], [98].

Many exciting research become available using the 3.5 million vessel wall patches and accurate vessel wall segmentations. Three examples were discussed in section 4.3.2 to 4.3.4.

4.3.2   *FRAPPE to summarize vessel wall remodeling patterns*

The most direct way of analyzing the vessel wall from the OAI dataset is to use statistical methods to perform epidemiologic studies, for example, identifying the vessel wall remodeling patterns from the vessel wall morphometry features. The large number of subjects in various vascular health states (about one third have vascular disease) is ideal for the analysis.

Remodeling patterns were studied at the slice level by fitting nonlinear curves relating mean wall thickness (MWT) to mean lumen diameter and mean outer wall diameter while adjusting for sex, age, height, and atherosclerosis risk factors using generalized additive models. The nonparametric bootstrap with resampling by subject (1000 resamples) was used to calculate 95% confidence bands for the spline curves. All analyses were weighted using weights derived from the *FRAPPE* algorithm representing its level of confidence in measurements at the slice level (side-specific), previously shown to improve the repeatability of the measurements.

Spline-smoothed relationships of MWT with lumen and outer wall diameters across 235,152 cross-sectional images in men and 319,953 images in women are shown in Figure 4.11 after adjusting for risk factors. When MWT increased starting from <0.5 mm, both lumen and outer wall diameter also increased on average. When MWT exceeded 0.92 mm (95% CI, 0.91– 0.93 mm) on average for men and 0.84 mm (95% CI, 0.83– 0.85 mm) on average for women, the mean lumen diameter began to steadily decrease with further increases in MWT. Over the range 0.92 to 1.84 in men and 0.84 to 1.68 in women, the average lumen diameter decrease was more rapid in men (−7.9% per 25% increase in MWT; 95% CI, −8.8 to −7.1) than women (−6.1% per 25% increase in MWT; 95% CI, −6.7 to −5.5%; P<0.001 for the difference with men). In contrast, over those same ranges, there was no significant increase in the outer wall diameter in men on average (−0.5% per 25% increase in MWT; 95% CI, −1.2 to 0.1%; P=0.12 compared with 0), while there

was a small but statistically significant increase in outer wall diameter in women (1.2% per 25% increase in MWT; 95% CI, 0.8%–1.7%; P<0.001 compared with men).
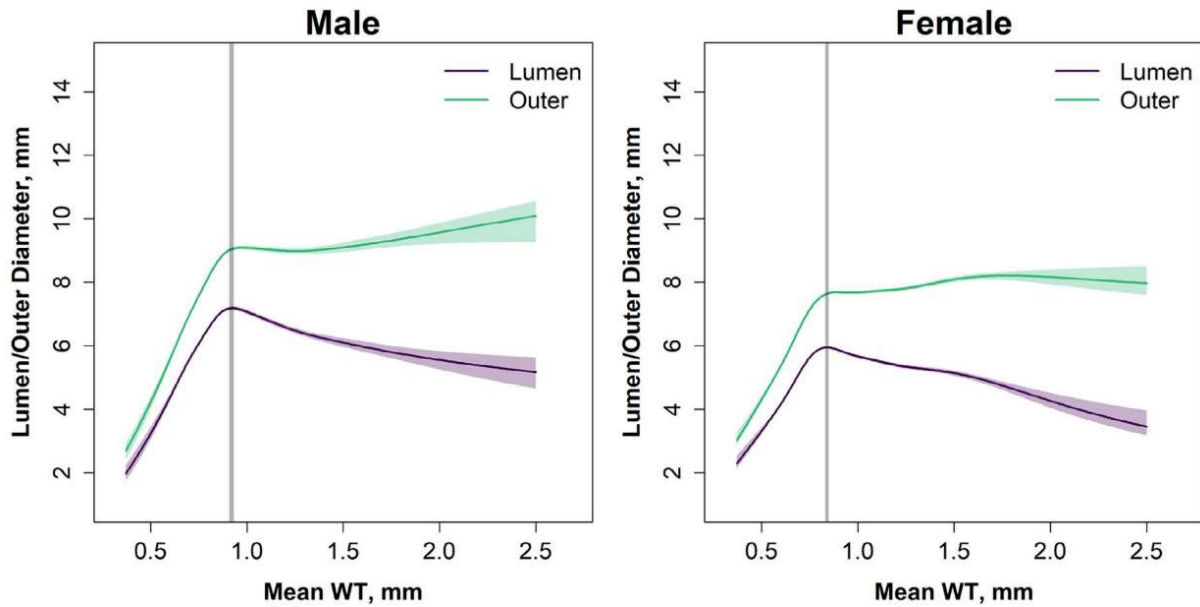
Figure 4.11 Popliteal artery remodeling patterns in men and women.

Spline- smoothed relationships of mean wall thickness with lumen diameter and outer diameter are shown, based on 235 152 and 319 953 cross- sectional images of men and women, respectively. The shaded regions represent 95% pointwise confidence bands. The vertical regions indicate the thickness where on average the mean lumen diameter tends to decrease with increasing thickness (0.92 mm in men and 0.84 mm in women). WT indicates wall thickness.

This study will advance the understanding of subclinical popliteal vascular diseases such atherosclerosis, identifying patients at risk of cardiovascular disease progression or ischemic events. More details of this approach can be found in our publications [100].

4.3.3   *FRAPPE extracted features as new biomarker for cardiovascular risks*

As our research focuses on cardiovascular risk assessments, we identified two groups of subjects who, on the basis of baseline clinical and demographic information, had respectively low or high risk for cardiovascular disease. This allowed us to compare results between high and low risk

groups and to enrich the datasets used for training, validation, and testing with individuals at higher risk of atherosclerosis and plaque in their popliteal arteries. The high-risk group included subjects $\geq$65 years old with a history of smoking, history of hypertension, BMI$\geq$25 kg/m^2, and at least one of seven additional prior events or risk factors: 1) operation to unclog or bypass arteries in legs; 2) stroke, transient ischemic attack, blood clot or bleeding in brain; 3) heart attack; 4) diabetes; 5) current smoker; 6) BMI$\geq$30 kg/m^2; 7) age$\geq$75 years old. The low-risk group included subjects < 55 years old who never smoked, were not hypertensive, had BMI<25 kg/m^2 and had none of the seven additional risk factors specified for the high-risk group.

Artery-based vascular features in subjects with high and low risk for atherosclerosis (Testing Set 4) are summarized in Table 4.6. Mean eccentricity ratio (area under the receiver operating characteristic curve (AUC): 0.79, 95% CI: 0.68-0.89, p=0.005), max wall thickness (AUC: 0.73, 95% CI: 0.60-0.85, p=0.002), and mean wall thickness (AUC: 0.71, 95% CI: 0.57-0.84, p=0.004) were most able to discriminate between high- and low-risk groups based on the AUC.

Table 4.6 Comparison of FRAPPE vessel wall measurements between high and low atherosclerosis risk groups.

Variable	Risk Group		Difference				
	High (N=50)	Low (N=50)	Mean	(95% CI)	P-value	AUC	(95% CI)
Mean wall thickness, mm	0.82 ± 0.08	0.76 ± 0.06	0.06	(0.02, 0.10)	0.004	0.71	(0.57, 0.84)
Max wall thickness, mm	1.97 ± 0.56	1.57 ± 0.43	0.40	(0.16, 0.63)	0.002	0.73	(0.60, 0.85)
Mean eccentricity ratio	1.47 ± 0.20	1.34 ± 0.15	0.13	(0.04, 0.22)	0.005	0.79	(0.68, 0.89)
Mean wall area, mm^2	17 ± 4	16 ± 4	1.2	(-0.9, 3.3)	0.25	0.60	(0.44, 0.75)
Mean lumen area, mm^2	27 ± 8	28 ± 11	-1.0	(-6.3, 4.2)	0.72	0.50	(0.34, 0.67)
Mean total vessel area, mm^2	45 ± 12	44 ± 15	0.2	(-7.1, 7.3)	0.95	0.53	(0.37, 0.69)

Mean normalized wall index, %	39 ± 3	38 ± 4	1.7	(-0.2, 3.5)	0.073	0.65	(0.49, 0.79)
Max normalized wall index, %	49 ± 6	46 ± 7	2.9	(-0.5, 6.2)	0.091	0.64	(0.49, 0.77)

More details of this approach can be found in our publication [97].

4.3.4 *FRAPPE to build vessel wall feature map*

A feature map is a high dimensional representation of image features extractable from the feature embedding layers of the neural network models. With feature maps extracted from the abundant vessel wall images and after feature reduction techniques, the characterization for vessel wall patches and their relations can be represented in human understandable maps. Using feature maps, we can, for example, easily find all the patches with similar plaques or aneurysms.

Starting from the backbone of the vessel wall segmentation CNN, by using the automated generated vessel wall thickness measurements (weak labels) as training labels, and a few highly challenging labeled samples (three rounds of active learning, 256 normal patches and 256 disease patches), a meaningful feature map could be generated [99].

Feature maps before and after metric learning are shown in Figure 4.12. Two clusters in the feature map are less mixed after metric learning, leading to more meaningful feature representations.

Figure 4.13 displays artery patches at selected dots in the feature map. Patches of normal arteries are far away from vessel wall with clear plaques while plaques with similar patterns are close in feature space. Patches at the boundary of two clusters in the feature map are found to be ambiguous and even challenging for expert humans to classify.

Feature map before metric learning   Feature map after metric learning
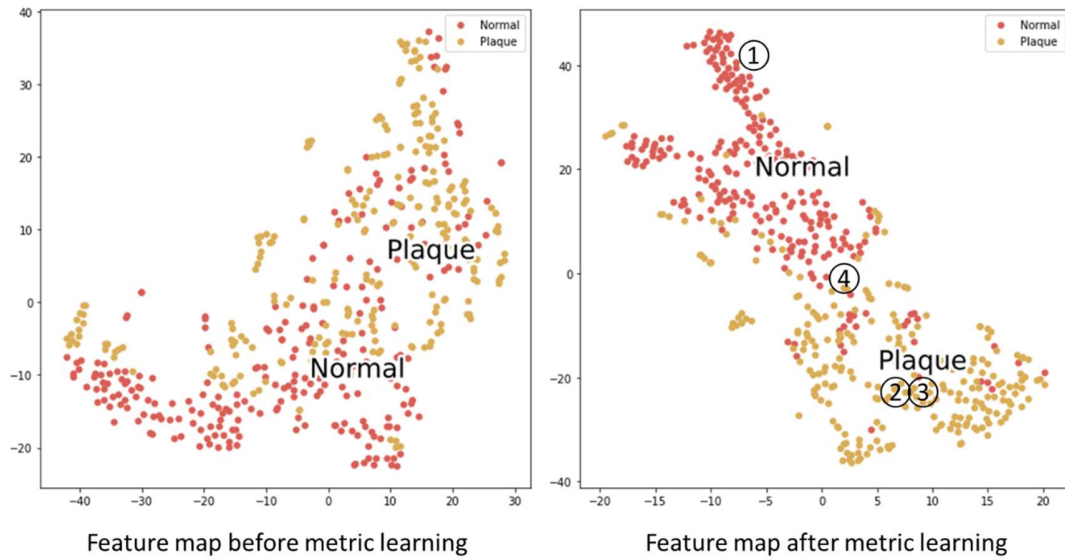
Figure 4.12 Feature map of test data represented in 2D space using t-SNE.

Each dot is represented as the artery patch feature embedding in the feature map. The colors (red for normal arteries, orange for arteries with plaque) are painted from the manual labels for readers to better understand the physical meaning of the feature map. Before metric learning (left figure), a large number of dots from two classes are mixed in feature space, but are separated after metric learning (right figure). Patches at four locations are shown in Figure 4.13.
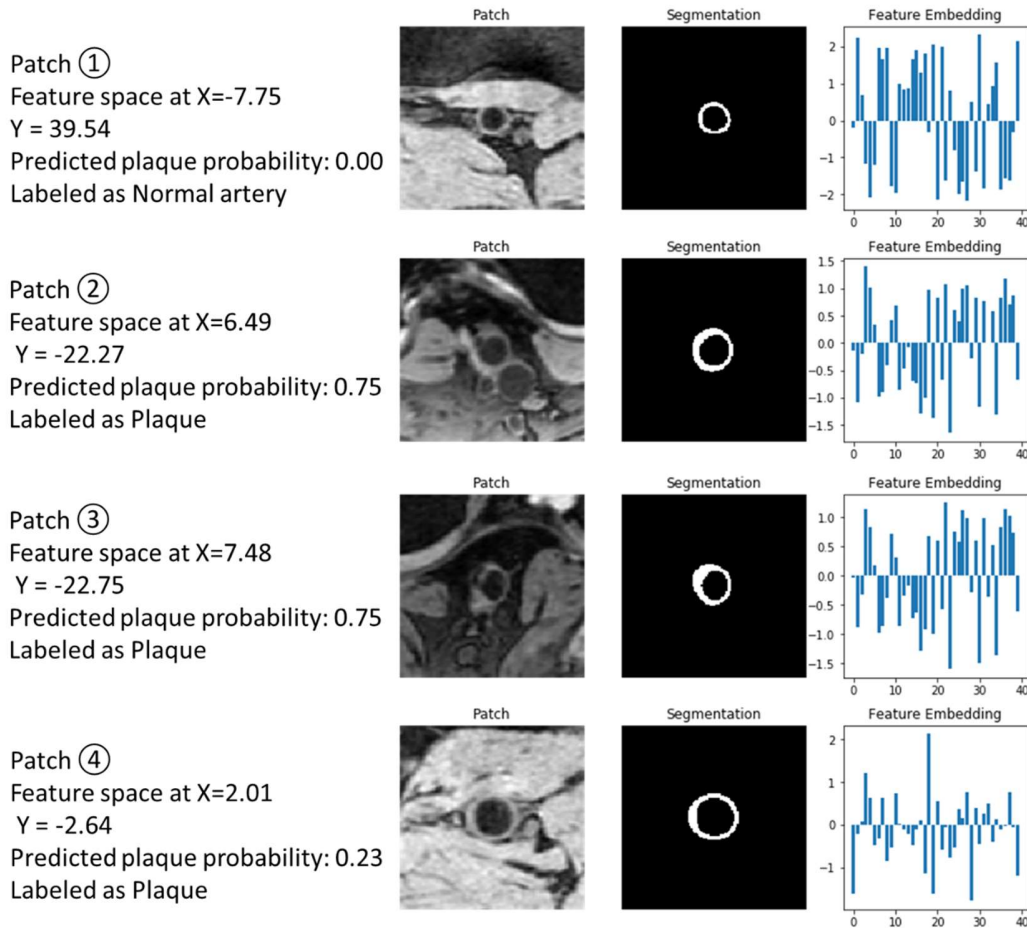
Figure 4.13 Patches, segmentation mask of vessel wall and the bar chart of 40 dimensional feature embeddings at four feature map locations indicated in Figure 4.12.

Patches of normal arteries (①) are far away from vessel wall with clear plaques (②③).

Plaques with similar patterns (②③) are likely to have close distance in the feature space. In this case, both artery patches have calcifications in the vessel wall. Patches at the boundary of two clusters in feature map (④) are likely to be ambiguous slices even challenging for human to decide the class.

More details of this approach can be found in our publication [99].

4.3.5   *Summary*

Like the previous work of vessel wall analysis on carotid arteries [6], vessel wall features generated from *FRAPPE* are also able to offer imaging biomarkers of cardiovascular risk useful

in both research and clinical environments. In addition, we believe *FRAPPE* could have wide applicability wherever knee MRI data are acquired, such as *FRAPPE* could provide an add-on popliteal artery analysis of standard knee MR scans without adding any additional work for radiologists. Although vessel wall features for popliteal arteries have not usually been reported from routine knee scans, these features could provide additional assessments of cardiovascular risks in asymptomatic patients. Subjects identified with thickened vessel wall can then be referred for more detailed examinations for atherosclerosis.

Chapter 5. ATHEROSCLEROTIC LESION IDENTIFICATION AND CLASSIFICATION

After successful artery centerline generation and lumen/vessel wall segmentation, a *quantitative vascular map* can be built to extract vascular structure and plaque features. One step to make the vascular map more meaningful and clinically useful is to add the additional feature about vascular disease locations.

LATTE (another member of *Cafe* family) was designed for automated atherosclerotic lesion identification and assessment to automatically identify high-risk patients for further detailed examination in a time-efficient manner (section 5.1).

Machine learning models developed from one dataset might not perform well on new datasets with slightly different imaging parameters, which leads to our domain adaptive lesion classification which applies an unsupervised domain adaptation method to improve the lesion classification accuracy (section 5.2).

Part of the contents from this chapter were described in details in our previous publications [114]–[117].

5.1   LATTE FOR LESION ASSESSMENTS

While fast 3D carotid MRI is available, manual reading of vessel wall scans is time-consuming and requires extensive review experience, which restricts MR for screening purpose. To automate the vessel wall review, we develop and evaluate a fully automated AI solution for carotid lesion assessment from a 3D fast MRI sequence (*3D-MERGE*) by providing image quality assessment, artery localization and lesion classification. The workflow is called *LATTE* (**L**esion **A**ssessment **T**hrough **T**racklet **E**valuation), shown in Figure 5.1.
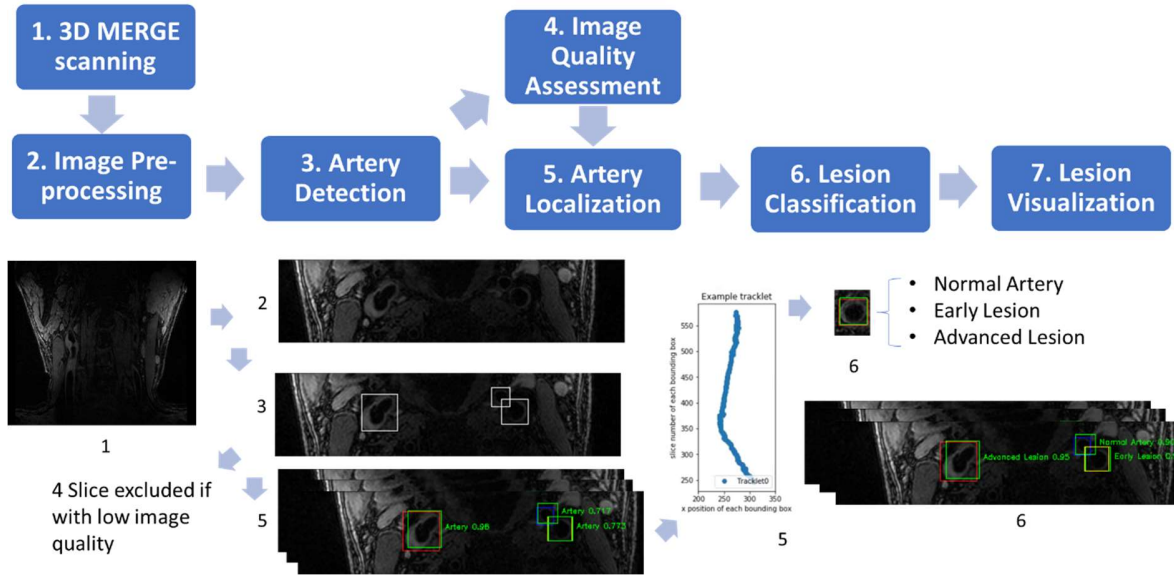
Figure 5.1 Workflow for fully automated carotid atherosclerotic lesion assessment (*LATTE*) in this study.

1) *3D-MERGE* sequence images were acquired. 2) Images were resliced into axial slices and centered of the neck region. 3) Artery detection was performed using a localization neural network model on each slice. 4) Artery-focused image quality assessments were generated for each slice. 5) Artery centerlines were generated using tracklet refinement of artery detection results. 6) Patch based atherosclerotic lesion classification.

As a proof of concept, *LATTE* is focused on carotid artery assessment where atherosclerotic plaques are more critical to overall vascular health. The structure of the carotid artery and the example MR images for *LATTE* analysis is shown in Figure 5.2
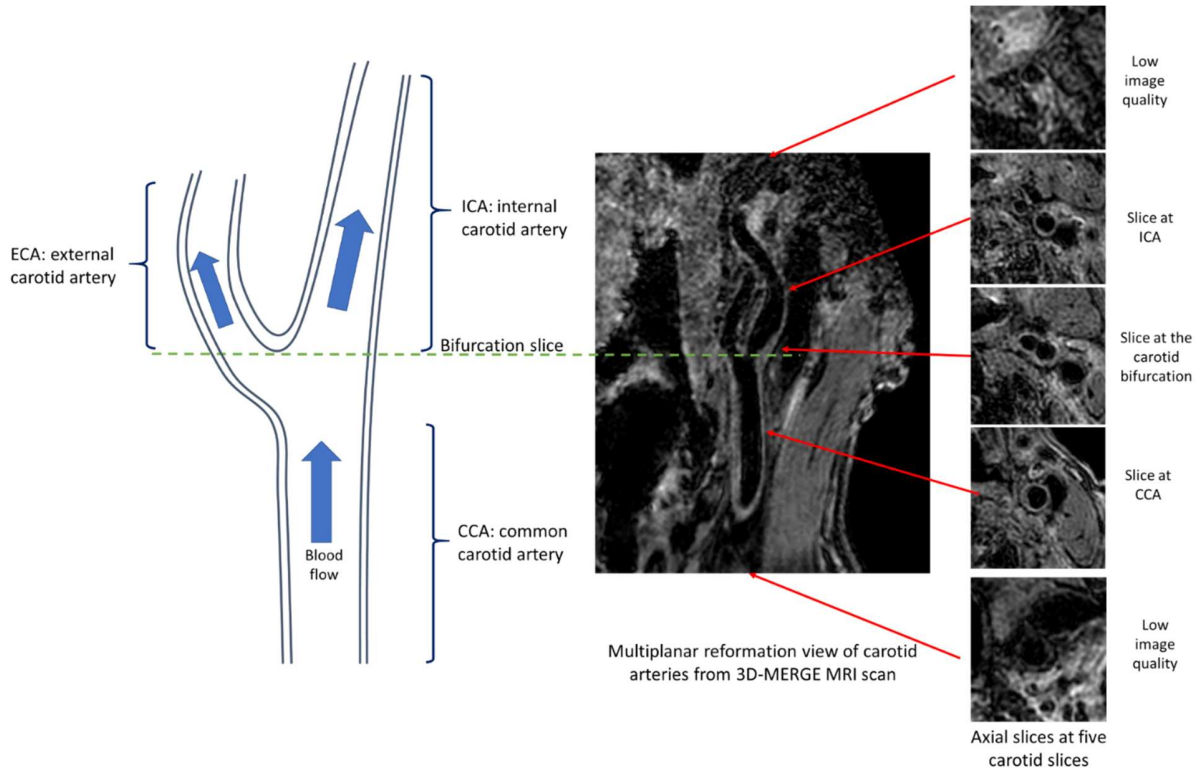
Figure 5.2 Illustration of carotid anatomical regions with example *3D-MERGE* images of carotid arteries from this study.

Slices at both ends have low image qualities, thus the image quality assessment module is used to predict the qualified slices for review.

A fast MR carotid sequence (3D Motion Sensitized Driven Equilibrium prepared Rapid Gradient Echo (*3D-MERGE*) [118]) of about 2 minutes was acquired in coronal direction for vessel wall analysis. Models were trained/validated/tested on 259/20/54 subjects of the Carotid Atherosclerosis Risk Assessment (CARE-II) dataset of 333 subjects acquired from five sites [61].

5.1.1   *LATTE development*
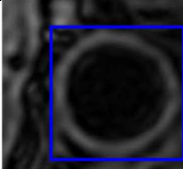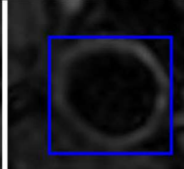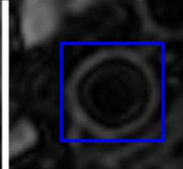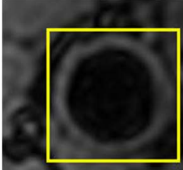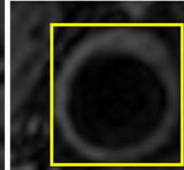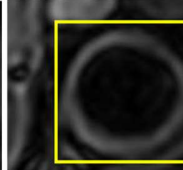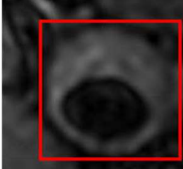
An image quality assessment model was developed to 1) identify whether the scan is of good quality (if the scan is with severe motion artifacts, a rescan is needed), and 2) exclude image slices with low quality to limit the further analysis [115]. Briefly, serial of no-overlapping patches was extracted around artery region (based on artery centerline generation) with weights (higher if closer

to the artery). Then each patch was assessed with a neural network for an image quality score, which were averaged with weights to be the final score. If the overall image quality for the whole slice is below a threshold, the scan was considered useless. If not, the range of slices with sufficient quality scores were used for further analysis.

The artery centerline generation and vessel wall segmentation steps followed the methods introduced in section 3.1and 4.2.

A classification model was used to categorize each artery slice into normal, early lesion and advanced lesion. Definition of three categories is in Table 5.1. Manual labels were given by an experienced radiologist. An average of 148.7 bounding boxes were labeled per scan by the radiologist for the CARE-II dataset, including 15920 bounding boxes for normal arteries (35.8%), 14958 bounding boxes for early lesions (33.6%) and 13582 bounding boxes for advanced lesions (30.5%) with diagnostic image qualities on the CAREII dataset.

Table 5.1 Carotid vessel wall categories with definition and example image slices

Category	Definition	Example image slices
Normal artery	AHA type I-II lesion, normal or near-normal wall thickness	
Early lesion	AHA type I-III lesion, mild wall thickening <1.5mm without complex compositions such as calcification, or lipid-rich necrotic core.	
Advanced lesion	AHA type IV-VIII lesions, plaque lesion with wall thickening ≥1.5mm or occlusion	

Patches with the size of 64*64 are extracted from the center of the points on the artery centerline. In order to select the specific artery wall for classification when multiple artery walls exist in region of interest, (for example, ECA and ICA co-existing on image slices in the bifurcation region), vessel walls are segmented using the polar segmentation model for each carotid artery before classification. The segmented region, as an attention mask, is concatenated with the original patch in the channel dimension of the image. To include neighboring slices information in the classification, two proximal and two distal neighboring patches are extracted along the centerline and concatenated in the depth dimension of the image. Image patches (each patch with size of 64*64*5*2) are then classified using a convolutional neural network for the lesion type of the middle slice.

The output of the model is a continuous variable of risk score trained from labels of -1 (normal artery), 0 (early lesion), and 1 (advanced lesion). Based on the purpose of *LATTE*, two thresholds were selected based on the validation set to divide the risk score range into three classes so that the sensitivity of advanced lesions and all lesions are 0.9. A confidence score (*conf*) can be derived from the risk score according to the distances to the thresholds using the following equation.

$$conf =$$

$$\begin{cases} max\left(0.01, 1 - abs\left(RiskScore - (-1)\right)\right), RiskScore < LowerThreshold \\ max\left(0.01, 1 - abs(RiskScore)\right), LowerThreshold \le RiskScore \le UpperThreshold \\ max\left(0.01, 1 - abs(RiskScore - 1)\right), RiskScore > UpperThreshold \end{cases} \quad (5.1)$$

5.1.2   *Experimental results*

Image quality assessment. For the CARE-II dataset, the image quality assessment model achieved 0.93 in sensitivity and 0.72 in specificity.

Centerline generation. Evaluated on 20 randomly selected scans from the test set with manually annotated 5503 bounding box labels, there were 172 human labeled bounding boxes

without at least 50% IoU with bounding boxes predicted from the model (Miss) and 63 predicted bounding boxes without at least 50% IoU with any human labeled bounding boxes (False detections). Among the 5331 predicted bounding boxes having at least 50% IoU with human labels (Hit), the mean distance to the annotated artery center was 0.82±0.09 pixels (0.28 mm).

Lesion classification. The weighted kappa between the predicted lesion category and the ground truth was 0.65 (0.65-0.65); the AUC was 0.94 for detection of advanced lesions (operating point at sensitivity = 0.92 / specificity = 0.84); the AUC was 0.93 for detection of all lesions (operating point at sensitivity = 0.92 / specificity = 0.86). An example showing prediction and ground truth on one slice from the CARE-II dataset are shown in Figure 5.3.
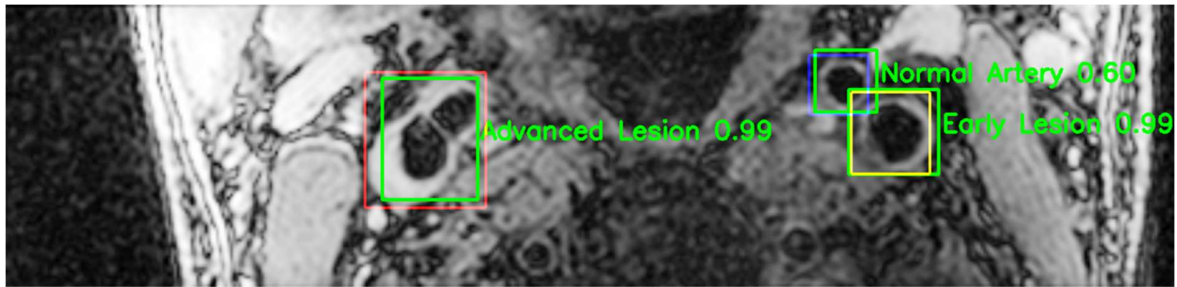
Figure 5.3 *LATTE* results on one slice of carotid artery from the testing set
Green bounding boxes show prediction locations and artery type (text right to the bounding boxes), classification confidence (definition in Supporting Information) follows the artery type. Reference locations by the radiologist shown in blue, yellow and red representing normal arteries, early lesions and advanced lesions, respectively.

Visualization. *LATTE* results can be viewed in *iCafe* GUI for human reviewers by switching between cross-sectional, axial/coronal/sagittal, or curve planar reformatted views to have a detailed examination of the predicted lesion areas.

Review time. Based on our workstation with Intel Xeon E5-1650 V4 @3.6GHz, NVIDIA Titan V and 64GB memory, the average processing time for one case was 6.0 minutes. However, it only took 44.0 seconds to get image quality assessment results. The processing time for artery

detection, artery refinement and lesion classification were 123.4 seconds, 133.9 seconds, 81.6 seconds respectively. The manual review time for each scan (640-720 slices) was around 20-60 minutes depending on vascular anatomy and lesion distribution.

5.2 DOMAIN ADAPTIVE LESION CLASSIFICATION

5.2.1 *Datasets*

We used additional three datasets (CROP/IPH/Renji) with the same *3D-MERGE* MRI sequence but slightly different imaging parameters to test the robustness of the domain adaptive model after it was adapted (no additional annotations needed) to the target dataset. Details of the datasets are described in Table 5.2.

Table 5.2 Dataset division (subject based) and typical image properties of each dataset.

Dataset Name	Number of participating sites	Coronal Image size after interpolation	Coil	3D imaging resolution (mm*mm)	Interpolated resolution (mm*mm)	Echo time/Repetition time (ms)	Scan durations (seconds)
CAREII	5	720*720	8-channel carotid coil	0.7*0.7*0.7	0.35*0.35*0.35	4.8/10.2	250.1
CROP	1	720*720	custom-designed 36-channel neurovascular coil	0.7*0.7*0.7	0.35*0.35*0.35	4.9/10.3	240.3
IPH	1	640 * 640	8-channel carotid coil	0.8*0.8*0.8	0.40*0.40*0.40	4.3/9.1	158.5
Renji	1	640 * 640	8-channel carotid coil	0.8*0.8*0.8	0.40*0.40*0.40	4.4/9.3	160.8

5.2.2 *Unsupervised domain adaptation method*

Enlighted from [119], an unsupervised domain adaptation algorithm was applied to transfer the lesion classifier trained from the CARE-II dataset (source domain) to the three other datasets (target domains) without additional manual annotations. The structure of the domain adaptive classifier and the training strategy is shown in Figure 5.4. Patches of the carotid artery at five consecutive slices with both the original image and the vessel wall segmentation P were used as the input to a convolutional neural network model for lesion category classification. In addition to the source classifier branch $S(P)$, where the artery at the center slice was classified into three categories y, a domain classifier branch $D(P)$ was added after the last convolutional layer to discriminate the domain of the inputs (source or target). An alternate procedure was used in training the network. In step 1, weights of the domain classifier branch were fixed for training the rest of the network using both patches from the source $P_{s,i}$ and target domains $P_{t,i}$. The loss of step 1 l_1 was the sum of the source classifier loss and the domain classifier loss. The source classifier loss is the mean absolute error loss from the source classifier branch where the ground truth category of the center patch of the input $y_{s,i}$ was compared with the predicted category $S(P_{s,i})$. The domain classifier loss is the binary cross entropy loss from the domain classifier branch where the ground truth domain $d_{s/t,i}$ was compared with the predicted domain $D(P_{s/t,i})$. It should be noted that the source classifier did not require labels from patches of the target domain ($y_{t,i}$ set to 0) and the loss calculation of the source classifier did not include target domain patches due to the unsupervised domain adaptation design. i indicates each patch in the source or target domain.

$$l_1 = \sum_i |S(P_{s,i}) - y_{s,i}| + 0 * |S(P_{t,i}) - y_{t,i}| - \frac{1}{N} \sum_i^N d_{s/t,i} \cdot \log\left(D(P_{s/t,i})\right) + (1 - d_{s/t,i}) \cdot$$
$$\log\left(1 - D(P_{s/t,i})\right) \tag{5.2}$$

In step 2, the weights other than the domain classifier were fixed, and the same input was used to train the domain classifier branch only. Importantly, an adversarial approach was used here to invert the domain labels on purpose to train the model, so that if the source classifier was robust enough, it could not tell whether the features extracted from the convolutional layers were originated from the source or target domain. In other words, the convolutional layers were trained to extract only features which were shared across different domains to make a correct classification in the source classifier. The loss in step 2 l_2 was only the binary cross entropy loss from the domain classifier branch.

$$l_2 = -\frac{1}{N}\Sigma_i^N(1 - d_{s/t,i}) \cdot \log\left(D(P_{s/t,i})\right) + d_{s/t,i} \cdot \log\left(1 - D(P_{s/t,i})\right) \qquad (5.3)$$
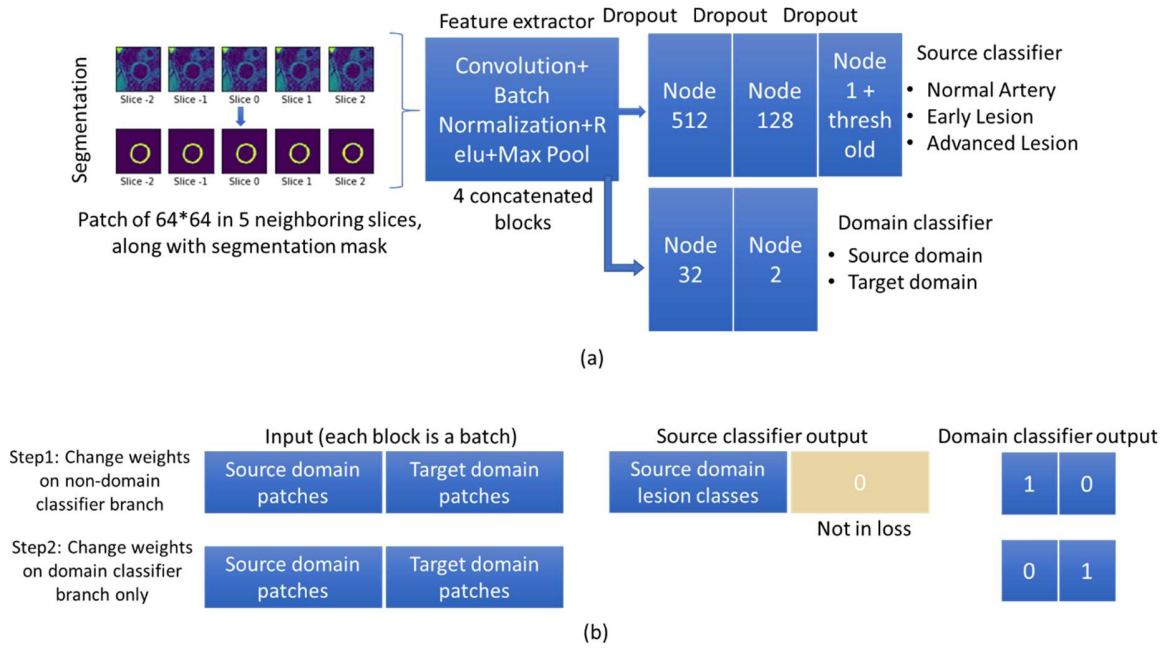
Figure 5.4 Network structure and training strategy for the domain adaptive lesion classification.

(a) Network structure for the domain adaptive lesion classifier. The feature extractor has 4 concatenated blocks of 2 convolutional layer with kernel size of 32, a Relu layer and a max pooling layer with the stride of 2,2,1. The source classifier has three fully connected layers with

512, 128 and 1 nodes (number of neurons) and dropout layers with dropout probability of 0.5. The domain classifier has two fully connected layers with 32 and 1 nodes.

(b) The data flow during the domain adaptive training. In step 1 of domain adaptation training, loss for source classifier (only on source domain patches) and loss for domain classifier were used to change weights on non-domain classifier branch. In step 2 of domain adaptation training, loss for domain classifier were used to change weights on domain classifier branch.

5.2.3   *Experimental results*

On the CROP dataset, the weighted kappa was 0.37 (0.36-0.38); the AUC was 0.88 for detection of advanced lesions (operating point at sensitivity = 0.90 / specificity = 0.67); the AUC was 0.83 for detection of all lesions (operating point at sensitivity = 0.93 / specificity = 0.58).

On the IPH dataset, the weighted kappa was 0.62 (0.61-0.63); the AUC was 0.90 for detection of advanced lesions (operating point at sensitivity = 0.92 / specificity = 0.69); the AUC was 0.90 for detection of all lesions (operating point at sensitivity = 0.94 / specificity = 0.70).

On the Renji dataset, the weighted kappa is 0.68 (0.67-0.68); the AUC is 0.94 for detection of advanced lesions (operating point at sensitivity = 0.90 / specificity = 0.84); the AUC is 0.90 for detection of all lesions (operating point at sensitivity = 0.90 / specificity = 0.72).

Confusion matrices of predicted results compared with ground truth for all four datasets are shown in Table 5.3.

Table 5.3 Confusion matrices for lesion classification results on artery slices of test sets for four datasets used in this study.

Rows are ground truth and columns are predictions. Slices detected by LATTE but not annotated by radiologists were excluded from evaluations.

	LATTE Prediction for CARE-II			LATTE Prediction for CROP			LATTE Prediction for IPH			LATTE Prediction for Renji		
Number of artery slices	Normal Artery	Early Lesion	Advanced	Normal Artery	Early Lesion	Advanced	Normal Artery	Early Lesion	Advanced	Normal Artery	Early Lesion	Advanced

				Lesion			Lesion			Lesion			Lesion
Ground truth from the radiologist's classification	Normal Artery	25147	1472	2727	14052	4690	5534	6324	1208	1537	17173	4286	2389
	Early Lesion	398	640	2588	821	2575	5548	447	1367	2578	1249	2324	2422
	Advanced Lesion	222	122	4059	39	221	2314	63	284	3921	231	652	7943
Sensitivity for advanced lesions		0.92			0.90			0.92			0.90		
Specificity for advanced lesions		0.84			0.67			0.69			0.84		
Sensitivity for all lesions		0.92			0.93			0.94			0.90		
Specificity for all lesions		0.86			0.58			0.70			0.72		
Weighted kappa		0.65 (0.65-0.65)			0.37 (0.36-0.38)			0.62 (0.61-0.63)			0.68 (0.67-0.68)		
Patient bootstrap weighted kappa		0.64 (0.63-0.65)			0.41 (0.40-0.42)			0.55 (0.54-0.56)			0.59 (0.58-0.60)		

The domain adaptation applied on three unseen datasets (CROP, IPH, Renji) showed improvements on lesion classification compared with the baseline method of directly using the model trained from CAREII dataset to predict on unseen datasets. For example, the AUC for advanced lesion detection improved from 0.80 to 0.88, and the AUC for all lesion improved from 0.80 to 0.83 for the CROP dataset. ROC curves before and after domain adaptation are shown in Figure 5.5.
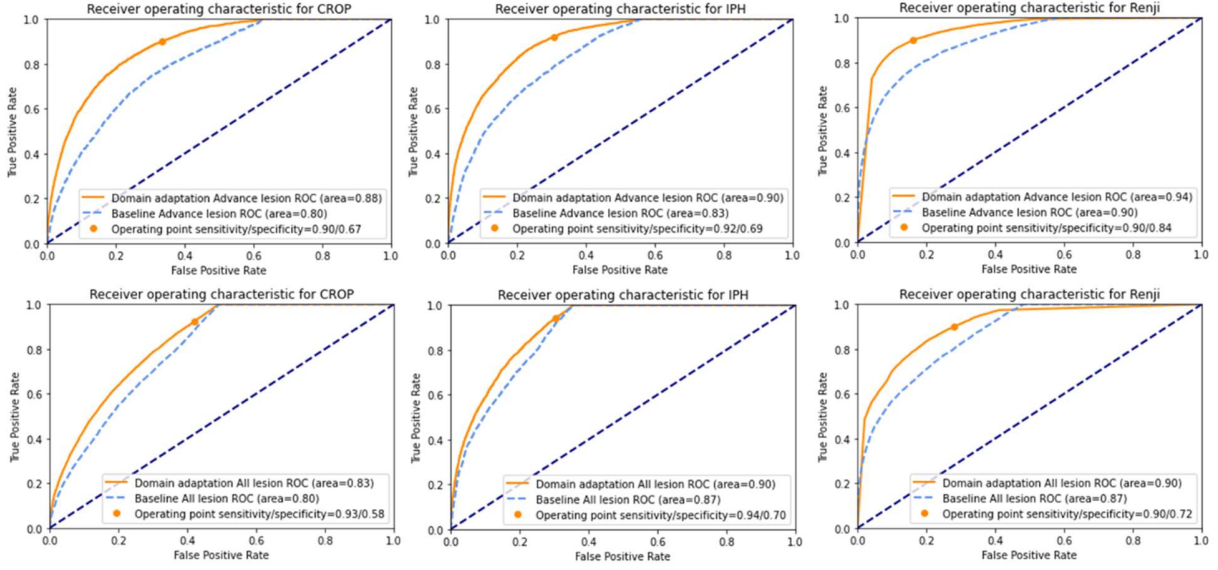
Figure 5.5 Area under the receiver operating characteristic curve for advanced and all lesions before and after domain adaptation.

5.3   SUMMARY

In this chapter, we described *LATTE*, a domain adaptive and fully automated workflow with multiple AI modules, including image quality assessment, centerline generation, and especially lesion classification with domain adaptation. The combined application of *3D-MERGE* and *LATTE* may offer a unique solution where clinical information of carotid atherosclerotic lesion is needed for effective and accurate identification and stratification of atherosclerotic disease severity.

LATTE is a combination of uniquely designed CNN approaches. By incorporating human prior knowledge into the network design (such as using higher weights on patches with arteries in the image quality assessment model) and developed with large sample size (8 sites, 550 subjects, 128,536 labeled artery slices), CNN is able to extract useful image intensity patterns to regress image quality score, locate artery regions, and classify lesions from the annotations of expert reviewers. Most importantly, without further supervised training, the lesion classification is shown to be adaptive to three different datasets (including different imaging parameters, coils and

scanners) by the specially designed domain adaptive CNN structure and training procedure. For vessel wall assessments on a large population from different sites, a domain adaptive and fully automated workflow may greatly reduce radiologists' workload and assist their reading by prioritizing diseased artery segments to review.

In addition, *LATTE* may have the following immediate clinical impacts: 1) during image acquisition, with accurate and fast image quality assessments, *LATTE* could alert the MR operator to rescan if insufficient image quality is found before the subject leaves the scanner, a more time efficient way to control image quality; 2) lesion classification allows high-risk artery segments to be highlighted so that radiologists may focus on the flagged location during the diagnostic review. The high sensitivity of lesion classification indicates significant reduction in manual workload and review time; and 3) with a user-friendly module to visualize the artery structures and lesion locations, radiologists could easily receive beneficial assistance from the AI tool without sophisticated training.

In conclusion, the proposed domain adaptive and fully automated carotid atherosclerosis lesion assessment workflow (*LATTE*) can identify carotid atherosclerotic lesions with a high level of agreement with expert reviewers. Domain adaptation improves the lesion classification performance on new datasets without additional annotations, allowing smooth deployments of *LATTE* as a potentially usable AI solution for carotid atherosclerosis detection and assessment in clinical environments.

More details of this approach can be found in our publications [114]–[117].

Chapter 6. CONCLUSIONS

In this dissertation, we proposed *the Cafe family* toolbox to construct the *quantitative vasculature map* using novel vascular image analysis techniques for 3D vascular images. The *quantitative vasculature map* is especially useful for atherosclerotic plaque assessments where both blood flow (through artery centerlines) and plaque morphometry (through vessel wall segmentation) features are important. The tracklet refinement/*iCafe*/*AICafe* approaches generate accurate artery centerlines for quantifying comprehensive region-based vascular structural features, proved to be useful in a series of vascular research studies. The additional voxel-wise segmentation of lumen/vessel wall regions (through *Y-net*, Polar segmentation or *FRAPPE*) further provides additional lumen and outer wall morphometry features. In addition, atherosclerotic lesion identification and classification are available through analyzing cross-sectional slices along centerlines by *LATTE*. With the vascular structural features, plaque morphometry features, and atherosclerotic lesion features, a *quantitative vasculature map* of human vasculature can be useful for both vascular research and clinical applications.

The development of *the Cafe family* is not possible without the extensive use of AI techniques, which not only help to extract subtle features not possible from human designed feature descriptors, but also automate the image analysis workflow. With AI techniques, unbiased, accurate and meaningful vascular features can be extracted from large population studies for vascular research. The good performance of our AI models is partly due to the joint wisdom between human and machine. Guided by human wisdom by incorporating human's prior knowledge on vasculature in the model design, AI techniques can quickly and robustly learn from human labels following human's thinking patterns.

In addition, the contributions from our work also include constructing a large well curated vascular image dataset carefully labeled by the *iCafe* GUI, which is also a visualization platform for the *quantitative vasculature map*. Part of the dataset has been publicly available to encourage more research on vascular image analysis.

The future work can be among three promising directions. 1) Extend *the Cafe family* toolbox to more vascular beds with more imaging modalities; 2) Construct a vascular feature bank to store vascular features along with clinical/diagnostic features to provide reference for new patients with similar subjects in the feature bank; 3) Transforming the Cafe family toolbox to products with easy access for medical workers.

BIBLIOGRAPHY

[1] E. J. Benjamin *et al.*, "Heart Disease and Stroke Statistics—2017 Update: A Report From the American Heart Association," *Circulation*, vol. 135, no. 10, pp. e146–e603, Mar. 2017, doi: 10.1161/CIR.0000000000000485.

[2] M. Trelles, "Imaging of Cerebrovascular Disease," *Invest. Radiol.*, vol. 51, no. 7, p. e1, 2016, doi: 10.1097/rli.0000000000000302.

[3] J. F. Bentzon, F. Otsuka, R. Virmani, and E. Falk, "Mechanisms of plaque formation and rupture.," *Circ. Res.*, vol. 114, no. 12, pp. 1852–66, 2014, doi: 10.1161/CIRCRESAHA.114.302721.

[4] N. Dieleman *et al.*, "Imaging intracranial vessel wall pathology with magnetic resonance imaging current prospects and future directions," *Circulation*, vol. 130, no. 2. pp. 192–201, Jul. 08, 2014, doi: 10.1161/CIRCULATIONAHA.113.006919.

[5] C. Yuan and D. L. Parker, "Three-Dimensional Carotid Plaque MR Imaging," *Neuroimaging Clinics of North America*, vol. 26, no. 1. Elsevier, pp. 1–12, Feb. 01, 2016, doi: 10.1016/j.nic.2015.09.001.

[6] J. Sun *et al.*, "Carotid magnetic resonance imaging for monitoring atherosclerotic plaque progression: a multicenter reproducibility study," *Int. J. Cardiovasc. Imaging*, vol. 31, no. 1, pp. 95–103, 2015, doi: 10.1007/s10554-014-0532-7.

[7] R. P. Choudhury *et al.*, "Arterial Effects of Canakinumab in Patients With Atherosclerosis and Type 2 Diabetes or Glucose Intolerance," *J. Am. Coll. Cardiol.*, vol. 68, no. 16, pp. 1769–1780, 2016, doi: 10.1016/j.jacc.2016.07.768.

[8] B. J. Alpers, R. G. Berry, and R. M. Paddison, "Anatomical Studies of the Circle of Willis in Normal Brain," *Arch. Neurol. Psychiatry*, vol. 81, no. 4, pp. 409–418, Apr. 1959, doi: 10.1001/archneurpsyc.1959.02340160007002.

[9] Y. Marchenko, I. Volkau, and W. L. Nowinski, "Vascular editor: From angiographic images to 3D vascular models," *J. Digit. Imaging*, vol. 23, no. 4, pp. 386–398, 2010, doi: 10.1007/s10278-009-9194-8.

[10] D. Lesage, E. D. Angelini, I. Bloch, and G. Funka-Lea, "A review of 3D vessel lumen segmentation techniques: Models, features and extraction schemes," *Med. Image Anal.*, vol. 13, no. 6, pp. 819–845, 2009, doi: 10.1016/j.media.2009.07.011.

[11]   P. Bibiloni and S. Massanet, "A survey on curvilinear object segmentation in multiple applications," *Pattern Recognit.*, vol. 60, pp. 949–970, 2016, doi: 10.1016/j.patcog.2016.07.023.

[12]   F. Zhao, Y. Chen, Y. Hou, and X. He, "Segmentation of blood vessels using rule-based and machine- learning-based methods : a review," *Multimed. Syst.*, vol. 0, no. 0, p. 0, 2017, doi: 10.1007/s00530-017-0580-7.

[13]   P. Sanchesa, C. Meyer, V. Vigon, and B. Naegel, "Cerebrovascular network segmentation of MRA images with deep learning," *Proc. - Int. Symp. Biomed. Imaging*, vol. 2019-April, pp. 768–771, 2019, doi: 10.1109/ISBI.2019.8759569.

[14]   Y. Zhang and L. Chen, "DDNet: A Novel Network for Cerebral Artery Segmentation from MRA Images," *Proc. - 2019 12th Int. Congr. Image Signal Process. Biomed. Eng. Informatics, CISP-BMEI 2019*, 2019, doi: 10.1109/CISP-BMEI48845.2019.8965836.

[15]   T. Kitrungrotsakul *et al.*, "VesselNet: A deep convolutional neural network with multi pathways for robust hepatic vessel segmentation," *Comput. Med. Imaging Graph.*, vol. 75, pp. 74–83, 2019, doi: 10.1016/j.compmedimag.2019.05.002.

[16]   G. Tetteh *et al.*, "DeepVesselNet: Vessel Segmentation, Centerline Prediction, and Bifurcation Detection in 3-D Angiographic Volumes," pp. 1–13, 2018, [Online]. Available: http://arxiv.org/abs/1803.09340.

[17]   Y. Wang *et al.*, "JointVesselNet: Joint Volume-Projection Convolutional Embedding Networks for 3D Cerebrovascular Segmentation," in *Medical Image Computing and Computer Assisted Intervention – MICCAI 2020. MICCAI 2020.*, 2020, pp. 106–116.

[18]   Y. Wang *et al.*, "Deep distance transform for tubular structure segmentation in CT scans," in *Proceedings of the IEEE Computer Society Conference on Computer Vision and Pattern Recognition*, 2020, pp. 3832–3841, doi: 10.1109/CVPR42600.2020.00389.

[19]   Y. Wang, A. Narayanaswamy, C. L. Tsai, and B. Roysam, "A broadly applicable 3-D neuron tracing method based on open-curve snake," *Neuroinformatics*, vol. 9, no. 2–3, pp. 193–217, 2011, doi: 10.1007/s12021-011-9110-5.

[20]   S. R. Aylward and E. Bullitt, "Initialization, noise, singularities, and scale in height ridge traversal for tubular object centerline extraction," *IEEE Trans. Med. Imaging*, vol. 21, no. 2, pp. 61–75, 2002, doi: 10.1109/42.993126.

[21]   S. H. Lee and S. Lee, "Adaptive Kalman snake for semi-autonomous 3D vessel tracking,"

Comput. Methods Programs Biomed., vol. 122, no. 1, pp. 56–75, 2015, doi: 10.1016/j.cmpb.2015.06.008.

[22] J. M. Wolterink, R. W. va. Hamersvelt, M. A. Viergever, T. Leiner, and I. Išgum, "Coronary artery centerline extraction in cardiac CT angiography using a CNN-based orientation classifier," *Med. Image Anal.*, vol. 51, pp. 46–60, 2019, doi: 10.1016/j.media.2018.10.005.

[23] H. Yang, J. Chen, Y. Chi, X. Xie, and X. Hua, "Discriminative Coronary Artery Tracking via 3D CNN in Cardiac CT Angiography," in *Lecture Notes in Computer Science (including subseries Lecture Notes in Artificial Intelligence and Lecture Notes in Bioinformatics)*, 2019, vol. 11765 LNCS, pp. 468–476, doi: 10.1007/978-3-030-32245-8_52.

[24] Y. Wang, A. Narayanaswamy, and B. Roysam, "Novel 4-d open-curve active contour and curve completion approach for automated tree structure extraction," *Proc. IEEE Comput. Soc. Conf. Comput. Vis. Pattern Recognit.*, pp. 1105–1112, 2011, doi: 10.1109/CVPR.2011.5995620.

[25] E. Bullitt *et al.*, "Vessel tortuosity and brain tumor malignancy: A blinded study," *Acad. Radiol.*, vol. 12, no. 10, pp. 1232–1240, 2005, doi: 10.1016/j.acra.2005.05.027.

[26] A. Takemura, M. Suzuki, H. Harauchi, and Y. Okumura, "Automatic anatomical labeling method of cerebral arteries in MR-angiography data set.," *Japanese J. Med. Phys.*, vol. 26, no. 4, pp. 187–98, 2006, doi: 10.11323/JJMP2000.26.4_187.

[27] T. Dunås, A. Wåhlin, K. Ambarki, L. Zarrinkoob, J. Malm, and A. Eklund, "A Stereotactic Probabilistic Atlas for the Major Cerebral Arteries," *Neuroinformatics*, vol. 15, no. 1, pp. 101–110, 2017, doi: 10.1007/s12021-016-9320-y.

[28] T. Dunås *et al.*, "Automatic labeling of cerebral arteries in magnetic resonance angiography," *Magn. Reson. Mater. Physics, Biol. Med.*, vol. 29, no. 1, pp. 39–47, Feb. 2016, doi: 10.1007/s10334-015-0512-5.

[29] M. Bilgel, S. Roy, A. Carass, P. A. Nyquist, and J. L. Prince, "Automated anatomical labeling of the cerebral arteries using belief propagation," *Med. Imaging 2013 Image Process.*, vol. 8669, no. March 2013, p. 866918, 2013, doi: 10.1117/12.2006460.

[30] H. Bogunović, J. M. Pozo, R. Cárdenes, and A. F. Frangi, "Automatic identification of internal carotid artery from 3DRA images," in *2010 Annual International Conference of*

the IEEE Engineering in Medicine and Biology, Aug. 2010, vol. 2010, pp. 5343–5346, doi: 10.1109/IEMBS.2010.5626473.

[31] H. Bogunović, J. M. Pozo, R. Cárdenes, and A. F. Frangi, "Anatomical Labeling of the Anterior Circulation of the Circle of Willis Using Maximum a Posteriori Classification," in *Lecture Notes in Computer Science (including subseries Lecture Notes in Artificial Intelligence and Lecture Notes in Bioinformatics)*, vol. 6893 LNCS, no. PART 3, Springer, Berlin, Heidelberg, 2011, pp. 330–337.

[32] H. Bogunović, J. M. Pozo, R. Cardenes, L. S. Roman, and A. F. Frangi, "Anatomical labeling of the circle of willis using maximum a posteriori probability estimation," *IEEE Trans. Med. Imaging*, vol. 32, no. 9, pp. 1587–1599, 2013, doi: 10.1109/TMI.2013.2259595.

[33] D. Robben *et al.*, "Simultaneous segmentation and anatomical labeling of the cerebral vasculature," *Med. Image Anal.*, vol. 32, pp. 201–215, 2016, doi: 10.1016/j.media.2016.03.006.

[34] T. Kawahara, M. Nishikawa, C. Kawahara, T. Inazu, K. Sakai, and G. Suzuki, "Atorvastatin, Etidronate, or Both in Patients at High Risk for Atherosclerotic Aortic Plaques: A Randomized, Controlled Trial," *Circulation*, vol. 127, no. 23, pp. 2327–2335, Jun. 2013, doi: 10.1161/CIRCULATIONAHA.113.001534.

[35] B. A. Wasserman, B. C. Astor, A. Richey Sharrett, C. Swingen, and D. Catellier, "MRI measurements of carotid plaque in the atherosclerosis risk in communities (ARIC) study: Methods, reliability and descriptive statistics," *J. Magn. Reson. Imaging*, vol. 31, no. 2, pp. 406–415, Feb. 2010, doi: 10.1002/jmri.22043.

[36] C. Yuan, E. Lin, J. Millard, and J. N. Hwang, "Closed contour edge detection of blood vessel lumen and outer wall boundaries in black-blood MR images," *Magn. Reson. Imaging*, vol. 17, no. 2, pp. 257–266, 1999, doi: 10.1016/S0730-725X(98)00162-3.

[37] G. Adams, G. W. Vick III, C. Bordelon, W. Insull, and J. Morrisett, "Algorithm for quantifying advanced carotid artery atherosclerosis in humans using MRI and active contours," *Med. Imaging 2002 Image Process.*, vol. 4684, no. May 2002, p. 1448, 2002, doi: 10.1117/12.467110.

[38] H. R. Underhill, W. S. Kerwin, T. S. Hatsukami, and C. Yuan, "Automated measurement of mean wall thickness in the common carotid artery by MRI: A comparison to intima-

media thickness by B-mode ultrasound," *J. Magn. Reson. Imaging*, vol. 24, no. 2, pp. 379–387, 2006, doi: 10.1002/jmri.20636.

[39] A. M. Arias-Lorza *et al.*, "Carotid Artery Wall Segmentation in Multispectral MRI by Coupled Optimal Surface Graph Cuts," *IEEE Trans. Med. Imaging*, vol. 35, no. 3, pp. 901–911, 2016, doi: 10.1109/TMI.2015.2501751.

[40] A. M. Arias Lorza, A. Van Engelen, J. Petersen, A. Van Der Lugt, and M. De Bruijne, "Maximization of regional probabilities using Optimal Surface Graphs: Application to carotid artery segmentation in MRI: Application," *Med. Phys.*, vol. 45, no. 3, pp. 1159–1169, 2018, doi: 10.1002/mp.12771.

[41] J. Petersen *et al.*, "Increasing Accuracy of Optimal Surfaces Using Min-Marginal Energies," *IEEE Trans. Med. Imaging*, vol. 38, no. 7, pp. 1559–1568, 2019, doi: 10.1109/TMI.2018.2890386.

[42] D. Vukadinovic *et al.*, "Segmentation of the outer vessel wall of the common carotid artery in CTA," *IEEE Trans. Med. Imaging*, vol. 29, no. 1, pp. 65–76, 2010, doi: 10.1109/TMI.2009.2025702.

[43] K. Hameeteman *et al.*, "Carotid wall volume quantification from magnetic resonance images using deformable model fitting and learning-based correction of systematic errors.," *Phys. Med. Biol.*, vol. 58, no. 5, pp. 1605–1623, 2013, doi: 10.1088/0031-9155/58/5/1605.

[44] J. Wu *et al.*, "Deep Morphology Aided Diagnosis Network for Segmentation of Carotid Artery Vessel Wall and Diagnosis of Carotid Atherosclerosis on Black-Blood Vessel Wall MRI," *Med. Phys.*, p. mp.13739, Jul. 2019, doi: 10.1002/mp.13739.

[45] F. Shi *et al.*, "Intracranial Vessel Wall Segmentation Using Convolutional Neural Networks," *IEEE Trans. Biomed. Eng.*, vol. 66, no. 10, pp. 2840–2847, 2019, doi: 10.1109/TBME.2019.2896972.

[46] R. Van't Klooster *et al.*, "Automatic lumen and outer wall segmentation of the carotid artery using deformable three-dimensional models in MR angiography and vessel wall images," *J. Magn. Reson. Imaging*, vol. 35, no. 1, pp. 156–165, 2012, doi: 10.1002/jmri.22809.

[47] S. Gao *et al.*, "Quantification of common carotid artery and descending aorta vessel wall thickness from MR vessel wall imaging using a fully automated processing pipeline," *J.*

Magn. Reson. Imaging, vol. 45, no. 1, pp. 215–228, Jan. 2017, doi: 10.1002/jmri.25332.

[48] L. Chen *et al.*, "Development of a quantitative intracranial vascular features extraction tool on 3D MRA using semiautomated open-curve active contour vessel tracing," *Magn. Reson. Med.*, vol. 79, no. 6, pp. 3229–3238, 2018, doi: 10.1002/mrm.26961.

[49] L. Chen *et al.*, "Quantification of morphometry and intensity features of intracranial arteries from 3D TOF MRA using the intracranial artery feature extraction (iCafe): A reproducibility study," *Magn. Reson. Imaging*, vol. 57, no. December 2018, pp. 293–302, 2018, doi: 10.1016/j.mri.2018.12.007.

[50] L. Chen *et al.*, "Quantitative Assessment of the Intracranial Vasculature in an Older Adult Population using iCafe (intraCranial Artery Feature Extraction)," *Neurobiol. Aging*, vol. 79, pp. 59–65, 2019, doi: 10.1016/j.neurobiolaging.2019.02.027.

[51] L. Chen *et al.*, "A novel algorithm for refining cerebral vascular measurements in infants and adults," *J. Neurosci. Methods*, vol. 340, no. April, p. 108751, 2020, doi: 10.1016/j.jneumeth.2020.108751.

[52] L. Chen, T. Hatsukami, J.-N. Hwang, and C. Yuan, "Automated Intracranial Artery Labeling Using a Graph Neural Network and Hierarchical Refinement," in *International Conference on Medical Image Comput- ing and Computer-Assisted Intervention*, 2020, vol. 3, pp. 76–85, doi: 10.1007/978-3-030-59725-2_8.

[53] L. Chen *et al.*, "Automated Artery Localization and Vessel Wall Segmentation using Tracklet Refinement and Polar Conversion," *IEEE Access*, vol. 8, pp. 1–1, 2020, doi: 10.1109/access.2020.3040616.

[54] L. Chen *et al.*, "Quantitative Assessment of the Intracranial Vasculature of Infants and Adults Using iCafe (Intracranial Artery Feature Extraction)," vol. 12, no. May, pp. 1–9, 2021, doi: 10.3389/fneur.2021.668298.

[55] L. Chen *et al.*, "Automated detection and labeling of the intracranial arterial tree in routine MR angiography: A machine learning approach enhanced with structural saliency," *Radiol. Soc. North Am. 103rd Sci. Assem. Annu. Meet. Novemb. 26 to December 1, 2017, McCormick Place, Chicago, Illinois.*, 2017.

[56] L. Chen, W. Liu, and N. Balu, "Deep Open Snake Tracker for Vessel Tracing," in *International Conference on Medical Image Comput- ing and Computer-Assisted Intervention*, 2021.

[57]   J. Redmon and A. Farhadi, "YOLO9000: Better, faster, stronger," *Proc. - 30th IEEE Conf. Comput. Vis. Pattern Recognition, CVPR 2017*, vol. 2017-Janua, pp. 6517–6525, 2017, doi: 10.1109/CVPR.2017.690.

[58]   O. Ronneberger, P. Fischer, and T. Brox, "U-Net: Convolutional Networks for Biomedical Image Segmentation," in *Medical Image Computing and Computer-Assisted Intervention – MICCAI 2015*, 2015, pp. 234–241, doi: 10.1007/978-3-319-24574-4_28.

[59]   N. Otsu, "A Threshold Selection Method from Gray-Level Histograms," *IEEE Trans. Syst. Man. Cybern.*, vol. 9, no. 1, pp. 62–66, Jan. 1979, doi: 10.1109/TSMC.1979.4310076.

[60]   F. Schroff and J. Philbin, "FaceNet: A Unified Embedding for Face Recognition and Clustering." Accessed: Oct. 28, 2018. [Online]. Available: https://www.cv-foundation.org/openaccess/content_cvpr_2015/app/1A_089.pdf.

[61]   X. Zhao, R. Li, D. S. Hippe, T. S. Hatsukami, and C. Yuan, "Chinese Atherosclerosis Risk Evaluation (CARE II) study: a novel cross-sectional, multicentre study of the prevalence of high-risk atherosclerotic carotid plaque in Chinese patients with ischaemic cerebrovascular events—design and rationale," *Stroke Vasc. Neurol.*, vol. 2, no. 1, pp. 15–20, 2017, doi: 10.1136/svn-2016-000053.

[62]   J. Sun *et al.*, "Subclinical Carotid Atherosclerosis: Short-term Natural History of Lipid-rich Necrotic Core—A Multicenter Study with MR Imaging," *Radiology*, vol. 268, no. 1, pp. 61–68, Jul. 2013, doi: 10.1148/radiol.13121702.

[63]   T. Yoneyama *et al.*, "In vivo semi-automatic segmentation of multicontrast cardiovascular magnetic resonance for prospective cohort studies on plaque tissue composition: initial experience," *Int. J. Cardiovasc. Imaging*, vol. 32, no. 1, pp. 73–81, Jan. 2016, doi: 10.1007/s10554-015-0704-0.

[64]   D. Xu, W. S. Kerwin, T. Saam, M. Ferguson, and C. Yuan, "CASCADE : Computer Aided System for Cardiovascular Disease Evaluation," *Magn. Reson. Imaging*, vol. 11, no. 1, pp. 1922–1922, 2004.

[65]   L. G. Nyul, J. K. Udupa, and X. Zhang, "New variants of a method of MRI scale standardization," *IEEE Trans. Med. Imaging*, vol. 19, no. 2, pp. 143–150, 2000, doi: 10.1109/42.836373.

[66]   N. Phansalkar, S. More, A. Sabale, and M. Joshi, "Adaptive local thresholding for

detection of nuclei in diversity stained cytology images," *ICCSP 2011 - 2011 Int. Conf. Commun. Signal Process.*, pp. 218–220, 2011, doi: 10.1109/ICCSP.2011.5739305.

[67] A. F. Frangi, W. J. Niessen, K. L. Vincken, and M. A. Viergever, "Multiscale vessel enhancement filtering," *Medial Image Comput. Comput. Invervention - MICCAI'98. Lect. Notes Comput. Sci. vol 1496*, vol. 1496, no. 6, pp. 130–137, 1998, doi: 10.1016/j.media.2004.08.001.

[68] L. Chen and D. Wang, "An improved acquaintance immunization strategy for complex network," *J. Theor. Biol.*, vol. 385, pp. 58–65, 2015, doi: 10.1016/j.jtbi.2015.07.037.

[69] T. Y. Zhang and C. Y. Suen, "A fast parallel algorithm for thinning digital patterns," *Commun. ACM*, vol. 27, no. 3, pp. 236–239, Mar. 1984, doi: 10.1145/357994.358023.

[70] J. B. Kruskal, "On the shortest spanning subtree of a graph and the traveling salesman problem," *Proc. Am. Math. Soc.*, vol. 7, no. 1, pp. 48–48, Jan. 1956, doi: 10.1090/S0002-9939-1956-0078686-7.

[71] W. Liu *et al.*, "Arterial elasticity, endothelial function and intracranial vascular health: A multimodal MRI study," *J. Cereb. Blood Flow Metab.*, p. 0271678X2095695, Oct. 2020, doi: 10.1177/0271678X20956950.

[72] W. Liu *et al.*, "Uncontrolled hypertension associates with subclinical cerebrovascular health globally: a multimodal imaging study," *Eur. Radiol.*, Sep. 2020, doi: 10.1007/s00330-020-07218-5.

[73] M. Schaap *et al.*, "Standardized evaluation methodology and reference database for evaluating coronary artery centerline extraction algorithms," *Med. Image Anal.*, vol. 13, no. 5, pp. 701–714, 2009, doi: 10.1016/j.media.2009.06.003.

[74] L. Chen *et al.*, "Quantification of morphometry and intensity features of intracranial arteries from 3D TOF MRA using the intracranial artery feature extraction (iCafe): A reproducibility study," *Magn. Reson. Imaging*, vol. 57, no. November 2018, pp. 293–302, 2019, doi: 10.1016/j.mri.2018.12.007.

[75] K. Bernardin and R. Stiefelhagen, "Evaluating multiple object tracking performance: The CLEAR MOT metrics," *Eurasip J. Image Video Process.*, vol. 2008, 2008, doi: 10.1155/2008/246309.

[76] K. N. Kayembe, M. Sasahara, and F. Hazama, "Cerebral aneurysms and variations in the circle of Willis.," *Stroke*, vol. 15, no. 5, pp. 846–850, 1984, doi:

10.1161/01.STR.15.5.846.

[77]   B. J. Alpers, R. G. Berry, and R. M. Paddison, "Anatomical studies of the circle of Willis in normal brain.," *AMA. Arch. Neurol. Psychiatry*, vol. 81, no. 4, pp. 409–18, Apr. 1959, Accessed: Feb. 09, 2017. [Online]. Available: http://www.ncbi.nlm.nih.gov/pubmed/13636509.

[78]   L. Chen *et al.*, "Quantitative Intracranial Vasculature Assessment to detect dementia using the intraCranial Artery Feature Extraction (iCafe) Technique," *Proc. Annu. Meet. Int. Soc. Magn. Reson. Med. Palais des congrès Montréal, Montréal, QC, Canada May 11-16*, 2019.

[79]   J. Zhou *et al.*, "Graph Neural Networks: A Review of Methods and Applications," pp. 1–22, 2018, [Online]. Available: http://arxiv.org/abs/1812.08434.

[80]   P. W. Battaglia *et al.*, "Relational inductive biases, deep learning, and graph networks," *arXiv*, pp. 1–40, 2018, [Online]. Available: http://arxiv.org/abs/1806.01261.

[81]   Z. Zhai *et al.*, "Linking Convolutional Neural Networks with Graph Convolutional Networks: Application in Pulmonary Artery-Vein Separation," *Lect. Notes Comput. Sci. (including Subser. Lect. Notes Artif. Intell. Lect. Notes Bioinformatics)*, vol. 11849 LNCS, no. September, pp. 36–43, 2019, doi: 10.1007/978-3-030-35817-4_5.

[82]   J. M. Wolterink, T. Leiner, and I. Išgum, "Graph Convolutional Networks for Coronary Artery Segmentation in Cardiac CT Angiography," *Lect. Notes Comput. Sci. (including Subser. Lect. Notes Artif. Intell. Lect. Notes Bioinformatics)*, vol. 11849 LNCS, pp. 62–69, 2019, doi: 10.1007/978-3-030-35817-4_8.

[83]   J. Gilmer, S. S. Schoenholz, P. F. Riley, O. Vinyals, and G. E. Dahl, "Neural Message Passing for Quantum Chemistry."

[84]   A. Pinto, V. Alves, and C. A. Silva, "Brain Tumor Segmentation using Convolutional Neural Networks in MRI Images," *IEEE Trans. Med. Imaging*, vol. 35, no. 5, pp. 1240–1251, 2016, doi: 10.1109/TMI.2016.2538465.

[85]   Z. Chen *et al.*, "Intracranial vascular feature changes in time of flight MR angiography in patients undergoing carotid revascularization surgery," *Magn. Reson. Imaging*, vol. 75, no. August 2020, pp. 45–50, 2021, doi: 10.1016/j.mri.2020.10.004.

[86]   M. Kass, A. Witkin, and D. Terzopoulos, "Snakes: Active contour models," *International Journal of Computer Vision*, vol. 1, no. 4. pp. 321–331, 1988, doi: 10.1007/BF00133570.

[87] F. Gao and L. Han, "Implementing the Nelder-Mead simplex algorithm with adaptive parameters," *Comput. Optim. Appl.*, vol. 51, no. 1, pp. 259–277, Jan. 2012, doi: 10.1007/s10589-010-9329-3.

[88] M. Shirakawa *et al.*, "Quantitative assessment of cerebrovascular structure after carotid revascularization using intraCranial Artery Feature Extraction (iCafe) Technique," *Proc. Annu. Meet. Int. Soc. Magn. Reson. Med. Montréal, QC, Canada, 11-16 May, 2019*, 2019.

[89] Q. Zhang *et al.*, "Angiographic contrast mechanism comparison between Simultaneous Non-contrast Angiography and intraPlaque hemorrhage (SNAP) sequence and Time of Flight (TOF) sequence for intracranial artery," *Magn. Reson. Imaging*, vol. 66, no. May 2019, pp. 199–207, 2019, doi: 10.1016/j.mri.2019.09.001.

[90] L. Chen *et al.*, "Development of a Quantitative Assessment tool for Peripheral Artery Feature Extraction (pCafe)," *Proc. Annu. Meet. Int. Soc. Magn. Reson. Med. Montréal, QC, Canada, 11-16 May, 2019*, 2019, doi: 10.1002/mrm.26961.9.

[91] Y. Xiong *et al.*, "Findings from SNAP-MRA and PCASL in Patients with Parkinson's Disease 'OFF' and 'ON' Levodopa," *Proc. Jt. Annu. Meet. ISMRM-ESMRMB, Paris, Fr.*, p. 419, 2018, [Online]. Available: http://indexsmart.mirasmart.com/ISMRM2018/PDFfiles/0419.html.

[92] W. Liu *et al.*, "Understanding Atherosclerosis Through an Osteoarthritis Data Set," *Arterioscler. Thromb. Vasc. Biol.*, pp. 1–8, 2019, doi: 10.1161/ATVBAHA.119.312513.

[93] A. Gould *et al.*, "Vessel length on SNAP MRA and TOF MRA is a potential imaging biomarker for brain blood flow," *Magn. Reson. Imaging*, vol. 79, no. October 2020, pp. 20–27, 2021, doi: 10.1016/j.mri.2021.02.012.

[94] L. Chen *et al.*, "3D intracranial artery segmentation using a convolutional autoencoder," in *2017 IEEE International Conference on Bioinformatics and Biomedicine (BIBM) 3D*, Nov. 2017, doi: 10.1109/BIBM.2017.8217741.

[95] L. Chen *et al.*, "Automatic Segmentation of Carotid Vessel Wall Using Convolutional Neural Network," *Proc. Annu. Meet. Int. Soc. Magn. Reson. Med. Paris, Fr. 16-21 June, 2018*, 2018.

[96] L. Chen *et al.*, "Automated Artery Localization and Vessel Wall Segmentation of Magnetic Resonance Vessel Wall Images using Tracklet Refinement and Polar Conversion," *arXiv*, Sep. 2019, [Online]. Available: http://arxiv.org/abs/1909.02087.

[97] L. Chen *et al.*, "Fully automated and robust analysis technique for popliteal artery vessel wall evaluation (FRAPPE) using neural network models from standardized knee MRI," *Magn. Reson. Med.*, vol. 84, no. 4, pp. 2147–2160, 2020, doi: 10.1002/mrm.28237.

[98] D. S. Hippe *et al.*, "Confidence weighting for robust automated measurements of popliteal vessel wall magnetic resonance imaging," *Circ. Genomic Precis. Med.*, no. February, pp. 39–41, 2020, doi: 10.1161/CIRCGEN.119.002870.

[99] L. Chen *et al.*, "Visualizing and utilizing latent features of MR vessel wall images using weakly supervised deep learning analysis workflow," in *Proceedings of the Annual Meeting of the International Society for Magnetic Resonance in Medicine, 2020*, 2020, doi: 10.1002/mp.13739.

[100] G. Canton *et al.*, "Atherosclerotic Burden and Remodeling Patterns of the Popliteal Artery as Detected in the Magnetic Resonance Imaging Osteoarthritis Initiative Data Set," *J. Am. Heart Assoc.*, vol. in press, p. JAHA.120.018408, May 2021, doi: 10.1161/JAHA.120.018408.

[101] L. R. Dice, "Measures of the Amount of Ecologic Association Between Species," *Ecology*, vol. 26, no. 3, pp. 297–302, Jul. 1945, doi: 10.2307/1932409.

[102] L. Chen *et al.*, "Y-net: 3D intracranial artery segmentation using a convolutional autoencoder," in *arXiv*, 2017, doi: 10.1109/BIBM.2017.8217741.

[103] C. H. Sudre, W. Li, T. Vercauteren, S. Ourselin, and M. Jorge Cardoso, "Generalised Dice Overlap as a Deep Learning Loss Function for Highly Unbalanced Segmentations," in *Lecture Notes in Computer Science (including subseries Lecture Notes in Artificial Intelligence and Lecture Notes in Bioinformatics)*, vol. 10553 LNCS, 2017, pp. 240–248.

[104] K. He, X. Zhang, S. Ren, and J. Sun, "Deep Residual Learning for Image Recognition," *arXiv*, May 2015, [Online]. Available: https://arxiv.org/abs/1512.03385.

[105] J. Deng, W. Dong, R. Socher, L.-J. Li, Kai Li, and Li Fei-Fei, "ImageNet: A large-scale hierarchical image database," in *2009 IEEE Conference on Computer Vision and Pattern Recognition*, Jun. 2009, pp. 248–255, doi: 10.1109/CVPR.2009.5206848.

[106] K. He, G. Gkioxari, P. Dollar, and R. Girshick, "Mask R-CNN," *Proc. IEEE Int. Conf. Comput. Vis.*, vol. 2017-Octob, pp. 2980–2988, 2017, doi: 10.1109/ICCV.2017.322.

[107] E. Angelie, E. R. Oost, D. Hendriksen, B. P. F. Lelieveldt, R. J. Van der Geest, and J. H. C. Reiber, "Automated Contour Detection in Cardiac MRI Using Active Appearance

Models," *Invest. Radiol.*, vol. 42, no. 10, pp. 697–703, 2007, doi: 10.1097/rli.0b013e318070dc93.

[108] J. J. Bartko, "Measurement and reliability: statistical thinking considerations.," *Schizophr. Bull.*, vol. 17, no. 3, pp. 483–9, 1991, Accessed: Jun. 27, 2017. [Online]. Available: http://www.ncbi.nlm.nih.gov/pubmed/1947873.

[109] K. He, G. Gkioxari, P. Dollár, and R. Girshick, "Mask R-CNN," *IEEE Trans. Pattern Anal. Mach. Intell.*, vol. 42, no. 2, pp. 386–397, 2020, doi: 10.1109/TPAMI.2018.2844175.

[110] L. Chen *et al.*, "Automatic Segmentation of Carotid Vessel Wall Using Convolutional Neural Network," *Proc. Annu. Meet. Int. Soc. Magn. Reson. Med. Paris, Fr. 16-21 June, 2018*, vol. 96, pp. 2017–2018, 2018, doi: 10.1002/jmri.22043.6.

[111] T. K. Koo and M. Y. Li, "A Guideline of Selecting and Reporting Intraclass Correlation Coefficients for Reliability Research," *J. Chiropr. Med.*, vol. 15, no. 2, pp. 155–163, 2016, doi: 10.1016/j.jcm.2016.02.012.

[112] A. Padua and J. Carrino, "3T MR Imaging of Cartilage using 3D Dual Echo Steady State (DESS)," *MAGNETOM Flash*, pp. 33–36, 2011, [Online]. Available: http://www.healthcare.siemens.de/siemens_hwem-hwem_ssxa_websites-context-root/wcm/idc/groups/public/@global/@imaging/@mri/documents/download/mdaw/mdex/~edisp/3t_mr_imaging_of_cartilage_using_3d_dual_echo_steady_state-00011808.pdf.

[113] Y. Wang *et al.*, "Association between popliteal artery wall thickness and knee structure in adults without clinical disease of the knee: A prospective cohort study," *Arthritis Rheumatol.*, vol. 67, no. 2, pp. 414–422, 2015, doi: 10.1002/art.38922.

[114] L. Chen *et al.*, "Domain adaptive and fully automated carotid artery atherosclerotic lesion detection using an artificial intelligence approach (LATTE) on 3D MRI," *Magn. Reson. Med.*, no. February, pp. 1–12, 2021, doi: 10.1002/mrm.28794.

[115] H. Jiang *et al.*, "A target-oriented and multi-patch based framework for image quality assessment on carotid artery MRI," in *Medical Imaging 2020: Image Processing*, Mar. 2020, p. 81, doi: 10.1117/12.2549473.

[116] L. Chen *et al.*, "Carotid Artery Localization and Lesion Detection on 3D-MERGE MRI through Online Learning," *Soc. Magn. Reson. Angiogr. 30th Annu. Int. Conf. August 29 – 31, 2018 Glas. Scotl.*, vol. 1, p. 2017, 2018.

[117] L. Chen *et al.*, "Carotid Artery Localization and Lesion Classification on 3D-MERGE MRI using Neural Network and Object Tracking methods," *Proc. Annu. Meet. Int. Soc. Magn. Reson. Med. Montréal, QC, Canada, 11-16 May, 2019*, 2019.

[118] N. Balu, V. L. Yarnykh, B. Chu, J. Wang, T. Hatsukami, and C. Yuan, "Carotid plaque assessment using fast 3D isotropic resolution black-blood MRI," *Magn. Reson. Med.*, vol. 65, no. 3, pp. 627–637, 2011, doi: 10.1002/mrm.22642.

[119] Y. Ganin and V. Lempitsky, "Unsupervised Domain Adaptation by Backpropagation," in *Proceedings of the 32nd International Conference on Machine Learning*, Sep. 2015, [Online]. Available: http://arxiv.org/abs/1409.7495.

APPENDIX A

Useful links for more information.

My full list of publications: https://clatfd.cn/cv#pub

Our open-source repository and resources:

- GNN artery labeling: https://github.com/clatfd/GNN-ART-LABEL

- Domain adaptive lesion classification: https://github.com/clatfd/DANN

- Polar segmentation: https://github.com/clatfd/PolarReg

- OAI dataset vessel wall manual annotations: https://github.com/clatfd/OAI-Polar

- Academic use of *iCafe* is available through reasonable request by sending email to lab manager Mr. Zach Miller (zach1@uw.edu) and Dr. Dongxiang Xu (xdx@uw.edu)

- iCafe user guide: https://1drv.ms/w/s!AqZ4RxQg6dp-7XX7_yu1jXxpSbg7

- *iCafe* demo video by Li Chen: https://www.youtube.com/playlist?list=PLxG3HeAddxYb_KQbL2fKNV5BW99yMCksY

As the organizer, we held the Carotid Artery Vessel Wall Segmentation Challenge endorsed by SMRA 2021 and MICCAI 2021, attracted 194 participants: https://vessel-wall-segmentation.grand-challenge.org/

Project websites:

- *iCafe*: http://icafe.clatfd.cn/

- *FRAPPE:* http://clatfd.cn/a/312

- *LATTE*: http://clatfd.cn/a/321

VITA

Li Chen received the B.S. degree in Electrical Engineering from Fudan University in 2016. His research interests include medical image analysis and machine learning. He is the author for 28 peer-reviewed full-length papers (15 as the first author) ranging from technical innovations, medical applications, and clinical research. He is the current member of IEEE, MICCAI and ISMRM. He received Outstanding Research Award from OCSMRM, and Magna Cum Laude Merit Awards from ISMRM in 2019 and 2020. He is an active reviewer for multiple conferences and journals, including MICCAI, CVPR, IEEE Access, Magnetic Resonance Imaging, Stroke & Vascular Neurology, Medical & Biological Engineering & Computing, American Journal of Neuroradiology, Computers in Biology and Medicine.